COMPARING SIMULATION AND EXPERIMENTS FOR INTERPRETING THE MECHANISMS OF ELECTROCHEMICAL OXIDATION

Ožbej Vodeb

Doctoral Dissertation
Jožef Stefan International Postgraduate School
Ljubljana, Slovenia

Supervisor: Prof. Dr. Nejc Hodnik, National Institute of Chemistry, Slovenia

Evaluation Board:
Prof. Dr. Anton Kokalj, Chair, Jožef Stefan Institute, Ljubljana, Slovenia
Prof. Dr. Marc T. M. Koper, Member, Leiden University, Leiden, the Netherlands
Dr. Aleksandar R. Zeradjanin, Member, Max Planck Institute for Chemical Energy Conversion, Mülheim an der Ruhr, Germany

MEDNARODNA PODIPLOMSKA ŠOLA JOŽEFA STEFANA
JOŽEF STEFAN INTERNATIONAL POSTGRADUATE SCHOOL



Ožbej Vodeb

COMPARING SIMULATION AND EXPERIMENTS FOR INTERPRETING THE MECHANISMS OF ELECTROCHEMICAL OXIDATION

Doctoral Dissertation

PRIMERJAVA MED SIMULACIJO IN POSKUSOM ZA INTERPRETACIJO MEHANIZMOV ELEKTROKEMIJSKE OKSIDACIJE

Doktorska disertacija

Supervisor: Prof. Dr. Nejc Hodnik

Ljubljana, Slovenia, April 2026

To the Reader

Acknowledgments

I would first and foremost like to thank my mentor Prof. Nejc Hodnik for all the help and discussions we had during my PhD. For the most part I would like to thank him for allowing me to stray on my own and never discouraging me from looking into anything he deemed "weird". It is mostly thanks to him that I discovered a passion for electrochemistry in me.

Next, I would also like to extend a thank you to Dušan Strmčnik, who while not being present through all of my time during the thesis, instilled in me that good is not good enough. It is him who introduced me to Marc Koper and helped me to study in Leiden for 6 months, something I will always be thankful for. He is also the one who introduced me to single-crystal electrodes and is in large part the one who helped me develop the model in Chapter 5 for Ni hydroxide formation.

I would like to thank all my coworkers who helped me along or hung out with me during my study. A special shout out goes to Anja Logar, Dževad Kozlica, and Pedro Martins who did most of the electrochemical measurements. Pedro for the data on Pt(111) and Ni, Dževad for the beautiful Ni experiments, and Anja for measuring Ir nanoparticles in Chapter 6. Here I would also like to thank Marjan Bele for the IrO_2 samples used in this thesis, as well as Armin Hrnjić for the TEM images of all Ir samples.

A special thanks also goes out to all the people at Leiden University. Here I would like to especially thank Marc Koper for hosting me for 6 months and for showing me a broader picture regarding electrochemical simulation. Another thank also goes out to Rifael Snitkof Sol, who was my mentor there and showed me how to work with single-crystal electrodes. I will always cherish our discussions about electrochemistry and science. Another, thanks also to Saeid Bahjati, who provided STM images used in this thesis, as well as to Alfred Larsson, with whom I shared many a beer, while in Leiden.

Finally, a thank you to all my family and friends. A thank you to my mom and dad for getting me through my education, and my brother for keeping me grounded. I would also like to thank my friends some, for all the fun we had playing board games, Magic or TTRPGs, others for being a joy to be around.

I would like to acknowledge the use of Claude for improving text readability and grammar.

Abstract

The rising demand for alternative energy sources has brought hydrogen-based technologies to the forefront as promising contributors to future energy systems. As these technologies develop, a deeper understanding of the electrode–electrolyte interface becomes essential, along with mathematical models that accurately capture its behavior. This thesis presents the most widely used model equations for interpreting laboratory-scale rotating disk electrode (RDE) experiments and evaluates how effectively it explains experimental data.

I begin by outlining the need for electrocatalysts in the context of the global climate crisis. Chapter 1 provides a brief overview of the key electrochemical phenomena occurring at the electrode–electrolyte interface. Chapter 2 introduces the fundamental equations and assumptions used to simulate RDE experiments, along with a short discussion on how simulations can be fitted to experimental data.

Building on this foundation, Chapter 3 presents ElectroKitty, a Python library I developed around the model described in Chapter 2. Using ElectroKitty, I analyze three RDE-based systems (single-crystal Pt, polycrystalline Ni, and Ir nanoparticles) to explore the types of insights that can be extracted through mean-field approximations. Chapters 4 through 6 examine these systems individually, progressing from the simplest to the most complex. Each chapter concludes with a short discussion of the specific conclusions that can be drawn for that system.

Finally, in the concluding chapter, I summarize the overall insights gained and discuss the types of conclusions that can reasonably be drawn from such models.

Povzetek

Z naraščajočo potrebo po alternativnih virih energije postaja tehnologija, bazirana na vodiku, vse bolj obetajoča. S tem pa se nam odpira dodatna nujnost po razumevanju stičišča med elektrolitom in elektrodo in matematičnih modelih, ki to opišejo. V tem delu predstavim trenutno najpopularnejši model za opisovanje laboratorijskih poskusov na rotirajoči elektrodi (ang. RDE) in razpravljam o uporabnosti modela za opis podatkov iz teh poskusov.

Delo začnem s predstavitvijo elektrokatalize kot pomembnega področja za bitko z globalno podnebno krizo. Temu sledi hitra predstavitev procesov na elektrodi v 1. poglavju. V 2. poglavju predstavim matematični model, ki opisuje RDE elektrode. Tam predstavim vse potrebne enačbe in predpostavke, nujne za njen opis. Prav tako v tem poglavju predstavim metode za prilagajanje simulacije podatkom in podam nekaj opomb iz osebne prakse.

Temu sledim v poglavju 3, kjer predstavim ElectroKitty, ki je programska knjižnica, spisana za Python. Z uporabo te knjižnice poskušam opisati tri različne sisteme, ki si sledijo po kompleksnosti. V poglavju 4 poskušam pokazati model za oksidacijo površine Pt(111), v petem nastanek hidroksida na poli-kristalinični površini Ni in nazadnje opisati reakcijo nastanka kisika na nanodelcih iridija. Vsak sistem terja svoje poglavje, na koncu katerega diskutiram o vpogledih, ki jih taki modeli omogočajo. Tako tudi delo zaključim s splošno diskusijo in potrditvijo hipotez iz poglavja 1 in povzamem, kakšne zaključke smemo delati z uporabo modela v poglavju 2.

Contents

Acknowledgments **vii**

Abstract **ix**

Povzetek **xi**

Contents **xiii**

List of Figures **xvii**

1 Introduction **1**
1.1 The Necessity of Electrocatalysis 1
1.2 Understanding Materials Behavior 3
1.3 Surface Phenomena 4
1.3.1 Electrochemical reactions 4
1.3.2 Capacitive processes 5
1.4 Modeling and Interpreting Electrochemical Results 7

2 Modelling Electrochemical Experiments **9**
2.1 Governing Equations 9
2.1.1 Mass transport 9
2.1.2 Rate laws 11
2.1.3 Surface reactions 13
2.1.4 Capacitance and resistance 14
2.2 Simulating Electrochemistry 15
2.3 Modeling Electrochemical Experiments 16
2.4 Notes 17

3 Developing a Programing Tool **19**
3.1 The ElectroKitty Package 19
3.1.1 The ElectroKitty class 21
3.1.2 The ElectroKitty_parser instance 21
3.1.3 The cpp_ekitty_simulator and ElectroKitty_simulator instances 21
3.1.4 The optimization_controller and optimization_routines instances 22
3.1.5 The loss_functions instance 22
3.1.6 The MCMC_sampler instance 22
3.2 Outlook 22

4 Modelling Pt(111) Oxidation **25**
4.1 Introduction to the Problem 25

4.2 Experimental Details 27
4.3 Kinetic Model 28
4.4 Modeling Results and Discussion 30
4.5 Concluding Remarks 33

5 Modeling Polycrystalline Ni Surface 35
5.1 Introduction to Ni Electrochemistry 35
5.2 Experimental Detail 37
5.2.1 Chemicals and materials 37
5.2.2 Surface preparation of polycrystalline nickel electrodes 37
5.2.3 Electrochemical measurements 37
5.3 Results and Discussion 38
5.3.1 Mechanistic models governing the initial stages of Ni (hydr)oxide formation 39
5.4 Conclusions 43

6 Modeling OER and Oxidation of Ir Nanoparticles 45
6.1 Introduction 45
6.2 Experimental 47
6.2.1 Materials and electrochemical characterization 47
6.3 Model 48
6.4 Results and Discussion 50
6.4.1 Characterization/comparison of materials 50
6.4.2 ACV voltammograms/harmonics and their interpretation 53
6.5 Discussion on OER Mechanism Fits 55
6.6 Conclusion 60

7 Conclusions 61

Appendix A 63

Supplementary Materials for Chapter 4 63
A.1 ElectroKitty Code Containing the Model 63
A.2 STM Images of Pt(111) Before and After Going to 1.15V 64
A.3 Comparing Experiment and Simulation of Potential Holds 65
A.4 Simulated Response From Literature 66

Appendix B 67
B.1 Demonstrating HER Subtraction From CVs 67
B.2 Figure Showing the Linear Dependance of the Anodic Peak 68
B.3 Note on the Decreasing Anodic Current 68
B.4 Figure of Simulated Potential Holds 68
B.5 Simulated Coverages of the Ni Place-Exchange Model 70
B.6 ElectroKitty Code for the Place-Exchange Model 70

Appendix C 73
C.1 XRD Spectra and Sample Analysis 73
C.2 Model Equations 74
C.3 Constants Used 75
C.4 EIS Spectra 75
C.5 Found Constants for Each Material 76

References **81**

Bibliography **95**
Publications Related to the Thesis 95
Journal Articles..... 95

Biography **97**

List of Figures

Figure 1.1: Globally reported number of natural disasters by year. 1
Figure 1.2: A rough representation of an electrochemical interface. 6
Figure 3.1: Figure shows how the various modules of ElectroKitty are connected to each other. 20
Figure 4.1: A typical CV of Pt(111) in 0.1 M HClO4, with a scan rate of 50 mVs^{-1} 26
Figure 4.2: Comparison of pseudocapacitances of experimental and simulated CVs at different scan rates 30
Figure 4.3: The experimental and simulated response of continuously changing the vertex potential when measuring a Pt(111) electrode in 0.1 M HClO4. 30
Figure 4.4: The comparison between the experimental and simulated responses of the ACV measurement 31
Figure 4.5:Comparison between simulated and experimental potential holds for a Pt(111) electrode in $HClO_4$. 32
Figure 5.1: Schematic illustration of proposed mechanisms for Ni oxidation in alkaline media. 36
Figure 5.2: Electrochemical probing of the initial stages of Ni (hydr)oxide formation. 39
Figure 5.3. Comparisons between different models and experimental data. 42
Figure 6.1: TEM images and particle size distributions for the studied materials. 50
Figure 6.2: LSV comparison between the different Ir catalysts. 51
Figure 6.3: Comparison between LSV (3a) and 3rd harmonic (3b) for Ir Black. 52
Figure 6.4: 3rd harmonic comparison for the studied materials. 54
Figure 6.5: Comparison between simulation and experiment for the 4th harmonic currents after activation 57
Figure 6.6: A comparison between materials. 59

Figure A. 1: In-situ STM images before (Left) and after (right) a scan up to 1.15V. 64
Figure A. 2: Simulated potential holds with a variation in potential. 65
Figure A. 3: Potential hold simulation using the literature model. 66

Figure B.1: Demonstrating on HER subtraction from voltamograms. 67
Figure B.2: Linear dependence of the Ni hydroxide peak. 68
Figure B.3: Simulated potential hold experiment 69
Figure B.4: Simulated coverages of the place exchange model in Chapter 4 70

Figure C.1: XRD spectra of Ir Black, Ir on Vulcan and IrO_2 nanoparticles. 73
Figure C.2: High frequency EIS spectra for the investigated samples. 76

Chapter 1

Introduction

1.1 The Necessity of Electrocatalysis

In recent years, the frequency and severity of natural disasters have increased noticeably as a result of climate change (Figure 1.1) [1]. These events are often unpredictable and can lead to devastating consequences. Some regions now suffer from extreme drought and limited access to clean water, while others experience unusual or unprecedented weather patterns, such as snowfall in Texas [2], [3], [4]. Although many people—myself included—live in specific areas that have not yet experienced the most severe direct impacts, Europe and other highly developed regions still feel both significant direct and indirect effects. These include rising social tension, concerns about future climate migration, and growing feelings of uncertainty. For many, this has manifested as climate anxiety, or eco-anxiety, which has become increasingly recognized in recent years [5]. Wherever you might live, there is no doubt that climate change has influenced your life in one way or another.

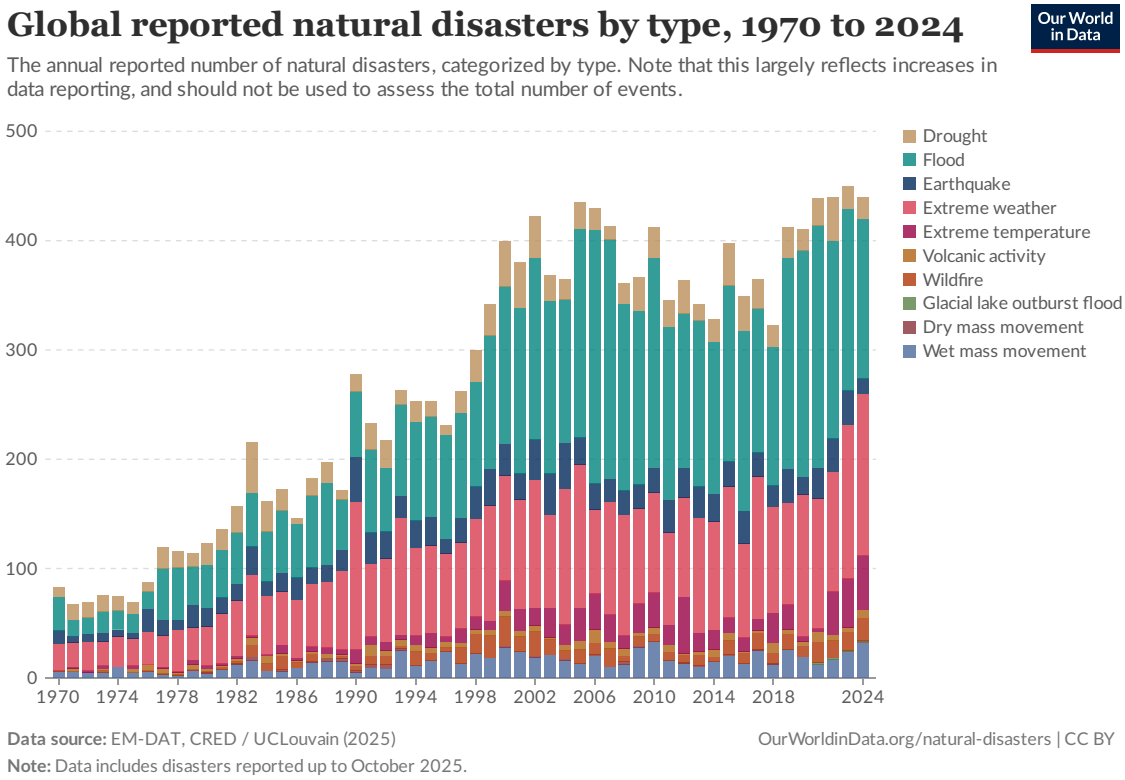


Figure 1.1: Globally reported number of natural disasters by year. Taken from [1].

The question then becomes what can be done to mitigate, or even prevent, the fallout from climate change. The solution seems to be two-fold. First is the more practical scientific answer. Science has already played a crucial role in identifying how current environmental changes correlate with pollution and in forecasting the potential consequences for human societies. It also provides pathways toward solutions, whether through technologies that reduce or remediate environmental damage or through innovations that fundamentally change the way we produce and consume resources. However, as Thomas R. Oliver wrote: "Science can identify solutions to public health problems, but only politics can turn most of those solutions into reality" [6]. For scientific solutions to be implemented effectively, the societies and economies in which we live will need to undergo substantial transformation. In particular, the global energy economy must change. How we produce, store, and consume energy will have to shift dramatically, as global CO_2 emissions continue to rise year after year. These economic shifts will, in turn, reshape social structures and the relationships within them. Only through coordinated scientific, political, and socio-economic change can the effects of climate change be meaningfully addressed [7], [8], [9].

The socio-economic and political dimension lies beyond the scope of this thesis, but it is important to acknowledge its role. In this work, the focus will be on how electrocatalysis can contribute to addressing current challenges in energy production and storage. Our societies are largely dependent on fossil fuels (such as natural gas, gasoline, and coal) for their energy production [10]. This proves to be a fundamental problem, as other technologies advance, and usually require more energy, the environment becomes more polluted, as more fuel needs to be consumed, irrespective of what kind of advancement it is. Consequently, there is an urgent need for new, sustainable energy sources, as well as effective methods for storing and transporting that energy [8], [9], [11], [12].

One of the most practical methods for storing energy is in the form of chemical fuels that can be used in energy-conversion devices. Several chemicals have the potential to serve as energy carriers, with hydrogen, ammonia, and methanol being among the most promising. These fuels can be produced using excess electricity generated by power plants and then stored for periods of increased energy demand. To enable this, technologies capable of converting electricity into chemical products and converting those chemical products back into electricity on demand are required. Devices that generate chemical fuels are known as electrolyzers, while those that consume these fuels to produce electricity are called fuel cells. Although they serve opposite purposes, both devices operate on closely related principles, with one essentially functioning as the reverse of the other [8], [9], [11], [13].

The performance of these devices ultimately depends on understanding the surface processes that occur during their operation. Among the most important are the catalytic reactions that produce or consume fuel, as well as the degradation processes that eventually lead to device failure. Both must be understood to enable the design of efficient and durable systems. While these processes can be broadly grouped into catalytic and degradative categories, the reality is far more complex: numerous surface phenomena occur simultaneously, often interacting with and influencing one another [14], [15], [16], [17], [18].

To disentangle and understand these complex phenomena, it is necessary to use model systems. Such systems can vary widely in scale, from nanoelectrodes to model fuel cells or electrolyzers, depending on the level at which the processes of interest are to be examined. One of the most fundamental model systems for studying catalyst behavior is the rotating disk electrode (RDE) operated in a three-electrode configuration. In this setup, the working electrode (WE) is immersed in an electrolyte solution, allowing direct probing of surface behavior under controlled and well-defined hydrodynamic conditions. The electrode surface can take many forms, ranging from single- or polycrystalline materials to supported catalyst powders, making the RDE a versatile technique for investigating a wide variety of catalytic surfaces [14], [18], [19].

Understanding how a surface behaves under potential control is essential for interpreting catalytic reactions such as the oxygen reduction and hydrogen evolution reactions (ORR and HER). In real electrochemical environments, catalytic activity is shaped not by a single step but by a combination of interfacial processes—including adsorption and desorption dynamics, competitive reactions, changes in surface coverage, double-layer effects, and local variations in pH or ion concentration, all of which interact in complex ways. Studying surface behavior also helps reveal when and how catalytic activity is lost, as degradation mechanisms such as dissolution, oxidation, restructuring, or poisoning can significantly alter performance. Over the years, many systems have been explored to better understand these interconnected phenomena and their impact on catalytic surfaces [14], [15], [16], [17], [18].

To help with understanding the observed signal, different mathematical models have been proposed to describe the observations. The models themselves range from microscopic descriptions to macroscopic models. Atomic-level descriptions typically employ density functional theory to predict stable surface states and the transition states between them [19]. The next level consists of mesoscopic models, which use kinetic rate laws in an attempt to directly reproduce experimental curves. These models form the basis of the present work, though, as will be shown, they have notable limitations and sometimes fail to adequately explain experimental responses. At the highest scale are macro-scale multiphysics models, which couple device-level operation to numerous interacting phenomena but cannot resolve atomic-level detail. Such models are generally applied to larger, practical devices to quantify energy losses during operation [19], [20]. To apply any of these modeling approaches effectively, it is important to have a basic understanding of surface behavior and different transport phenomena across scales. For this reason, the thesis begins with a brief overview of materials behavior before discussing how the results produced by these models can be interpreted.

1.2 Understanding Materials Behavior

As noted earlier, understanding materials behavior is essential for the development of efficient energy-conversion devices. This task is challenging, as modern materials exist in a wide range of forms, from well-defined single crystals to complex nanostructured catalysts. Characterizing such diversity requires multiple approaches, and the choice of which technique would be best suited depends largely on the specific properties one wishes to probe and on the nature of the material itself. Techniques such as: electrochemical measurements, X-ray Photoelectron Spectroscopy (XPS), Fourier Transform Infrared spectroscopy (FTIR), and others, offer valuable insight into how electrochemical devices operate, and when applied appropriately, they can even reveal the fundamental processes that govern their performance.

Historically, most characterization techniques were designed to investigate bulk materials properties, such as crystal structure, composition, or conductivity. However, to study catalysis, it is more important to study the structure and phenomena at the surface. With the interest in catalysis ever increasing, both thermal and electrochemical, where reactions and changes occur exclusively at the surface, has driven the development of novel surface sensitive techniques in the 20th century, and continues even to this day. In electrocatalysis, the active sites responsible for the reaction are located directly at the electrode–electrolyte interface [14], making bulk-focused, and even some “surface-sensitive”, techniques insufficient for understanding interface behavior. Consequently, methods capable of selectively probing surfaces, and even single atomic layers, have become indispensable [14], [15], [16], [17], [18].

Among the most challenging aspects of surface science is the direct study of surface reactions themselves. Determining surface structure with high precision is already difficult; resolving how that structure evolves dynamically under reaction conditions is even more demanding. In thermal catalysis, researchers typically rely on indirect measurements, such as changes in reactant or product concentrations, to infer reaction mechanisms. Electrocatalysis offers a conceptual advantage in that reaction rates can, in principle, be measured directly through the current response. However, this apparent simplicity can be misleading. Although electrochemical experiments often monitor reaction rates as a function of applied potential, the measured current is a convolution of all processes occurring at that potential. These processes may include faradaic reactions, capacitive charging, adsorption and desorption events, and mass-transport contributions, all of which overlap in time and magnitude. As a result, careful interpretation is crucial, and extracting mechanistic insight requires an understanding of how each process contributes to the observed signal [19], [21], [22], [23], [24].

1.3 Surface Phenomena

In this work, the focus will be on surface phenomena that occur in solution under potential control. These interfacial processes can be broadly categorized into three groups. The first are Faradaic processes, which involve charge transfer across the interface and are conceptually the simplest. The second are capacitive processes, in which excess charge is stored electrostatically on the electrode. The third group, pseudo-capacitive processes, combines features of both charge-transfer and charge-storage behavior. Understanding these distinctions is essential not only for this thesis but for understanding electrochemistry in general. While additional processes (such as phase transitions, or surface reconstructions) also occur at interfaces, many of these can be viewed as consequences of the fundamental electrochemical mechanisms described above. A solid grasp of these primary processes therefore provides a foundation for interpreting more complex surface behavior.

To begin, we define the interface as the boundary between two distinct phases: the electrode and the electrolyte. It is thus a mathematical construct that helps us conceptualize the region of interest. The importance of it lies in what occurs at and near this dividing surface, since this is where nearly all meaningful changes in the electrochemical system take place. It is important to note that the boundary is not sharp. Rather, it spans a region in which both the surface atoms of the electrode and the electrolyte species near the surface behave differently from those in their respective bulk phases. A schematic representation is provided in Figure 1.2a.

On the electrode side, we simply refer to the outermost atoms as surface atoms, and the rest as the bulk. On the electrolyte side, however, the interfacial region is typically divided into three sub-regions. Closest to the electrode is the inner Helmholtz plane (IHP), consisting of electrolyte species that interact most strongly with the electrode surface. As processes in this region are not the primary focus here, they will not be discussed in detail. Beyond it lies the outer Helmholtz plane (OHP), containing ions and molecules that remain influenced by the electrode potential but possess greater freedom of movement. Finally, farther from the surface is the bulk electrolyte, where species behave essentially independently of the electrode [19], [25].

1.3.1 Electrochemical reactions

Electrochemical reactions are central to electrocatalysis. In simple terms, they are chemical reactions driven by charge transfer between an electrode and a reacting species. Because the charge state of the species changes, all electrochemical reactions are, by definition, redox reactions. These reactions are further classified according to whether they are influenced by the electrode surface or not [19], [25].

Most textbooks first introduce electrochemical reactions that are not strongly affected by the surface, although such reactions are relatively rare in practice (Figure 1.2b). They typically involve metal complexes or other large molecules that undergo no significant structural changes during the reaction and interact only weakly, if at all, with the electrode. These are known as outer-sphere reactions, adopting the terminology of the Marcus–Hush model. Experimentally, outer-sphere reactions are almost always diffusion-limited and produce the characteristic duck-shaped voltammetric response. A key diagnostic feature is that changing the electrode material does not alter the reaction kinetics [19], [25].

The second major class comprises reactions that exhibit a strong dependence on the electrode material and for instance its crystallographic orientation (Figure 1.2c). These are called inner-sphere reactions, as the reacting species forms a chemical bond with a surface atom during the charge-transfer step. These reactions play a major role in electrochemistry and can produce a wide range of voltammetric signatures. Inner-sphere reactions can be further divided based on the fate of the product. If the product remains adsorbed on the surface and forms a strong chemical bond, the process may be classified as pseudo-capacitive, and the reaction rate is limited by the number of available surface sites. In contrast, if the product desorbs or does not form a strongly bound surface species, the reaction is categorized as Faradaic, because in this case the rate can be limited by charge-transfer kinetics, mass transport, or both [19], [25].

1.3.2 Capacitive processes

While electrochemical reactions involve charge transfer between the electrode and a reactant, there exists another type of response that generates current without any actual electron exchange. In this case, the observed current arises from the applied potential attracting charged species, typically ions in the electrolyte, though the solvent can also play an important role, toward the electrode surface. As these charged species redistribute in response to the applied potential, the overall charge distribution in the solution shifts, producing a measurable current. Because no electron transfer occurs, the ions remain confined near the electrode, effectively forming a capacitor; hence, this behavior is referred to as capacitive charging [19], [25].

Close to the electrode surface, ions and solvent molecules begin to order themselves based on the charge distribution of the surface (Figure 1.2a). This ordering gradually diminishes with distance from the surface. Depending on the degree of organization, the interfacial region is divided into the inner Helmholtz plane (IHP) and the outer Helmholtz plane (OHP), separated by corresponding Helmholtz planes. The detailed structure of the electrochemical double layer is complex, and numerous models have been developed to describe it. In this work, however, we will not explore these models in depth and will instead approximate the charging current as a constant, noting that more sophisticated descriptions exist [19], [25].

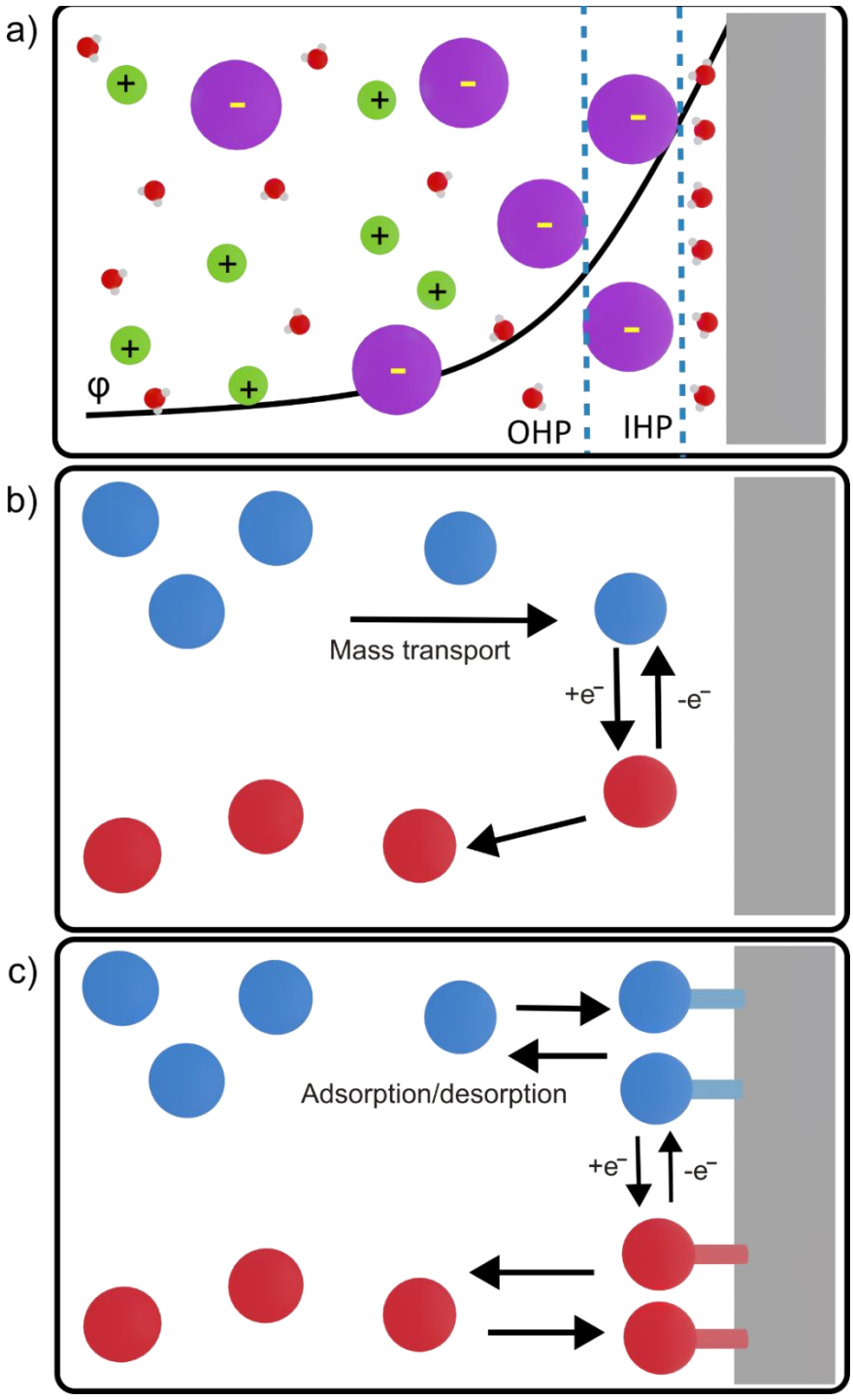


Figure 1.1: A rough representation of an electrochemical interface. a) The diffuse layer in which a distribution of charged species forms, due to electrical potential φ. This distribution leads to the formation of the double-layer, with the inner and outer Helmholtz planes shown (IHP, OHP). b) Shows the Faradaic reaction, where an electrochemical reaction converts blue species to red ones and vice-versa. c) A pseudocapacitive process. Here the blue and red species are bound to the surface, and a reaction occurs among them. The species can also adsorb and desorb.

1.4 Modeling and Interpreting Electrochemical Results

There are many ways to model electrochemical experiments, ranging from approaches that attempt to describe atomistic behavior at the interface to methods that treat the system from a more "zoomed-out" perspective. At the most fundamental level are microscopic models, which typically simulate only a small number of atoms—rarely more than a hundred. These ab initio techniques are most often based on density functional theory (DFT), which remains one of the most widely used tools in quantum chemical simulations. Despite its great usefulness, DFT also has significant limitations, and other numerical approaches such as force-field molecular dynamics (MD) or force-field Monte Carlo (MC) simulations, though less commonly applied to electrochemical systems, can also capture microscopic features [15], [19], [25].

A step above these are continuum models, where relevant quantities are treated as smooth functions. These approaches often involve variations of Fick's second law or the Poisson equation to describe mass transport and electric fields within the solution. Continuum models typically focus on the working electrode (WE) and treat the bulk solution as an effectively infinite thermal reservoir. Another popular method, especially in impedance spectroscopy, is the equivalent-circuit approach, where the system is approximated using basic electrical components such as resistors and capacitors. These components are then mapped onto physically meaningful parameters. At larger or industrially relevant scales, model choice depends on the application: continuum models may be used for multiphysics simulations, whereas equivalent circuits may be preferred for simplified device-level analysis [19], [26], [27].

In this work, the emphasis will be on continuum models or, in the case of surface-bound reactions, mean-field models. These are most relevant for laboratory-scale studies, though they remain crude approximations. Their main advantage is that they can be readily fitted to experimental data, since their direct output is a potential–current relationship. However, the conclusions that can be drawn from such fits can be limited. The physical relevance of the fitted parameters is often uncertain, but useful insights can still be obtained when the model is interpreted within a narrow and well-defined context.

The goal of this thesis is therefore to demonstrate that:

1. solving these models need not be a complicated task, and their simulation and fitting can be automated,
2. simulation and fitting can provide reasonable hypotheses about the underlying reaction mechanisms,
3. the types of conclusions and the details of a system, which can be inferred, strongly depends on the type of model and how it is applied to a system.

Accordingly, the thesis begins with a brief introduction to the governing equations, followed by an explanation of the Python library developed during this work, and concludes with three model systems that illustrate how the strength and clarity of the conclusions depend on the complexity of the electrochemical system.

Chapter 2

Modelling Electrochemical Experiments

In this chapter, I will briefly outline the equations used to model electrochemical experiments. Because this work focuses on the most basic electrochemical systems, many of the formulas simplify considerably. It can be tempting to apply these simplified forms to more complex systems, but such simplifications must be justified—either through numerical testing or by comparing model predictions with experimental data.

To provide context, I will begin by describing how an electrochemical system can be defined in its most complete form and review the full set of equations required for a general description. I will then show how, through a series of reasonable assumptions, these equations can be simplified to make numerical simulation more practical. In each chapter, the complete model will be presented first, followed by the rationale for the simplifications. The final simplified form is the version implemented in the Python library introduced in the next chapter.

2.1 Governing Equations

2.1.1 Mass transport

We begin with mass transport. This is governed by Fick's law, with a slight addition. Both the first and second are usually written with the diffusion and convection terms, but in electrochemistry, we need to add a term to account for migration to fully encapsulate the transport phenomena at the electrode [19], [28].

$$\vec{J} = -D\nabla c + \vec{v}c - \frac{zF}{RT}D\nabla\phi c \tag{2.1}$$

Equation 2.1 is known as the Nernst-Planck equation, which shows how the three contributions alter the flux of a species (J). The first term is diffusion, which is determined by the diffusion coefficient (D) and the gradient of the concentration c. The second is the convective term, which dictates how fluid velocity (v) impacts transport. Finally, there is the migration term, which dictates how the gradient of the potential field affects the species distribution, though the chemical must have an electric charge for this term to hold. In the last term, z is the species charge, F the Faraday constant, R the gas constant, T is the temperature of the system, and ϕ as potential.

The migration term is often neglected because a supporting electrolyte is typically present in excess. The high concentration of dissolved ions ensures that they act as the primary charge carriers between the working and counter electrodes. As a result, the electric field within the solution has only a minimal influence on the motion of the reacting species, allowing the contribution of migration to the measured current to be safely ignored. In recent years, however, several studies have examined the potential impact of migration under experimental conditions. Their results confirm that when the supporting electrolyte concentration is sufficiently high, migration effects are indeed negligible [29]. At lower electrolyte concentrations, however, the situation differs: migration can significantly influence the system's behavior in ways that extend beyond the simple concept of solution resistance [19], [28].

Thus, we are left with only two terms governing mass transport in the system we aim to simulate. In principle, one could solve for the concentration profile using only the flux expression, but this would provide limited insight. Because most electrochemical experiments are time-dependent, we must also obtain the temporal evolution of all relevant variables and of any quantities derived from them. For this reason, the Nernst-Planck equation alone is insufficient. To capture the time dependence of mass transport, we must employ Fick's second law, which describes how concentration changes with time. In its general form, neglecting migration, this is expressed as [19], [28]:

$$\frac{\partial c}{\partial t} = D\nabla^2 c - \vec{v}\nabla c \tag{2.2}$$

Most laboratory studies employ electrodes with well-defined geometries, so it is practical for general simulation tools to incorporate the relevant geometry from the outset. Because many experiments are performed using flat rotating disk electrodes (RDEs), equation 2.2 can be simplified further to make numerical solutions more efficient. RDEs typically have diameters of at least 4 mm, which when compared to the thickness of the diffusion layer—typically in the order of 0.01 mm to 0.1 mm—the electrode is at least an order of magnitude larger. This allows us to assume that concentration gradients along the plane of the electrode surface are much more gradual than those perpendicular to it. If the electrode diameter were significantly smaller, this assumption would break down. With this approximation, the dimensionality of equation 2.2 is reduced from four variables (one temporal and three spatial) to just two: one temporal dimension and one spatial dimension (normal to the surface) [19], [28].

To solve the resulting system, three boundary conditions are required. The first is the initial condition, for which we typically assume a uniform concentration equal to the bulk value (c_{bulk}). The second applies at the outer boundary, where the concentration is assumed to remain constant in the limit of large distance, practically a few hundred micrometers from the electrode, reflecting the fact that the bulk solution is far larger than the simulated region and unaffected by local changes. The third boundary condition is at the electrode itself. Here, the applied potential drives electrochemical reactions, and the flux at the surface must be equated to the corresponding reaction rate. These boundary conditions, together with the simplified transport equation, are summarized in equations 2.3.[19], [28]

$$\frac{\partial c}{\partial t} = D\frac{\partial^2 c}{\partial x^2} - \vec{v}\frac{\partial c}{\partial x} \tag{2.3a}$$

$$c(t = 0, x) = c_{\text{bulk}} \tag{2.3b}$$

$$\lim_{x \to \infty} c(t = t, x) = c_{\text{bulk}} \tag{2.3c}$$

$$-D\frac{\partial c}{\partial x} = \sum r_{\text{forward}} - \sum r_{\text{backward}} \tag{2.3d}$$

The r in equation 2.3d is either the forward and backward reaction rate. The same terms could also be added to equation 2.3a, given that chemical reactions take place among the dissolved species. The formulation of the rate law dictates the form r will take when the system is eventually solved. The form of the rate law is detailed in section 2.1.2.

This concludes the derivation of the mass-transport equations. Although the derivation above considers a single species, systems containing multiple species require additional equations, resulting in a set of coupled partial differential equations (PDEs) that must be solved simultaneously. Solving such systems can be challenging. During my studies, however, I developed a programming library capable of solving these electrochemical PDE systems efficiently. An overview of the library is provided in Chapter 3, and further details are available on the project's GitHub page [30], [31].

2.1.2 Rate laws

To describe the reactions occurring in the system, we need a mathematical framework for expressing their rates. This is provided by the rate law. The choice of rate law determines the form of the boundary condition in equation 2.3d and dictates how surface reactions are modeled. In general, a rate law specifies how the reaction velocity depends on system parameters. While classical chemical kinetics focuses primarily on temperature and concentration, electrochemical systems require the additional consideration of electrical potential.

Rate laws typically follow the structure shown in equation 2.4, where the reaction rate is proportional to a rate constant and a product of species concentrations. This form can be understood by considering two probabilities. The concentration term reflects the probability of finding the reacting species, with the exponent n indicating the reaction order. The rate constant k represents the intrinsic probability that the reaction occurs once the species encounter each other. Together, these determine the overall reaction velocity. Because k depends on environmental factors such as temperature and the local electrochemical conditions, a suitable model is required to relate these parameters to the reaction rate [19].

$$r = k \prod_i c_i^n \tag{2.4}$$

The first kinetic model to consider is the Butler–Volmer model. It was originally introduced as a phenomenological law to describe the empirical relationship between electrode potential and reaction rate. Over time, the model was refined and linked to transition state theory, giving it a more rigorous theoretical foundation. Despite the development of many alternative models since its introduction, the Butler-Volmer formulation remains the most widely used [19]. Its popularity stems largely from its simplicity: it is both computationally efficient and conceptually straightforward. The model is expressed in equations 2.5 [19], [28].

$$k_{\text{forward}} = k_0 e^{-\alpha \frac{zF}{RT}(E-E^{0\prime})} \tag{2.5a}$$

$$k_{\text{backward}} = k_0 e^{(1-\alpha) \frac{zF}{RT}(E-E^{0\prime})} \tag{2.5b}$$

The remaining parameters in the Butler–Volmer equation are the charge-transfer coefficient α, the pre-exponential factor k_0, and the standard (or more commonly, the formal) potential $E^{0\prime}$. Their full derivations are discussed extensively in the electrochemistry literature [19], [25], but a more intuitive explanation is helpful here.

The charge-transfer coefficient α describes how the applied potential affects the energy barrier of the reaction. When a potential is applied, it shifts the energies of the reactant and product states differently. The value of α (which always lies between 0 and 1) determines how much of this potential shift stabilizes the transition state for the forward reaction versus the backward reaction. If α is close to 0.5, both directions respond symmetrically to changes in potential. If α is closer to 0 or 1, one direction is strongly favored by potential changes. In practical terms, α tells us which reaction, oxidation or reduction, is more sensitive to the applied potential.

The parameter k_0 is the pre-exponential, or "rate constant," at the formal potential $E^{0\prime}$. It incorporates several physical contributions: the frequency of molecular encounters, the probability of successful electron transfer, and properties related to the local environment (such as solvent structure, double-layer effects, and temperature). Because so many factors influence k_0, the interpretation it offers as a value is dubious. Nevertheless, within the Butler-Volmer framework, k_0 determines the intrinsic speed of the reaction: higher values correspond to faster electron-transfer kinetics.

Finally, the formal potential $E^{0\prime}$ defines the potential at which the forward and backward reaction rates are equal. It is closely related to the thermodynamic driving force of the reaction. When the applied potential is more positive than $E^{0\prime}$, oxidation is favored; when it is more negative, reduction dominates. Thus, $E^{0\prime}$ sets the energetic reference point that determines which direction the reaction prefers under a given potential.

In principle, the Butler–Volmer framework provides all that is needed to simulate basic electrochemical systems and their reaction mechanisms. However, it is still valuable to consider other kinetic models that have been developed over the years, especially those aimed at describing inner-sphere reactions [25], [32], [33], [34], [35], [36]. These reactions remain difficult to model because the precise role of the catalyst surface in facilitating electron transfer is not yet fully understood.

The first major alternative to the Butler–Volmer model appeared in the mid-1950s with the development of the Marcus–Hush theory [34], [35], [37]. Initially formulated for electron transfer between molecules in solution, the model was soon extended to incorporate the effect of electrode potential, making it applicable to electrochemical systems. The central idea behind Marcus theory is the inclusion of solvation (or reorganization) energy in the rate expression. Electron transfer can occur only when the system reaches a configuration in which the reactant and product states are energetically aligned, and achieving this configuration requires the surrounding solvent molecules to rearrange appropriately. Many formulations of Marcus–Hush theory exist, with the Marcus–Hush–Chidsey variant being one of the more widely used today, including in my simulation package. Although Butler–Volmer and Marcus–Hush remain the most familiar models among electrochemists, neither offers a complete or fully accurate description of the catalyst's role during an inner-sphere reaction.

Beyond these, additional theories were developed later in the 20th century [25], [32], [33], [38]. Notably, contributions from the Russian school and the model developed by Schmickler represent some of the most advanced attempts to explicitly account for catalytic effects at the surface. These models currently provide some of the most detailed descriptions of catalyst–reactant interactions, but their computational cost is high, and they have so far been applied only to a limited number of model systems. The technical details of these theories lie well beyond the scope of this thesis, but their existence is worth acknowledging.

For the purposes of this work, it is now more relevant to turn to how surface reactions can be modeled within the broader reaction framework.

2.1.3 Surface reactions

In the previous sections, I outlined the main components needed to describe an electrochemical system. Reactions involving species bound to the surface, such as adsorption or desorption, are not described by PDEs but by the much simpler ordinary differential equations (ODEs). However, when a surface species is kinetically linked to dissolved species, the result is a coupled system of ODEs and PDEs that must be solved simultaneously. The general form of such an ODE is shown in equations 2.6, and the number of ODEs required corresponds directly to the number of surface species included in the model [19], [28].

$$\frac{d\theta}{dt} = \sum r_{\text{forward}} - \sum r_{\text{backward}} \tag{2.6a}$$

$$\frac{d\Gamma}{dt} = \sum r_{\text{forward}} - \sum r_{\text{backward}} \tag{2.6b}$$

Because the species we aim to model are bound to the electrode surface, it is natural to describe their quantity in terms of surface concentration (Γ), or more conveniently, in terms of surface coverage (θ). The general form of the reaction rates remains the same as previously described, except that concentration terms are replaced by coverage. An important feature of surface-bound processes is that the reaction rate often depends on the degree of coverage itself. Thermodynamic treatments of adsorption, typically expressed through adsorption isotherms, show that coverage influences both the likelihood of additional adsorption and the overall accessibility of surface sites. The same behavior appears in the systems examined in this thesis. The study of adsorption isotherms spans more than a century, and many formulations have been developed. In this work, I focus on two classical and widely used isotherms: the Langmuir and Frumkin models [19], [28].

The Langmuir isotherm is based on the assumption that each adsorbing molecule occupies a single surface site and does not interact with neighboring adsorbates. When simulating this behavior, the rate expressions use the same basic form as presented in equation 2.5, with coverage or surface concentration replacing concentration. In contrast, the Frumkin isotherm incorporates interactions between adjacent adsorbed molecules. These interactions may be attractive or repulsive, depending on the specific system, and they modify both the adsorption energy and the coverage dependence of the reaction rate [19], [39].

Although many additional isotherms exist, some accounting for variations in adsorption site energy, surface heterogeneity, or more complex intermolecular interactions, these models lie beyond the scope of this thesis [40], [41]. The Langmuir and Frumkin isotherms provide sufficient flexibility to represent the vast majority of systems considered here. In some cases, however, mean-field models like these may be insufficient, and more detailed microscopic approaches may be required. The appropriate choice depends on the system being studied and the level of mechanistic detail one aims to extract from the modeling results [19], [39].

To model the Frumkin isotherm, a small modification must be applied to the rate constants introduced in equation 2.5. The central idea of the Frumkin approach is that interactions between neighboring adsorbates either increase or decrease the activation energy of the reaction, depending on whether these interactions are repulsive or attractive. To account for this effect, an additional coverage-dependent term is introduced into the exponential factor of the rate expression. Mathematically, this can be implemented by multiplying the rate constants in equation 2.5 by an extra exponential factor, as shown in equation 2.7 [19], [39].

In this formulation, the parameter g represents the strength of the lateral interaction between neighboring adsorbed species and may take either positive or negative values. Positive values correspond to repulsive interactions, while negative values indicate attractive interactions. The influence of this parameter on the shape of voltammograms, as well as its deeper physical interpretation, is discussed extensively in the literature [19], [39].

$$k = k_{\mathrm{BV}} e^{-g\theta} \tag{2.7}$$

With this, I conclude the brief survey of the key equations required to model reaction rates and mass transport in basic electrochemical systems. To fully describe such systems, two additional components must be included: an equation accounting for the potential drop due to solution resistance, and another describing the charging of the electrochemical double layer. These will be introduced briefly in the following section.

2.1.4 Capacitance and resistance

Finally, I introduce the basic equations used to model double-layer capacitance and solution resistance. In this work, only the simplest formulations are employed, as the examples presented in later chapters involve solutions with high ionic strength. Under such conditions, deviations from ideal behavior are minimal and, more importantly, are not relevant to the aims of this study. The capacitance and resistance models used here are therefore crude approximations, and many more sophisticated descriptions exist in the literature. For the systems examined in this thesis, however, such added complexity would offer little further insight, as the focus lies elsewhere [19], [28].

Equations 2.8 should be included to the previous ones to have a full description of the system. Equation 2.8a describes how the charging current (i_{c}) is proportional to the double-layer capacitance (C_{dl}) and potential. Equation 2.8b describes how the applied potential (E_{app}) is lowered due to solution resistance (R_{u}).

$$i_{\mathrm{c}} = -C_{\mathrm{dl}} \frac{dE}{dt} \tag{2.8a}$$

$$E = E_{\mathrm{app}} - R_{\mathrm{u}} i \tag{2.8b}$$

Up to this point, I have not yet addressed how the current is calculated, even though it is the primary quantity of interest in voltammetric experiments. There are two general approaches. One can compute the current directly from the flux (or, for surface processes, from the time derivative of coverage). However, in systems involving coupled ODEs and PDEs, it is more convenient to express the current as the sum of all electrochemical reaction rates. This leads to equation 2.9a, which relates the kinetic current i_k to the individual reaction rates. Equation 2.9b then defines the total current as the sum of the kinetic and capacitive contributions. This total current is the quantity inserted into equation 2.8b, which in turn determines the potential used in equations 2.8a and 2.5 [19], [28].

$$i_\mathrm{k} = -\sum_{\text{electrochemical}} r_\text{forward} + \sum_{\text{electrochemical}} r_\text{backward} \tag{2.9a}$$

$$i = i_\mathrm{k} + i_\mathrm{c} \tag{2.9b}$$

With all components now defined, we can, in principle, solve the system of equations presented in this section. The resulting model is nonlinear and involves a combination of coupled PDEs, ODEs, and algebraic relations. A few remarks on how such systems can be solved are provided in the following section, though the choice of numerical algorithm ultimately depends on the complexity of the specific system under consideration.

2.2 Simulating Electrochemistry

Simulating electrochemical systems through differential equations has been possible for several decades, but the field experienced significant growth in the 1990s, likely due to the increasing availability of computers. Many of the foundational contributions to numerical electrochemistry were made during this period by researchers such as Feldberg, Strutwolf, and Britz [28], [42], [43], [44], [45], [46]. Some of these authors also developed early simulation tools, including what later became DigiElch [47], which remains a widely used software package today. This section highlights key concepts in electrochemical simulation; for a more comprehensive treatment, the book by Strutwolf and Britz is highly recommended [28].

Modeling electrochemical systems typically involves solving coupled PDEs, ODEs, and algebraic equations, and a variety of numerical algorithms have been developed for this purpose. Each method comes with specific advantages and limitations, and the appropriate choice depends on the system being modeled. The earliest approaches were finite difference methods (FDM), which discretize the domain into points representing the dependent variables. Although computationally efficient, FDM can suffer from accuracy issues and is less suitable for complex geometries. To address these challenges, finite volume (FVM) and finite element (FEM) methods were introduced. Both approaches divide the simulation domain into small volumes or elements, usually tetrahedra, and solve the governing equations within these regions. Because FVM and FEM share conceptual similarities, they are often considered together. However, both methods are computationally more demanding and are typically used only when simulations require at least two spatial dimensions [28].

At the beginning of this chapter, I noted that this work focuses only on the simplest electrochemical systems, i.e. "simple" in the sense of geometry. This allows several important simplifications, the most significant being that the system reduces to a one-dimensional PDE. Under these conditions, the finite difference method (FDM) is the most appropriate numerical approach. Although FEM and FVM have been applied in previous studies, the simplicity of FDM makes it far easier to implement, while still providing sufficient accuracy for simulating experimental data [28].

FDM schemes are typically categorized as explicit or implicit, but explicit methods are almost never used in electrochemical modeling. This is because efficient simulations require relatively few grid points in the spatial (x) direction. Although increasing the number of points improves accuracy, an equivalent or even better level of accuracy can be achieved by using non-uniform grid spacing, something first introduced by Feldberg and still widely applied in modern simulation packages [28], [42], [46].

Additional details on how these numerical methods were implemented in this thesis, and in the development of ElectroKitty, are provided in the next chapter. For a comprehensive discussion of numerical approaches in electrochemistry, nontheless the previously mentioned book by Strutwolf and Britz remains the most authoritative reference. For researchers needing to simulate more complex geometries or systems involving multiphysics couplings, developing custom code is increasingly rare. Instead, established software platforms such as COMSOL Multiphysics and OpenFOAM are usually used for solving such problems [48], [49].

2.3 Modeling Electrochemical Experiments

Modeling experiments means attempting to reproduce the behavior observed in those experiments. In some fields, this may involve matching time-dependent concentration profiles or tracking changes in system energy. In electrochemistry, however, we probe surfaces directly by varying the potential and observing the resulting current, or in some techniques, by controlling the current and measuring the potential. Consequently, the primary quantities we aim to model are either the potential and the current. At present, there are no straightforward ways for extracting kinetic parameters with high certainty, particularly in systems involving multiple reactions. As a result, the most practical and commonly used approach is to adjust the model parameters so that the simulated response matches the experimental data [21], [39], [50], [51].

Fitting a simulation to experimental data can be challenging and computationally demanding. Parameter fitting is fundamentally a problem of function minimization, where the goal is to reduce a loss function (L) that measures the discrepancy between experimental and simulated data. A common choice is the squared-difference loss, though in electrochemistry, the relative root mean squared error (RRMSE) has become increasingly popular, particularly within the Fourier-transform alternating-current voltammetry community. The RRMSE is defined in equation 2.10. In practice, fitting involves adjusting model parameters until the loss function falls below a chosen threshold. While an ideal value of zero would indicate perfect agreement, this is virtually unattainable due to unavoidable experimental noise [21], [50], [51].

$$\mathrm{RRMSE} = \frac{\sum (i_{\mathrm{experimental}} - i_{\mathrm{simulated}})^2}{\sum i^2_{\mathrm{experimental}}} \tag{2.10}$$

Although one could perform parameter fitting manually, it is far more time-efficient to use algorithms designed for this purpose. Numerous optimization algorithms exist, each with strengths suited to different types of loss functions. A valuable feature in any fitting procedure is the ability to estimate parameter uncertainties or provide other statistical measures of confidence, since fitted parameters without uncertainty estimates are difficult to interpret meaningfully. One of the earliest and most widely used approaches is the Levenberg–Marquardt algorithm, which not only locates a minimum in the loss function but also returns the covariance matrix of the fitted parameters. While powerful, Levenberg–Marquardt is prone to converging on local minima. An alternative is to use more robust global-optimization methods such as CMA-ES, followed by a bootstrapping procedure in which multiple fits are initiated from different starting points and the results are analyzed statistically [52], [53].

Another option is to use Markov chain Monte Carlo (MCMC) methods to sample the full probability distribution of the parameters. Practitioners of these techniques generally recommend first performing a standard minimization to obtain an approximate best-fit point, which can then be used as the starting position for the MCMC chain; this reduces the burn-in period and improves convergence efficiency. MCMC is arguably the most robust approach to parameter estimation because it yields the entire parameter distribution rather than a single best-fit value, and, given sufficient sampling time, MCMC methods will always converge to the global minimum [23], [53].

A final approach, although not strictly rigorous from a mathematical standpoint, is to evaluate the extrapolative power of the fitted model. If both the proposed mechanism and the fitted parameters are valid, the model should be able to predict additional experimental behavior beyond the data used for fitting. This requires new experimental measurements to test whether the model's predictions hold. While this method does not constitute a formal statistical validation, it is physically meaningful and often provides valuable insight. In this work, I use both this predictive-validation approach (Chapters 4 and 5) and the examination of confidence intervals (Chapter 6) to assess the robustness of the fitted models.

2.4 Notes

With this, I conclude the chapter by providing a concise overview of the concepts necessary for understanding the electrochemical behavior of the different material surfaces presented in the following sections. The next chapter introduces the simulation library I developed during my studies, not only to accelerate my own work, but also with the hope that it may assist others in advancing their research more efficiently. Chapters 4, 5, and 6 then present several example systems in which the library is applied, along with commentary on the types of conclusions that can be drawn when fitting models of varying complexity.

The equations introduced here represent what is essentially a mean-field approximation, in which all regions of the system are assumed to behave similarly. Although this assumption is commonly made, there is growing evidence that it does not always hold, and that more sophisticated models may be required to capture the full behavior of certain systems. In this thesis, I aim to highlight the limitations of mean-field models, as they often leave one wishing for more detailed or more mechanistically grounded conclusions.

Chapter 3

Developing a Programing Tool

In today's age of data, the average electrochemist is expected to be familiar with at least some of the basics of data analysis. This includes finding current peaks, performing Tafel analysis, correcting uncompensated resistances, and sometimes even fitting models directly to measured data [54]. Over the years, many different tools have been developed to process or even simulate data. Today, almost every potentiostat program has methods for processing data, with some having more advanced features than others [55], [56], [57]. However, direct simulation of experiments is still not very common. A likely reason is that it is not straightforward to program a numerical algorithm that solves the governing equations, much less, fits the data. Unless an electrochemist has sufficient background in mathematics and computer science, fitting a model to the data can be a daunting task [58], [59], [60].

Over the years, many simulation packages have been developed. Some of the most popular are: DigiElch, which is distributed by Gamry Instruments [61], [62], MECSim, which was developed at Monash University is available for free [63], [64], and KISSA [65]. All these simulators offer the possibility to compute electrochemical responses for different electrode geometries and to simulate different mechanistic networks. However, all of them offer something which the others do not, thus I have decided to develop my own tool, to fit my specific use cases.

In recent years, Python has become one of the most popular programming languages in the world. Its most important features are the relative ease with which the language can be learned and the simple sharing of project code. The latter is partly due to the fact that Python has its own package manager and a website where the community can make its own projects freely available [54], [66]. This is exactly why I decided to program and publish ElectroKitty with Python, so that it is easily accessible, executable and understandable for everyone [31]. Combining this with a simulator written in C++, provides a good ratio between ease of use and performance. In this Chapter, I will delve further into the ideas behind ElectroKitty, so that the reasoning for the programming used can be explained in more detail.

3.1 The ElectroKitty Package

The ElectroKitty package consists of eight different modules, each of which does its part to either generate or analyze data. These are: the base class that controls everything, two simulator classes, one written in Python, the other in C++, a loss function class, optimization controllers and routines, an MCMC sampler, and a mechanism parser. Below the functions of each class are described in detail and how they are all interconnected to make the package work. Figure 3.1 shows the general scheme. It should be noted that all the modules presented, although created to work together, can also be used separately. This is useful if a user wants to use a different fitting algorithm but still wants to use the ElectroKitty simulator. Both the source code, as well as simple tutorials can be found on the project's GitHub page [30].

I chose to implement ElectroKitty using an object-oriented programming (OOP) approach, meaning that each module is structured as a class that encapsulates specific functionality. The main advantage of OOP, in my view, is that it makes scripting with ElectroKitty more intuitive. When an ElectroKitty object is instantiated, subsequent operations simply modify its internal properties through method calls. This structure helps the user clearly understand what actions are being performed and when particular inputs are required. OOP also simplifies handling large numbers of parameters, since all relevant variables are stored within the class and can be accessed or modified as needed. This eliminates the need for users to track where each parameter is declared or updated, making function calls cleaner and reducing the likelihood of errors.

This is not to suggest that other programming paradigms are unsuitable for such a library. A functional programming approach, for example, may be preferable in certain situations, particularly when working directly with functions is more intuitive. Ultimately, the choice reflects personal preference, but I consider it important to clarify why OOP was selected for ElectroKitty.

What follows are brief introductions to each class and what they are designed to do. How the different modules connect is schematically shown in Figure 3.1.

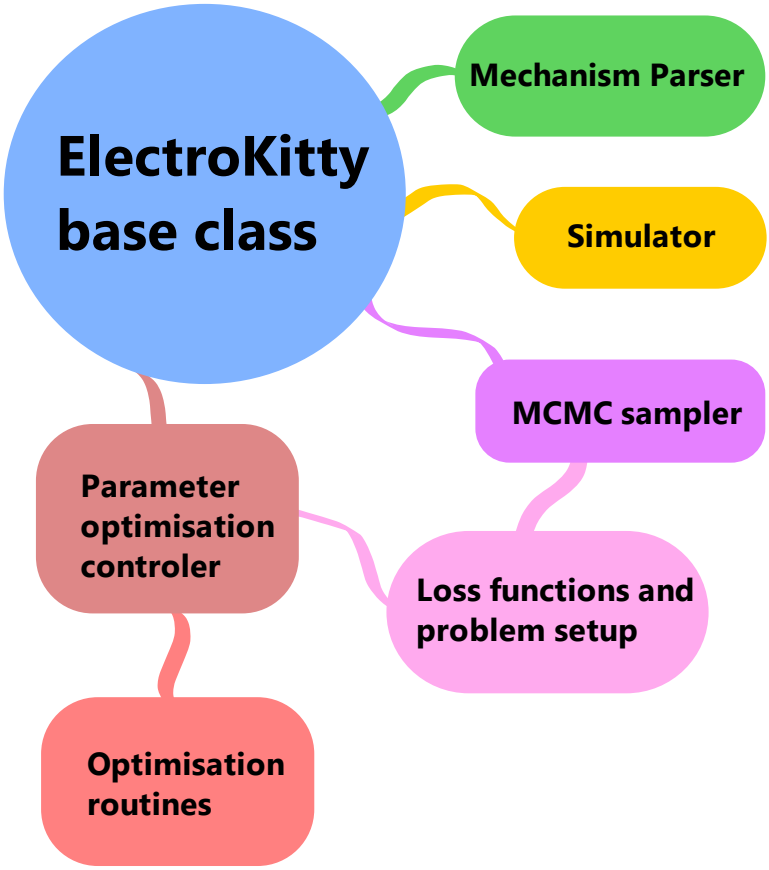


Figure 3.1: Schematic representation of the interconnections among ElectroKitty modules. Note that the base class has access to all submodules and can access them directly. As a result, at each point where the base class performs an operation, it calls the required submodule to do its work, which is then recorded by the base class.

3.1.1 The ElectroKitty class

This is the class that is most frequently called by the user, as it allows us to control all other aspects of the package. In this class, we find all our data, simulation results as well as the different constants used for the simulation or the best ones found from fitting data. This class has functions that we can use to call other classes to perform different operations. Another important feature of the class is that it can save and load itself. Given a file name, the class saves all its data in a binary file, which can then be loaded into another instance of the class so that no progress is lost. After parameter optimization, the class does this automatically, using the current date and time as the file name, so that progress is saved even if something goes wrong.

3.1.2 The ElectroKitty_parser class

This is a class that is called when the base class is initialized with a specific chemical and/or electrochemical reaction mechanism. It is a fairly simple class whose only task is to parse the given mechanism and pass the correct list to the simulator to run a simulation. For a given mechanism, this class separates the species into either dissolved or surface-bounded species and generates lists that are required for the simulator to work correctly. This is achieved by classifying each step as either electrochemical, chemical on the surface or chemical in solution, as well as reversible or non-reversible. Based on the classification done by the parser, the simulator then creates the necessary equations for it to solve.

3.1.3 The cpp_ekitty_simulator and ElectroKitty_simulator classes

Both simulators work in the same way, the only major difference is the programming language used. By default, the simulator cpp_ekitty_simulator is used, which was created with pybind11 [67], so that it can be easily operated with Python. Both simulators use the lists generated by the parser to create the differential equations applicable to the system and solve them. Currently, the simulator uses the Butler-Volmer and Marcus-Hush formalisms for its rate laws, which in the case of a pseudocapacitive current represents the individual differential equations for each species, while in the dissolved case the formalism is equated with the species flux at the electrode boundary as a boundary condition. The full model was presented in Chapter 2, as well as the justifications for the simplification. It is worth noting that ElectroKitty is valid only for systems for which such assumptions are applicable.

Fick's second law is approximated using the implicit finite difference method, where the coefficients of the second and first derivatives are given by the Fornberg algorithm [68]. In the diffusion layer, the derivatives are approximated with four points, while three points are used at the boundary. The complete set of equations is given in Chapter 2, which is then extended and modified in an appropriate way depending on the number of species. Implicit differentiation is used for the time step. The rate and diffusion equations are then coupled with equations 2.9a and 2.9b, which describe the double-layer charging and the potential drop due to the uncompensated resistance [69]. The entire set of nonlinear equations is then solved using the hybrid method adapted from MINPACK [70], [71], [72].

The simulation results are then the total current, the corrected potential and both the surface and dissolved concentration profiles, both of which can be plotted with the ElectroKitty base class.

3.1.4 The optimization_controller and optimization_routines classes

The two classes are presented together, as the controller module calls the optimization_routines module, and is thus useless without it. The optimization_routines is a class that contains the Nelder-Mead algorithm [73], the CMA-ES algorithm was adapted from [74], as well as a wrapper function for the CMA-ES from the cma Python implementation [74], [75]. The class containing the algorithms is free of any design specifics of ElectroKitty and as such the routines can be called separately. The optimization_controller communicates between the base class and the routines and ensures that everything is passed on correctly. In the presence of a loss function and an algorithm, the controller calls the correct routine and passes it the required information, which is either user-defined or automatically generated. After optimization, the controller returns the best parameters, which update the base object and generate the best simulation. The base class saves itself automatically after each optimization.

3.1.5 The loss_functions class

It is a fairly straightforward class whose only task is to calculate the value of a loss function given a simulator, a guess of the parameters and other information provided either by the user or by the base class. Currently, only two loss functions are implemented. One of these is the RRMSE for the total current difference and a harmonic average calculated from the 0^{th} harmonic up to a number specified by the user [60], [76]. These are currently the only ones implemented as previously they have both shown good performance [76]. Other loss functions might be added if a need for them arises in the community.

3.1.6 The MCMC_sampler class

This class contains the MCMC sampler based on the article [77], that presents an adaptive MCMC sampler, which minimizes the burn-in period. The class accepts as input the number of samples, the percentage of samples representing the burn-in period, the number of chains, and the optional bounds for the prior distribution. Other arguments may be passed, but the base class does this automatically. After running the sampler, a list of the computed Markov chains is created and returned to the base class. After sampling, the middle chain is calculated, the burn-in is discarded and the sampling parameters are updated. The base object also saves itself here.

3.2 Outlook

It should be acknowledged that ElectroKitty has both advantages and limitations when compared with established electrochemical simulation tools. It is neither as computationally efficient as MECSim or DigiElch, nor does it provide a graphical user interface like DigiElch. ElectroKitty is also currently limited to planar and RDE geometries and does not yet support more complex electrode shapes. However, it includes the ability to simulate the Frumkin isotherm, which is particularly valuable when modeling realistic systems that exhibit pseudo-capacitive behavior. For this reason, I believe ElectroKitty serves as an effective entry-level tool for quantitative electrochemical analysis and can help users better interpret experimental data through simulation.

To demonstrate the usefulness of the package, I examine three representative systems: Pt single-crystal electrodes, polycrystalline Ni, and nanoparticulate Ir. These examples illustrate how one might assign a reaction mechanism to experimental data and what types of conclusions can be drawn from such an analysis. Because these materials represent three distinct types of surfaces, the quality of the conclusions depends strongly on the assumptions made in constructing the model. As will become evident, the mean-field approach often yields an incomplete mechanistic picture, limiting the level of detail that can be inferred. The only true remedy is to adopt more sophisticated and computationally demanding models.

Chapter 4

Modelling Pt(111) Oxidation

4.1 Introduction to the Problem

Single-crystal surfaces provide model systems in which the assumptions presented in Chapter 2 are most likely to hold. In a mean-field framework, the central assumption is that the entire surface behaves uniformly, meaning that the measured signal represents an average response of an "average site". For single-crystal electrodes, this assumption is intuitively reasonable, as the surface consists predominantly of one element and a single crystallographic orientation. However, as we will see in this chapter, even in systems where such assumptions appear well justified, their actual validity can still be questioned.

Pt surfaces are currently the most active surfaces for both the oxygen reduction reaction (ORR), as well as the hydrogen evolution reaction (HER). With the former being the limiting reaction in fuel cell operation, this has garnered an interest in the fundamental understanding of why is Pt so particularly active. Thus, studies have emerged that link ORR behavior to surface oxidation or reduction [78], [79], [80], [81], [82], [83]. Single-crystal electrodes have been used to provide fundamental insights into the complex electrochemical mechanisms occurring in industrial-scale devices, such as fuel cells and electrolyzers. The Pt(111) surface is arguably one of the most extensively studied single-crystal electrodes in electrochemistry and electrocatalysis and is often used as a benchmark model system for understanding fundamental interfacial processes. Thus, historically, as well as recently, efforts have been made to explain the behavior of such a surface under potential control [84], [85], [86], [87], [88], [89], [90], [91], [92], [93], [94], [95], [96], [97].

Even though the electrode has been studied to this degree, there are still a lot of uncertainties about its behavior, one of which is a clear explanation of the mechanism behind the oxidation of this surface [85], [86], [87], [93], [98], [99]. Besides experimental efforts, a lot of theoretical work has been done since the Pt(111) was first studied. Some of the earlier studies focused more on an atomistic description, such as the work of Rossmeisl and Koper [100], [101]. Later work by Eikerling et al and Peng et al preferred a mean-field model to explain the oxidation behavior of the Pt(111) surface [98], [99]. The later models were developed using some of the experimental insights provided by Feliu et al, who proposed the idea of different types of water adsorption on the Pt(111) surface involving different surface sites [85], [86], [87], [93], [94].

The models by Peng et al and Eikerling et al [98], [99] present the oxidation of the Pt(111) surface as a continuum. This allows potential ranges to be assigned to individual oxidation stages. As illustrated by the models in the literature, the region between 0.5 V and 0.87 V (Figure 4.1) constitutes the hydroxide region. Above 1.0 V, the adsorbed hydroxides begin to oxidize further into adsorbed oxygen, which ultimately forms a surface oxide structure. This distinction is most clearly reflected in how the adsorption sites are defined in these models, where both sites begin adsorbing hydroxide in the lower potential region, and these are only further oxidized above 1.0 V.

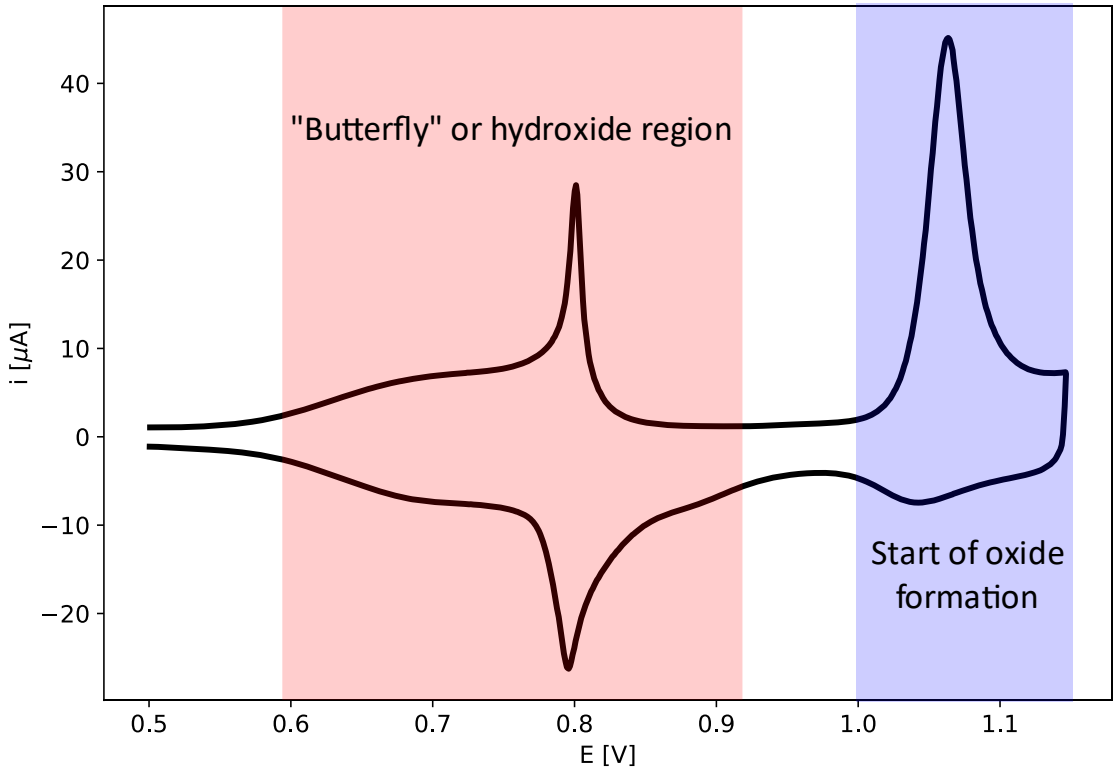


Figure 4.1: A typical experimental CV of Pt(111) in 0.1 M $HClO_4$, with a scan rate of 50 mVs^{-1}. It shows the "butterfly" feature between 0.55 V and 0.85 V, and the oxide peak at 1.05 V.

Curiously, somewhat contrary to this, publications by Feliu et al [102], [103], [104], argue that the oxide peak is in fact a two-step reaction. In their paper, they propose a mechanism for the oxide peak, which served as inspiration for the formulation presented here. One of their claims is also that the oxide peak could be due to a nucleation and growth mechanism. However, testing the proposed model, it can be found that that is likely not the case, as using the equations they proposed would result in the whole peak being consumed during a potential hold [85], [87], [94], [105], [106], [107], [108], [109], [110]. This is not the case, as is experimentally shown in their paper [87].

The main assumption differentiating this work from previous publications is that the butterfly peak can be described quantitatively by assuming only one type of active site, as in earlier theoretical studies [100], [101], rather than two distinct surface species occupying two distinct active sites. The OH species adsorbed in the initial step form a disordered phase, as the adsorption sites are chosen randomly. As more OHs are adsorbed or by hopping across the surface, they begin to form an ordered phase. This order-disorder reaction occupies roughly one-third of the surface coverage and is responsible for the butterfly peak. It can therefore be questioned whether two active sites are in fact needed to reproduce the butterfly, a claim made by other groups [93]. The influence of anions or other contaminants on the butterfly shape can in this case be attributed to their effect on either the kinetic or interaction parameters, a more intuitive explanation than invoking a two-site model, which was originally proposed precisely to account for such effects.

Another important consequence is that the model shows that a large overpotential is needed for additional OH adsorption after the butterfly, and it has already been speculated that anions block the remaining surface [111]. The model itself offers little explanation on the atomic scale as to why or how this happens, but an important consequence is that the oxidation of OH into O happens almost immediately, giving rise to the slope of roughly 38 mV/decade in the Laviron plot [103].

The final consequence is that one does not need to assume a 2-electron reaction for the oxide reduction [98], [99]. From modeling, it is found that a 1-electron reaction is enough to sufficiently describe reduction features. The model still agrees with others that it is not the oxide that is immediately formed that reduces back into either hydroxide or bare Pt, but that it is the place-exchanged oxide that undergoes electrochemical reduction.

4.2 Experimental Details

All measurements were performed in 0.1 M perchloric acid (UltraPure) using a BioLogic potentiostat. The Pt(111) electrode was first flame annealed for two times for 2 min with propane torches. After each annealing step, the electrode was cooled in a 1:1 mixture of argon and hydrogen gas. The electrode was left to cool down until room temperature, or about 10 minutes. After the annealing procedure, a droplet of water (MiliQ water) was deposited on the entire electrode surface to avoid any contamination coming onto the surface. All electrochemical measurements were done with a hanging meniscus setup, with a Pt wire serving as a counter electrode. The reference electrode used was a Hydroflex RHE electrode, and all potentials are reported versus RHE.

It was also reported that the Pt(111) surface roughens if the electrode is cycled repeatedly to potentials above 1.15 V [112], [113], [114]. To investigate if this is also the case for potentials below 1.15 V, in situ STM imaging of the surface was performed. In Appendix A.2, the before and after images of the surface are included, demonstrating that no appreciable changes have occurred. This is important, as this indicates that a model does not need to take in to account surface restructuring or other modifications.

4.3 Kinetic Model

The kinetic model employed is based roughly on the findings of references: [98], [99], [102], [103], but the model is formulated in a different way. These studies show that accurately describing the experimental observations requires the inclusion of at least two distinct surface sites. The first site (Pt_I^* in equation set 4.1) is associated with the "butterfly" peak. This peak is described as OH adsorption into a disordered phase ($\mathsf{Pt_IOH}^*_\mathsf{dis}$, equation 4.1a), which then equilibrates with the ordered adsorbed hydroxides ($\mathsf{Pt_IOH}^*_\mathsf{ord}$, equation 4.1b), leading to the occurrence of the "spike" in the voltammogram [101], [115]. The OH-covered surface is stabilized with anions, leading to a potential range of about 100 mV, where one can notice only the capacitive current, and any other contributions are due to surface defects as discussed by Feliu et al [102], [103], [104], [111]. Thus, a high overpotential is needed to break the ordered structure and continue the oxidation process. Further oxidation of the site (into $\mathsf{Pt_IO}^*_\mathsf{ord}$ species) occurs at potentials higher than 1.0 V (equation 4.1c). The reaction in equation 4.1c is the one responsible for the broadening of the underlying current at higher potentials up to 1.15 V.
The second site is responsible for the "oxide" peak found at around 1.05 V [98], [99], [102], [103], [104]. This site ($\mathsf{Pt}_\mathsf{II}^*$) immediately goes through a two-stage oxidation via OH ($\mathsf{Pt_{II}OH}^*$) into O ($\mathsf{Pt_{II}O}^*$), shown in equations 4.1d and 4.1e. Equation 4.1e is written as irreversible, so as to prevent the reduction of this particular oxide, simulate surface ageing. The surface O created via this path is then place-exchanged with surface Pt, forming $\mathsf{OPt}^*_\mathsf{pe}$ (equation 4.1f), and the assumption is that an equilibrium between the place-exchanged and non-place-exchanged species forms. This place-exchanged Pt is stabilized by the oxygen created via the first path to form PtOOPt^* (equation 4.1g), as proposed in previous studies [99]. The only way for the site to restore itself is by reducing the place-exchanged $\mathsf{OPt}^*_\mathsf{pe}$, shown by equation 4.1h, to form the surface hydroxide. The main reason for such a complex scheme is to try and reproduce the Laviron slopes of the negative-going scans, as they are likely the consequence of an irreversible step [103].

$$\mathrm{Pt}_\mathrm{I}^* + \mathrm{H_2O} \rightleftharpoons \mathrm{Pt_IOH}^*_\mathrm{dis} + \mathrm{H}^+ + \mathrm{e}^- \tag{4.1a}$$

$$\mathrm{Pt_IOH}^*_\mathrm{dis} \rightleftharpoons \mathrm{Pt_IOH}^*_\mathrm{ord} \tag{4.1b}$$

$$\mathrm{Pt_IOH}^*_\mathrm{ord} \rightleftharpoons \mathrm{Pt_IO}^*_\mathrm{ord} + \mathrm{H}^+ + \mathrm{e}^- \tag{4.1c}$$

$$\mathrm{Pt}_\mathrm{II}^* + \mathrm{H_2O} \rightleftharpoons \mathrm{Pt_{II}OH}^* + \mathrm{H}^+ + \mathrm{e}^- \tag{4.1d}$$

$$\mathrm{Pt_{II}OH}^* \rightarrow \mathrm{Pt_{II}O}^* + \mathrm{H}^+ + \mathrm{e}^- \tag{4.1e}$$

$$\mathrm{Pt_{II}O}^* \rightleftharpoons \mathrm{OPt}^*_\mathrm{pe} \tag{4.1f}$$

$$\mathrm{OPt}^*_\mathrm{pe} + \mathrm{Pt_IO}^*_\mathrm{ord} \rightleftharpoons \mathrm{PtOOPt}^* \tag{4.1g}$$

$$\mathrm{OPt}^*_\mathrm{pe} + \mathrm{H}^+ + \mathrm{e}^- \rightarrow \mathrm{Pt_{II}OH}^* \tag{4.1h}$$

The kinetic model uses the Butler-Volmer equation, with the Frumkin isotherm to account for interactions between the different surface species. The rate law is shown in Equation 4.2, written generally. For each reaction in the mechanism, the parameters are taken accordingly, with "i" adopting the species name. The "step" indicates for which step the rate constant is relevant, and for electrochemical reactions, they are denoted as the forward and backward rate constants. Other parameters found in the equation set are the E^0 as the formal potential, the E_{app} as the applied potential, R_{u} as the uncompensated resistance, and I as the total current. The g is the interaction parameter, and θ is the surface coverage, with α being the charge transfer coefficient. The other constants are F as the Faraday constant, R as the gas constant, and T as the temperature of the experiment. Finally, the computed rate constant is plugged into equation 4.2c, which is then used by equation 4.2d to compute the time evolution of the coverages.

$$k_{\text{forward,step}} = k_{0,\text{step}} e^{-\alpha \frac{F}{RT}(E^0_{\text{step}} - E_{\text{app}} - R_{\text{u}} I)} e^{-g_{\text{step},i}\theta_{\text{step},i}} \tag{4.2a}$$

$$k_{\text{backward,step}} = k_{0,\text{step}} e^{(1-\alpha) \frac{F}{RT}(E^0_{\text{step}} - E_{\text{app}} - R_{\text{u}} I)} e^{-g_{\text{step},i}\theta_{\text{step},i}} \tag{4.2b}$$

$$k_{chemical,step} = k_{chemical,step} e^{-g_{step,i}\theta_{step,i}} \tag{4.2c}$$

$$\begin{aligned} \frac{d\theta_i}{dt} = &- \sum_{\text{step}} k_{\text{forward,step}} \theta_j + \sum_{\text{step}} k_{\text{backward,step}} \theta_j \\ &- \sum_{\text{step}} k_{\text{chemical,forward,step}} \theta_j + \sum_{\text{step}} k_{\text{backward,chemical,step}} \theta_j \end{aligned} \tag{4.2d}$$

$$I = I_{C\text{dl}} - \sum_{\text{step}} k_{\text{forward,step}} \theta_j + \sum_{\text{step}} k_{\text{backward,step}} \theta_j \tag{4.2e}$$

To simulate the data, the code in the simulator in ElectroKitty has been modified to allow allocation of isotherm parameters for each species to be present in the rate law for each reaction. From there, the mechanism was coded into ElectroKitty [31] and fit using the CMA-ES algorithm [52], [116]. The double-layer capacitance and the ohmic potential drop were also taken into account by ElectroKitty. The loss function for the CMA-ES was constructed as the average RRMSE value using three CVs with different scan rate values. All found parameters can be found in the code found in Appendix A.1. The modified ElectroKitty code can be found in the project's GitHub page [30].

4.4 Modeling Results and Discussion

First, the model is compared with cyclic voltammograms recorded at different scan rates. For ease of comparison, the experimental data are normalized by both the scan rate and the electrode area. The experimental results are shown in Figure 4.2a, and a noticeable mismatch with the simulated curves in Figure 4.2b can be observed. Nevertheless, the model captures the main qualitative features of the CVs reasonably well.

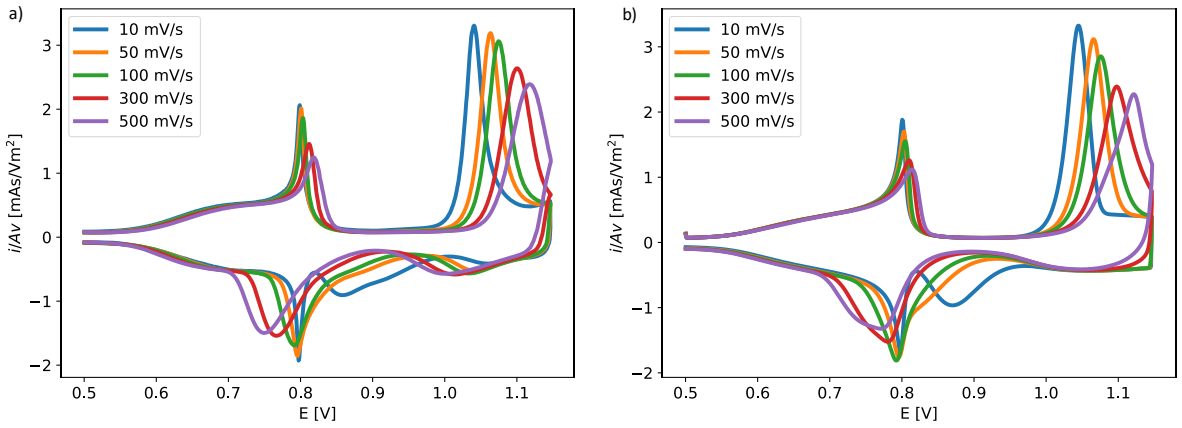


Figure 4.2: Comparison of pseudocapacitances of experimental and simulated CVs at different scan rates. a) Experimental results obtained at different scan rates as indicated in the legend. The voltammograms were measured using a Pt(111) electrode in 0.1 M $HClO_4$, in the potential region between 0.45 V and 1.15 V. b) Simulated results from the fitted model shown at different scan rates.

Further comparison can be made with the voltammogram taken at different vertex potentials. The vertex potential was continuously increased from 0.87 V up to 1.15 V, with a scan rate of 50 mVs^{-1}. The experimental behavior is the same as in the articles of Gomez et al [102], [103], [104]. The simulated response at identical conditions reproduces the same behavior seen in the experiment. The comparison is not ideal; however, the general reduction peak behavior is captured well by the model, seen in Figure 4.3.

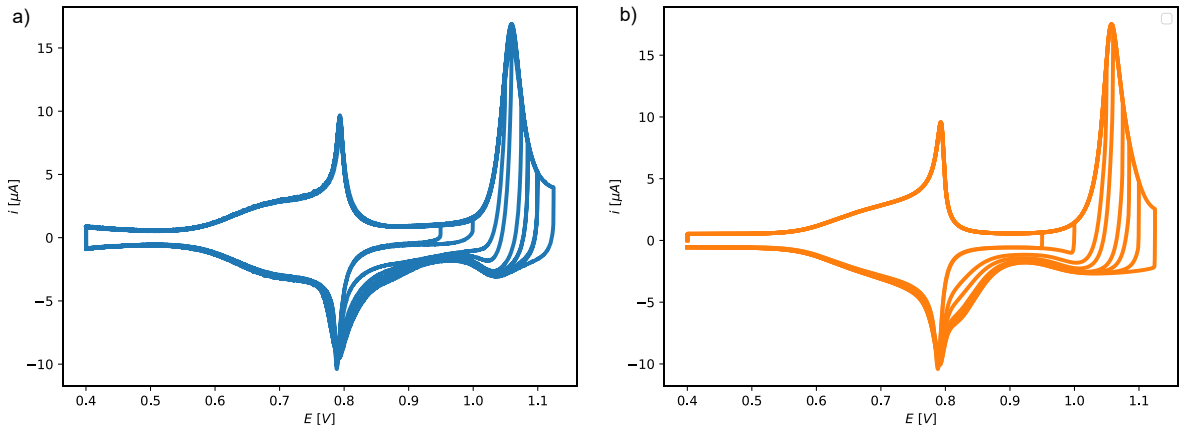


Figure 4.3: a) The experimental response of continuously changing the vertex potential when measuring a Pt(111) electrode in 0.1 M $HClO_4$. b) The simulated response of the fitted model, using the same potential program as in the experiment.

An alternating-current voltammetric measurement was also performed, a version of which is explained in Chapter 6. The potential was scanned between 0.45 V and 1.15 V at 50 mV s^{-1}, with a 5 mV sinusoidal perturbation at 70 Hz superimposed on the linear ramp. As shown in Figure 4.4, the DC component of the response is well reproduced, matching the behavior observed in the CV experiments. However, discrepancies are observed in the first harmonic response. Although the overall shape and the hysteresis near 1.0 V are captured, the detailed form differs from the experimental data. It should also be noted that, within the model, the behavior beneath the oxide peak is attributed to pseudo-capacitive contributions rather than purely capacitive currents.

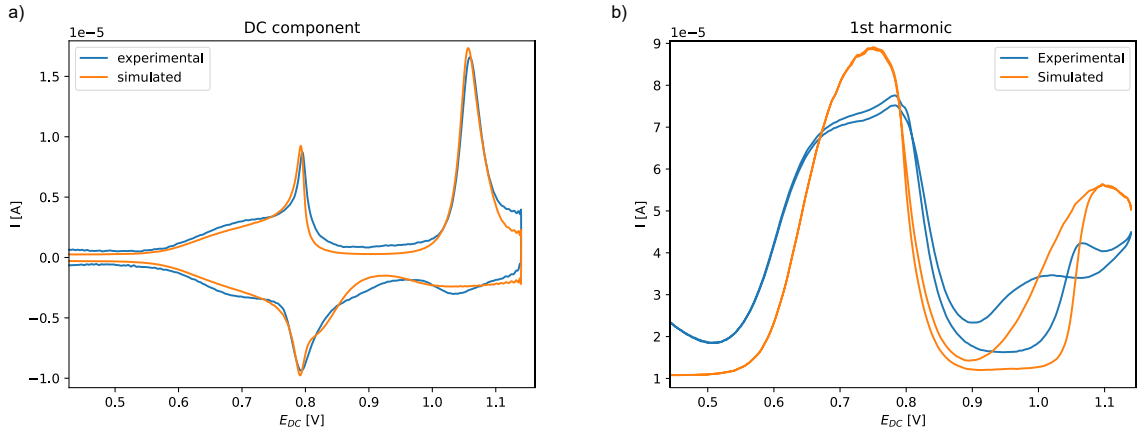


Figure 4.4: a) The comparison between the experimental and simulated responses of the DC component. b) Comparing the experimental and simulated responses of the 1st harmonic. The potential is scanned between 0.45 V to 1.15 V, with a scan rate of 50 mVs^{-1}, with the amplitude and frequency of 5 mV and 70 Hz respectively.

Another important comparison is provided by the potential-hold experiments. In these tests, the electrode is held at several potentials near 1.0 V, as shown in Figure 4.5, with each potential maintained for 2 minutes. A defining feature of the Pt(111) oxide peak is that, during a potential hold, a transient peak is produced whose magnitude and decay time depend on the applied potential. Overall, only partial agreement is obtained between simulation and experiment. Although the general peak behavior is reproduced reasonably well, a clear mismatch becomes apparent for the peak magnitudes and once the current begins to relax. The initial spike visible in the experimental traces is likely caused by the potentiostat as it transitions into the hold step. In case of simulated data, the spike is likely due to small numerical error. In Appendix A.3, a comparison is also included in which the hold potentials were decreased by 2.5 mV to examine whether the discrepancy could originate from a simple experimental offset. As shown there, the quantitative agreement improves, suggesting that the simulations remain within the range of experimental uncertainty. Despite these limitations, the qualitative features of the underlying mechanism are still captured by the model. Furthermore, it should be noted that, despite the discrepancies, the present model reproduces the potential-hold behavior more accurately than the model previously reported by Peng et al. As illustrated in Appendix A.4, their model does not successfully capture the transient peak characteristic of this experiment.

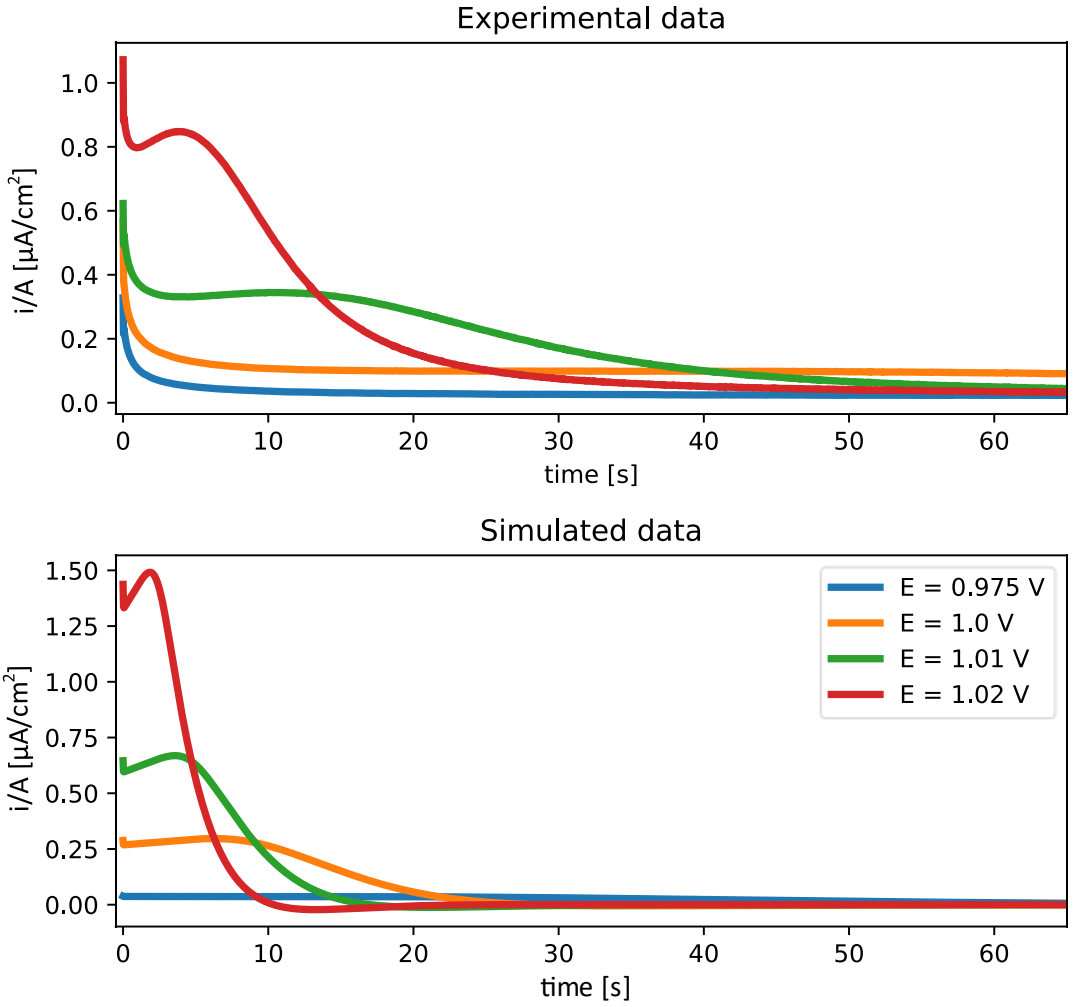


Figure 4.5: Comparison between simulated and experimental potential holds for a Pt(111) electrode in $HClO_4$. The potential was swept up to the indicated potential with a sweep rate of 50 mVs^{-1} and then held at that potential for 2 min. The potentials are shown up to 60 s, as no other interesting features can be observed after. a) The measured chronoamperometry. b) Simulated chronoamperometry following the same experimental procedure.

The modeled mechanism is able to quantitatively or, at the very least qualitatively, describe different experimental responses. Previous efforts to simulate the Pt(111) oxidation peak have focused exclusively on fitting the CV. Here, the model was applied to other types of experiments, such as potential holds and AC voltammetry, testing its extrapolative capabilities and helping to close the gap between experimental and theoretical insights.

4.5 Concluding Remarks

In conclusion, a mechanism was developed that is capable of qualitatively describing the redox behavior of a Pt(111) surface in the potential range of 0.4–1.15 V. The simulation reproduces trends observed when changing the scan rate and upper vertex potential in voltammetry, as well as the general behavior during potential holds, allowing it to fairly accurately predict the electrochemical behavior of Pt(111) electrodes. The proposed mechanism provides two important insights pointing toward a complex mechanism for the oxidation of Pt(111). The first concerns the "butterfly" peak: both prior theoretical work and this work indicates that OH adsorbs on a single type of site, existing in a dynamic equilibrium between ordered and disordered surface phases. The second concerns the "oxide" peak, which is likely associated with additional OH adsorption. Because this occurs at high potentials, the newly adsorbed OH is converted to O almost immediately. The resulting oxygen then undergoes further transformations as the surface restructures, potentially acting as a precursor for surface restructuring [117], [118], [119].

The model does, however, approach the practical limits of mean-field descriptions. It is difficult to identify which specific surface atoms act as active sites or how those sites are distributed on the surface. As previously alluded to, anions also contribute to surface oxidation in ways that cannot be reasonably captured by a mean-field model. This points to the need for more sophisticated approaches going forward, such as kinetic Monte Carlo simulations or other atomic-level methods.

Studying single-crystal materials nonetheless yields many valuable insights. Knowing the percentage of the surface that participates in the reaction, combined with mechanistic insight from the model, allows for some conclusions to be drawn about surface behavior. It is reasonable to speculate that different hydroxide phases may coexist simultaneously, that at least two distinct adsorption sites exist, and that these eventually combine to form surface oxide; conclusions that, while not unreasonable, should ideally be corroborated by complementary techniques. Some limitations remain inherent to the approach: the fitted kinetic and thermodynamic constants do not by themselves provide additional structural information about the surface, and ideally these parameters should be compared to those of similar systems to identify potential correlations.

Chapter 5

Modeling Polycrystalline Ni Surface

5.1 Introduction to Ni Electrochemistry

In this chapter, the focus shifts to polycrystalline electrodes, which in many ways represent a good link between fundamental and applied studies, as the surface structure should be similar at both lab and industrial scale. However, polycrystallinity does pose challenges for fundamental studies. For single-crystal electrodes, the majority of the surface shares a single orientation, meaning the observed signal can be attributed to it with confidence. This is not the case for polycrystalline electrodes, where many different orientations are present and defects are more common, making it difficult to assign the signal to any single, microstructure or type of defect. That said, certain orientations may still dominate, which aids in interpreting the signal, as its origin can at least partially be attributed to specific surface features. The polycrystalline material studied here is Ni, which has attracted growing interest in recent years and is already used in various electrochemical applications and it is on this basis that the chapter explores what information can be gained by assigning a reaction mechanism to polycrystalline electrodes.

Nickel-based materials are central to electrochemical energy storage and conversion technologies, including alkaline water electrolyzers, rechargeable batteries, and fuel cells. Their low cost, abundance, and stability under alkaline conditions have made Ni a preferred electrode component for decades [120], [121], [122], [123]. Beyond their technological importance, Ni electrodes serve as model systems for studying metal–(hydr)oxide interfacial processes, where surface oxygen species dictate the structure-function relationship, particularly in the hydrogen and oxygen electrode reactions [90], [124], [125], [126]. For example, recently a quantitative correlation was established between individual Ni species and hydrogen evolution reaction (HER) activity, showing that NiO behaves as a passive spectator, irreducible $Ni(OH)_2$ enhances HER by promoting water dissociation, and NiH_x inhibits HER [125]. Despite extensive work, the fundamental mechanism of Ni oxidation remains unsettled, particularly the initial transformation from metallic Ni to $Ni(OH)_2$, a critical step that governs subsequent hydr(oxy)oxide growth and surface evolution under operating conditions [127], [128], [129], [130], [131], [132], [133].

Understanding this process has challenged researchers for decades. Early work by Bode and co-workers [134] proposed a simple sequence in which Ni oxidizes to $Ni(OH)_2$, which then converts to oxyhydroxide (NiOOH). Later studies by Burke et al [135], [136], [137], [138], [139] and Oshchepkov et al [127], [128], [129] support the so-called direct adsorption model, in which $Ni(OH)_2$ forms via surface-limited electrosorption. Alternative explanations include the place-exchange model [131], [132], [140], [141], [142], [143], where Ni atoms and oxygen species swap positions, resulting in logarithmic oxide growth; dissolution–precipitation mechanisms [140], [144] involving brief Ni dissolution followed by redeposition as hydroxide; and nucleation-and-growth model [133], [144] which envisions the formation of hydroxide islands spreading across the surface. Figure 5.1 summarizes these concepts. While each explains some experimental observations, no consensus has been reached, and the actual pathway likely depends on the earliest stages of oxide formation, which remain difficult to observe experimentally.

This Chapter addresses this long-standing confusion by directly testing mechanistic models against electrochemical experiments using ElectroKitty [30], [31]. By comparing simulated and experimental responses across scan-rate dependence, switching-potential protocols, and potential-hold experiments, the mechanism is systematically evaluated and developed.

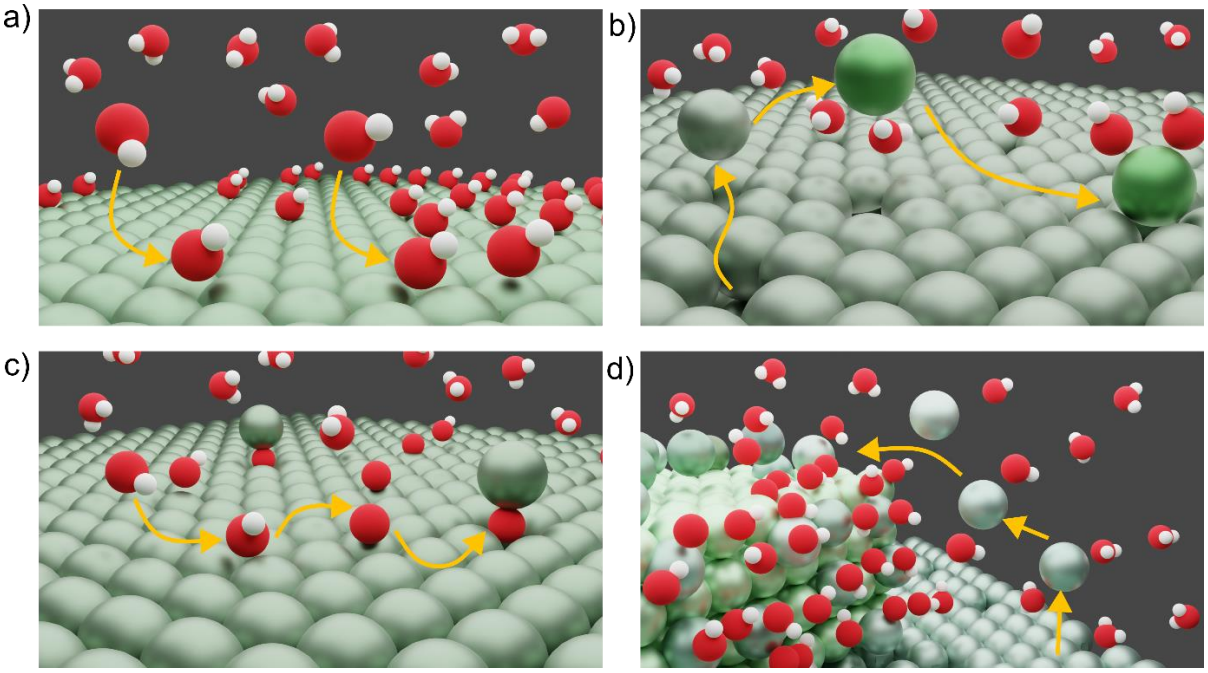


Figure 5.1: Schematic illustration of proposed mechanisms for Ni oxidation in alkaline media. a) Direct adsorption model, in which OH adsorbs on the Ni surface and forms a surface monolayer. b) Dissolution and precipitation model, where surface Ni atoms oxidize first, then dissolve into the solution, and subsequently redeposit to form a Ni hydroxide layer. c) Place-exchange model, in which hydroxide ions in solution initially adsorb on the surface; prior to completion of a full monolayer, O atoms react with surface Ni atoms, followed by exchange between O and Ni. d) Nucleation and growth model, which assumes that Ni hydroxide forms via discrete structures that grow outward, rather than a uniform layer.

5.2 Experimental Detail

5.2.1 Chemicals and materials

Potassium hydroxide (KOH, 99.995%) was purchased from Sigma Aldrich. Electrolytes were prepared using ultrahigh-purity deionized (DI) water (Milli-Q Millipore; resistivity >18.2 M Ω cm). Research-grade Ar (6N) and an Ar-H_2 mixture (6N) were obtained from Messer. The nickel rod used as the working electrode (American Elements) had a purity of 5N. A typical three-compartment fluoroethylene propylene (FEP) electrochemical cell was used to avoid contamination from glass in alkaline media [126]. To prevent cross-contamination between experiments, the cell was thoroughly rinsed with DI water and then boiled with DI water before each set of measurements.

5.2.2 Surface preparation of polycrystalline nickel electrodes

Polycrystalline Ni electrodes (6 mm diameter) were mechanically polished using SiC papers and diamond suspensions down to 0.25 µm, followed by sonication and rinsing with DI water. The electrodes were then inductively heated for 10 minutes at ~1300 K in an argon-hydrogen flow (3% hydrogen) [125], producing an atomically flat surface. After annealing, the electrodes were cooled to room temperature under inert gas and immediately covered with a droplet of DI water to prevent airborne contamination. They were subsequently assembled into the rotating disk electrode (RDE) setup.

5.2.3 Electrochemical measurements

The Ni electrodes, mounted in the RDE, were transferred into a standard three-electrode cell containing 0.1 M KOH. Prior to each measurement, the electrode was immersed under potential control (0.0 V_{RHE}) in Ar-saturated electrolyte. Immersion at open-circuit potential (≈0.5 V) would otherwise lead to the spontaneous formation of irreversible (hydr)oxide species, commonly referred as β-$Ni(OH)_2$. As a result, such oxidation would partially block the surface and interfere with resolving the initial stages of Ni oxidation. The metallic nickel (Ni^0) surface was prepared by first reducing the air-formed (hydr)oxide layer at –0.4 V vs. RHE, followed by oxidation of the hydride species formed during the reduction step by holding the potential at 0.3 V for 20 min. The electrode was then subjected to a cathodic sweep to –0.15 V and subsequently to anodic sweeps at the desired scan rates and potential windows specified in the text. This strict surface conditioning ensures highly reproducible and reliable measurements [126]. A high-purity Ni wire (99.999%, Thermo Fisher Scientific) and a bridged Ag/AgCl reference electrode (BASi) served as the counter and reference electrodes, respectively. All potentials are reported versus the reversible hydrogen electrode (RHE). Measurements were performed using a PalmSens4 potentiostat, with RDE experiments conducted on a Pine Modulated Speed Rotator. Sweep rates ranged from 10 to 3000 mV s^{-1}, with rotation speeds of 3600 rpm. All experiments were carried out at ambient pressure and room temperature.

5.3 Results and Discussion

Three sets of experiments were carried out to probe the initial oxidation of Ni under alkaline electrochemical conditions:

1. **Scan rate dependence** – The signal was analyzed in terms of pseudo-capacitance to assess the effect of scan rate on Ni oxidation.
2. **Gradual increase of switching potential** – The switching (limiting) potential in the voltammograms was progressively extended to examine how the accessible potential range affects the oxidation process.
3. **Effect of potential-hold duration on cathodic current** – A fast anodic scan was recorded to a holding potential of 0.25 V vs. RHE for varying durations, followed by a slow cathodic scan to assess how the hold time influences the Ni surface reduction behavior.

The pseudocapacitance, calculated from the cyclic voltammetry current normalized by the scan rate (i/v), was plotted and examined as a function of scan rate. The exponential current contribution at negative potentials, associated with the hydrogen evolution reaction (HER), was subtracted from the recorded voltammogram to isolate the relevant pseudocapacitive response (Appendix B.1). In general, a linear i–v dependence, manifested as constant pseudocapacitance, indicates a surface-limited process, whereas deviations from linearity suggest diffusion limitations or multi-step redox reactions.

As shown in Figure 5.2a, anodic pseudocapacitive peak heights remain nearly constant with scan rate, consistent with surface-limited behavior (Appendix B.2 and B.3). In contrast, cathodic peaks grow with decreasing scan rate, indicating kinetic limitations during reduction. At lower scan rates, both anodic and cathodic traces reveal two distinct electrochemical processes: the anodic peak broadens and flattens, while a new cathodic feature emerges around –0.1 V. Together, these observations suggest that Ni oxidation and reduction proceed through multiple sequential steps rather than a single elementary reaction.

It is also noted that, except at the highest scan rate, the anodic current relaxes into a limiting value at potentials above 0.4 V, which might suggest diffusion limitations. However, when the potential is reversed at 0.55 V, the current drops almost instantaneously to zero, indicating at least partial irreversibility of the electrochemical reactions. Under diffusion control, the current would persist upon reversal; for a purely Nernstian pseudocapacitive response, it would immediately become negative.

The influence of the switching potential on the cathodic current response was next examined. Shown in Figure 5.2b, the cathodic current increases with higher switching potentials, reflecting the greater amount of Ni hydroxide formed during the anodic sweep and subsequently reduced upon reversal. The cathodic region in 5.2a and 5.2c shows that two processes are present in the cathodic region. Which of these occurs can also depend on the switching potential of the experiment. This suggests that the reduction path observed in the cathodic current depends on the degree of surface oxidation, i.e. the amount and type of different oxidized species.

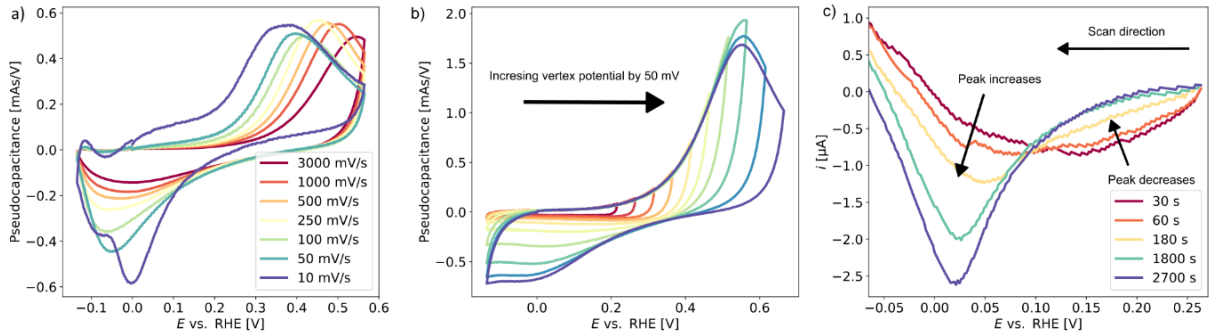


Figure 5.2: Electrochemical probing of the initial stages of Ni (hydr)oxide formation. a) Pseudocapacitive response of Ni as a function of scan rate (10, 50, 100, 250, 500, 1000, and 3000 mV s^{-1}). b) Cyclic voltammograms recorded with increasing anodic vertex potential from 0.20 to 0.75 V. c) Negative-going scans from 0.255 to −0.15 V at a scan rate of 10 mV s^{-1}; prior to each scan, the electrode was swept from 0.00 V to the starting potential of 0.255 V at 3 V s^{-1} and held for varying durations (30, 60, 180, 1800 and 2700 s). All measurements were performed in 0.1 M KOH using a polycrystalline Ni electrode.

Finally, a potential-hold experiment was performed to probe the presence of potential-independent (chemical) steps. While electrochemical steps reach equilibrium under a static potential, purely chemical transformations remain unaffected by it. To distinguish these contributions, a fast anodic scan (3 V s^{-1}) was applied before the potential hold. As shown in Figure 5.2c, two distinct cathodic features evolve with increasing hold duration, consistent with the behavior observed in the switching-potential experiments. The peak at around 0.17 V progressively diminishes, while the feature at around 0.025 V emerges and intensifies, indicative of a time-dependent surface transformation. This behavior points to the involvement of a slow or partially irreversible chemical process, as the cathodic peak continues to grow even at extended hold times. Note that the positive currents at –0.05 V are an artifact of the exponential fit subtraction and do not affect the qualitative interpretation of the data.

The following section aims to reproduce the observed experimental behavior through theoretical simulations, with the goal of developing a model that elucidates the mechanism of the initial stages of Ni oxidation in alkaline electrolytes.

5.3.1 Mechanistic models governing the initial stages of Ni (hydr)oxide formation

To evaluate the proposed mechanisms, ElectroKitty was used for all cases, excluding nucleation and growth mechanism [30], [31], which was implemented in Python following Seghiouer et al. [133]. In both approaches, the fitted parameters include the kinetic constants, the interaction parameters between surface species, and the maximum surface concentration. After fitting the model to a voltammogram recorded at 50 mV s^{-1}, the resulting parameters were used to simulate voltammograms at additional scan rates. This served as a validity test: a model that correctly captures the underlying mechanism should reasonably predict the system's behavior under new conditions, whereas systematic failure indicates that the assumed mechanism is incorrect. To gain insight into the early stages of Ni (hydr)oxide formation, the predictive performance of each mechanism was assessed, with a robust mechanism expected to reproduce the current–potential response across a range of conditions.

5.3.1.1 Dissolution/precipitation mechanism

First, the dissolution/precipitation mechanism is considered (the corresponding results are shown in Figure 5.3a), which has been widely applied in the corrosion field. In this model, surface Ni atoms (denoted by Ni^*) oxidize and dissolve into the electrolyte solution (equation 5.1a, where the solvated species is written as Ni^{2+}), leaving behind a surface vacancy (denoted by *). The dissolved species then bond with the hydroxide in solution (OH^-), forming Ni-hydroxide ($Ni(OH)_2{}^*$), which is deposited onto a free surface site (equation 5.1b).

$$Ni \rightleftharpoons Ni^{2+} + 2e^- + * \tag{5.1a}$$

$$Ni^{2+} + * + 2OH^- \rightleftharpoons Ni(OH)_2{}^* \tag{5.1b}$$

Although it is often assumed that this mechanism cannot produce a linear current–scan rate dependence, it can do so under certain conditions. The principal issue, however, is that when the solubility product (K_{sp}) of Ni hydroxide is properly considered, the cathodic current disappears, a consequence of the species strongly adsorbing onto the surface. For the hydroxide to be reduced, it must first dissolve, which does not occur in the simulation. The mechanism, therefore requires either further refinement or replacement with an alternative approach.

5.3.1.2 Nucleation and growth mechanism

Next is the nucleation and growth mechanism, reported by Seghiouer and co-workers [133], which is reproduced with Python code. For our discussion, the most relevant aspect is their treatment of the anodic peak, as the remainder of the system was described by rate law equations. However, as shown in Figure 5.3b, this model exhibits a major drawback, the anodic current peak is highly sensitive to even small variations in scan rate. The simulated anodic peak behavior can be attributed to the fact that new phase grows outward producing more sites for the reaction to take place. Since growth is considered potential independent in the model, this creates more sites at lower scan rates, since the new phase has more time to develop. Moreover, Jerkiewicz's group [130], [131], [132] demonstrated that impedance spectra of the Ni hydroxide peak do not align with those expected for a nucleation-growth process. Taken together, these findings cast serious doubt on the validity of the nucleation and growth mechanism.

5.3.1.3 Adsorption mechanism

The third mechanism considered is the adsorption model, which assumes that OH species electrosorb directly onto the Ni surface in two-dimensional arrays without involving Ni dissolution (equation 5.2a). The OH species in this case adsorb onto a group of surface atoms, with three Ni atoms forming a single site. Once such a layer is established, additional OH species adsorb according to equation 5.2b to achieve even higher coverages. In equations 5.2a and 5.2b, $Ni_3{}^*$ denotes a surface adsorption site, OH^- the dissolved hydroxide ions, and $NiOHNi_2{}^*$ and $Ni(OH)_2Ni_2{}^*$ the corresponding surface Ni site with adsorbed hydroxide. A similar framework has been widely used to model the anodic hydroxide peak, with numerous studies adopting an analogous formalism to describe surface Ni-hydroxide formation [127], [128], [129], [130], [131], [132], [145], [146]. In this mechanism, the hydroxide layer forms exclusively through two successive electrochemical adsorption steps, as described by equations 5.2a and 5.2b [127], [128], [129].

$$Ni_3{}^* + OH^- \rightleftharpoons NiOHNi_2{}^* + e^- \tag{5.2a}$$

$$NiOHNi_2{}^* + OH^- \rightleftharpoons Ni(OH)_2Ni_2{}^* + e^- \tag{5.2b}$$

While this mechanism shows promise—successfully reproducing much of the behavior observed at low scan rates (violet curve, Figure 5.3c) it still fails to capture the experimental response at higher scan rates (red and orange curves, Figure 5.3c). Nonetheless, it performs better than the previous models, suggesting that with suitable modifications, it could potentially match the full experimental trends. These shortcomings motivate the introduction of the place-exchange model, which can be viewed as an extension or refinement of the adsorption model, as surface adsorption remains the fundamental first step.

5.3.1.4 Place-exchange mechanism

The final mechanism considered is the place-exchange model (equations 5.3) [140]. This mechanism can be viewed as an extension of the adsorption framework, as it incorporates additional chemical steps and modified cathodic reactions, as well as two distinct pathways, one for oxidation and one for reduction. In the oxidation pathway, it is assumed that three adjacent surface Ni atoms form an active site onto which hydroxide adsorbs (the Ni_3 species in equation 5.3a). The adsorbed hydroxide is then further oxidized to form a surface oxide and water (equation 5.3b). This oxide is structurally unstable, leading to a place-exchange event in which the oxygen atom swaps positions with one of the underlying Ni atoms (equation 5.3c). This then provides an additional site for OH to adsorb, which forms the final state in this model (equation 5.3d). These steps occur in the positive-going scan and appear experimentally as a single peak, as they take place in rapid succession. Once the two atoms exchange position, reduction proceeds through a different pathway for this place-exchanged oxygen species. During the negative-going scan, the place-exchanged oxygen is first electrochemically reduced to a place-exchanged hydroxide (equation 5.3e), which is then further reduced to regenerate the metallic surface (equation 5.3f).

$$Ni_3{}^* + OH^- \rightleftharpoons Ni_3OH^* + e^- \tag{5.3a}$$

$$Ni_3OH^* + OH^- \rightleftharpoons Ni_3O^* + H_2O + e^- \tag{5.3b}$$

$$Ni_3O^* \rightleftharpoons ONi_3{}^* \tag{5.3c}$$

$$ONi_3{}^* + OH^- \rightleftharpoons ONi_3OH^* + e^- \tag{5.3d}$$

$$ONi_3{}^* + H_2O + e^- \rightarrow OHNi_3{}^* + OH^- \tag{5.3e}$$

$$OHNi_3{}^* + e^- \rightarrow Ni_3{}^* + OH^- \tag{5.3f}$$

As shown in Figure 5.3d, the place-exchange mechanism not only reproduces the dataset at low scan rates but also captures the trends at higher scan rates, in contrast to the previous models. Moreover, it successfully predicts the behavior observed during the potential-hold experiment (Appendix B.4). Overall, these results identify the place-exchange model as the most plausible mechanism for the initial formation of Ni hydroxide. This formulation is formed after evaluating numerous mechanistic variants, all of which were derived from the general framework represented by equations 5.3. In contrast, every other mechanism failed to reproduce the experimental behavior with sufficient accuracy. Only the present mechanism was capable of capturing the key trends across all conditions. The fitted kinetic parameters are provided in Appendix B.5, along with the simulation code and a plot illustrating the potential-dependent evolution of surface coverages.

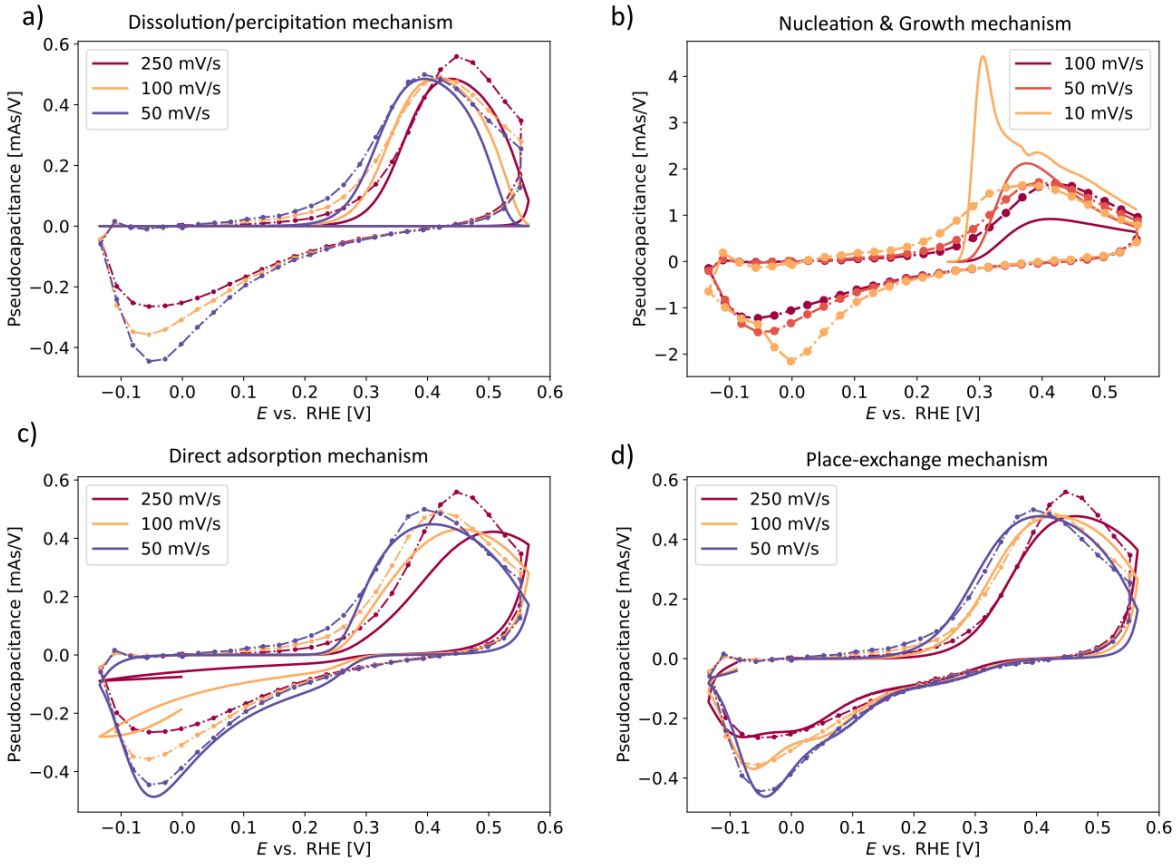


Figure 5.3: Comparisons between different models and experimental data. a) The dissolution-precipitation mechanism fitted onto experimental data taken at 50 mV s^{-1} and showed at higher scan rates as indicated in the Figure. b) The nucleation and growth mechanism presented in the text and in Ref [133] shows how it responds at different scan rates. c) The direct adsorption mechanism compared with experimental data at three different scan rates, as shown in the plot legend. d) The place-exchange mechanism and experimental data taken at three different scan rates. Both the place-exchange mechanism and the direct adsorption model were fitted onto experimental data at 50 mV s^{-1}, and then simulated at higher scan rates. Experimental data measured in 0.1 M KOH.

5.4 Conclusions

In this chapter, four possible mechanisms were examined to explain the initial stages of Ni oxidation. To evaluate them, any fitted model was required to demonstrate predictive capability to be considered viable. Each model was first fitted to a Ni cyclic voltammogram measured at 50 mV s^{-1}, then tested on whether the fitted parameters could reproduce the voltammetric behavior at higher scan rates. This analysis showed that only the place-exchange model captured the key features of the measurements across scan rates, and also correctly predicted the system's response during potential-hold experiments. It is therefore concluded that place exchange is the critical initial step governing the formation of Ni (hydr)oxide.

The place-exchange mechanism proposed here assumes oxidation beyond hydroxide formation. While the literature suggests that only Ni hydroxide forms in this potential region, the model appears to contradict this view. Such a contradiction cannot be confirmed by modeling alone, however, and should be substantiated with further experimental evidence, using a surface sensitive technique such as TOF-SIMS or forms of spectroscopy.

This chapter demonstrates that by carefully examining different mechanisms, the most likely candidate can be identified. However, working with polycrystalline electrodes comes at the cost of reduced structural resolution. Since the observed voltammogram represents a superposition of contributions from many different surface sites, only the surface-averaged behavior is captured. Information about the electrochemical behavior of individual orientations is therefore lost, and no firm conclusions can be drawn about how specific sites behave. What can be said is that three bare Ni atoms behave in roughly the manner described, but this raises further questions about the behavior of different surface orientations and their influence on catalytic reactions. Something which can only truly be resolved by a very precise experimental study.

Chapter 6

Modeling OER and Oxidation of Ir Nanoparticles

6.1 Introduction

This chapter attempts to understand nanoparticulate materials, a difficult task, as the analysis will show, due to the inherent limitations of the mean-field model. While techniques such as TEM can provide structural details about the electrode, probing the actual kinetic phenomena remains challenging. This is primarily due to the vast number of possible active sites, which may themselves change during a voltammetric experiment. Nonetheless, some general observations can still be made and quantified, as demonstrated here for the case of Ir-based nanoparticles used in water electrolysis. This chapter is based on the author's published article, with some modifications [147].

There have been many fundamental studies published on the topic of the electrochemical properties of Ir as an oxygen evolution reaction (OER) catalyst in acidic media, studied mostly on model systems [148], [149], [150], [151], [152], [153]. For bulk Ir electrodes, it has been shown that activation via electrochemical cycling continuously produces more and more porous Ir hydrous oxide (IrOH), which acts as the active phase for OER. Many studies, summarized in several reviews, [154], [155], [156], [157] have been dedicated to hydroxide formation and its effect on OER. In essence, by cycling bulk Ir material between a low and high voltage (usually between approximately 0 V and 1.5 V vs. RHE) the surface of Ir starts to irreversibly oxidize and thus restructure (e.g., formation of cracks) into a porous gel-like structure, referred to in the literature as a 3D catalyst. This is seen as a substantial growth of capacitive current with every cycle in cyclic voltammetry. This repetitive oxidation and reduction changes not only the morphology of Ir surface but also its electrochemical intrinsic properties, namely the electrochemically active surface area and the formation of specific OER active sites (turnover frequency) [154], [155].

Recently, Krewer et al [158], [159] employed a combined theoretical-experimental approach to study the OER mechanisms on different Ir systems. They fitted a microkinetic model based on DFT calculations to the measured cyclic voltammograms (CVs) of bulk Ir electrodes and IrO_2 nanoparticles. Their works showed that essentially all Ir-based catalysts share the same reaction pathway for OER.

Despite decades of fundamental studies on Ir electrocatalysis, not much work on understanding the Ir hydroxide formation has been done on Ir nanoparticles. Preparing various forms of Ir nanoparticulate catalysts, which can differ in many physical properties, comes with some lingering questions that are still not fully addressed in the literature. For example, how do the support and oxidation state of Ir affect the intrinsic properties of these Ir catalysts? Do different Ir-based catalysts need different activation treatments before reaching an active state? Do all Ir-based nanoparticles exhibit the same OER mechanism and possess the same intrinsic properties?

Voltammetric methods that are based on large amplitude alternating current (ACV) usually include a potential procedure where a sine wave of known frequency and amplitude is added to the conventional procedure of linear sweep or cyclic voltammetry experiment. With a sufficiently large amplitude, harmonics higher than the base frequency will occur. To date, the method has been applied in various fields of electrochemistry [58], [160]. Major advances and applications have been made by Bond et al [58], [160], [161], [162]. In particular, when the method is combined with a model-experiment comparison approach, it can prove to be a particularly powerful tool for understanding the electrochemical phenomena that occur on a catalyst surface [58], [162], [163]. This method can in principle effectively distinguish between Faradaic and capacitive currents, as harmonics are a consequence of only electrochemical reactions. These harmonics can then be filtered using the Fourier transform (FT). By analyzing the harmonics, the electrochemical reactions occurring on the Ir surface can be elegantly separated and thus analyzed. Such an analysis can provide a basis for discussion of the reaction pathway and intrinsic properties for different catalysts, such as supported Ir nanoparticles. On the contrary, conventional cyclic voltammetry is in most cases unable to distinguish between different electrochemical processes.

ACV is employed here to investigate how the initial oxidation state of Ir and the choice of support affect the intrinsic catalytic properties of Ir-based nanoparticles. Three materials are examined: unsupported Ir particles (Ir Black), rutile IrO_2, and Ir particles supported on Vulcan carbon. ACV measurements are performed and analyzed for each material before and after a series of potentiodynamic cycles. By comparing results across materials, it is possible to track how the mechanism and properties of each evolve with the number of activation cycles, and to determine how long each material takes to reach a steady state, referred to here as the activation threshold. Mechanistic simulations are then used to fit the experimental ACV results for the most active state of each material, from which OER mechanistic differences and similarities among the three materials are inferred. In particular, the hypothesis that all Ir-based materials share a common mechanistic pathway is tested.

6.2 Experimental

6.2.1 Materials and electrochemical characterization

Several materials with supported and unsupported Ir-based nanoparticles were used. Two commercial samples, namely Ir Black (Alfa Aesar) and Ir on Vulcan (20% Ir, Premetek) were compared to in-house synthesized IrO_2 nanoparticles.

Iridium oxide nanoparticles were prepared by thermal treatment of an iridium precursor in a silica template, which was subsequently removed. For this purpose, 0.4 g iridium(III) bromide hydrate (Sigma-Aldrich) was first dissolved in 10 mL of water at 50 °C. The solution was then mixed with 3 g of fumed silica (Cab-O-Sil M-5, Cabot Corporation) at 50 °C until evaporated (lightly ground in a mortar). The mixture was then thermally treated in air, raising the temperature to 500 °C at a rate of 2 °C per minute for 10 hours, and then cooled to room temperature. The silica matrix was then removed from the thermally treated mixture by first dissolving it in 60 ml of 6 M NaOH at 60 °C and followed by centrifugation at 7000 rpm for 15 minutes and washing with water four times. Preparing the oxide material in this way allows better control of nanoparticle size. X-ray spectra and sample analysis are available in Appendix C.1.

All electrochemical measurements were performed in a standard glass cell with three electrodes and a Biologic SP-300 potentiostat. The electrodes used were a graphite counter electrode, a HydroFlex reversible hydrogen electrode (RHE) (Gaskatel GmbH) reference electrode, and glassy carbon (GC) rotating disc electrode (RDE) from PINE as a working electrode, to which thin films of the investigated materials were deposited by drop casting. All potentials are given against RHE. Before the experiment, the cell was boiled in distilled water for 1 h and then thoroughly rinsed with Milli-Q water (18.2 MΩ cm). To ensure maximum purity of the working electrodes, the GC discs were polished with an alumina suspension (0.05 µm, MasterPrep, Buehler) and afterward washed by sonication in water for 5 min three times. The electrodes were then rinsed with water and dried under N_2 atmosphere. For the deposition of thin films on RDEs, suspensions containing different concentrations of Ir-based samples were prepared by weighing a material on a mg scale and then adding a suitable amount of water. In addition, a Nafion stock solution (Aldrich) was added to the suspension so that the amount of Nafion was 25 wt% of the solid content in the suspension. The ink was homogenized by sonication in an ice bath with a sonication horn (4 s pulse, 2 s pause) for 20 min. The prepared suspension was drop cast onto a clean and dry working electrode, which was then left to dry overnight in a closed plastic desiccator.

Hydrous Ir oxide films were prepared by 100, 200, 500, and 1000 square wave pulses (SQW) between 0.05 and 1.45 V (2s steps). The supporting electrolyte was 0.1 M perchloric acid ($HClO_4$, 70% Rotipuran Supra, Carl Roth, diluted with water). ACV and LSV scans were performed before and after each set of cycles. The ACV scans were performed at a scan rate of 1 mV/s from 0.4 V to 1.5 V. The sine wave was constructed with a frequency of 0.127 Hz and an amplitude of 150 mV. This provided a sufficient signal-to-noise ratio. The harmonics were filtered out as discussed in the literature [58]. A potential window between 0.4 V and 1.6 V was used for the LSV scan, with a scan rate of 5 mV/s.

6.3 Model

The model used is the one reported in previous articles [158], [159]. They constructed a model based on DFT calculations performed by other groups and linked the calculations to experimental findings. The proposed mechanism is composed of four electrochemical and three chemical steps. The first reaction step is a chemical one representing the adsorption of water on the electrode (denoted as 6.C1). This is followed by two electrochemical deprotonation steps (6.E1 and 6.E2), a chemical water adsorption step (dubbed 6.C2), and the last two electrochemical deprotonation steps (6.E3 and 6.E4). All the steps described are connected by the final chemical step of oxygen desorption which completes the reaction cycle (6.C3).

The active site in this reaction scheme, denoted as "*", is believed to be an exposed Ir atom on the surface, though no further assumptions can realistically be made. The kinetics of an active site are influenced not only by the atom at which the reaction occurs, but also by its local surroundings. Different kinetic parameters are therefore expected for the metallic and oxide materials. For metallic Ir samples, an amorphous hydrous oxide is expected to form on the surface, whereas electrocatalysis on the oxide sample occurs on a crystalline surface. Some parameter dispersion is also anticipated, as the nanoparticles in these samples do not have a uniform surface and are therefore expected to exhibit varied behavior. This should manifest as inconsistencies between harmonic fits, resulting in a harmonic dependence of some fitted parameters, a consequence of the model not capturing the frequency dependence of these parameters. This point is discussed further in Subchapter 6.4.2.

$$* + H_2O \rightleftharpoons H_2O^* \tag{6.C1}$$

$$H_2O^* \rightleftharpoons OH^* + H^+ + e^- \tag{6.E1}$$

$$OH^* \rightleftharpoons O^* + H^+ + e^- \tag{6.E2}$$

$$O^* + H_2O \rightleftharpoons OH_2O^* \tag{6.C2}$$

$$OH_2O^* \rightleftharpoons OOH^* + H^+ + e^- \tag{6.E3}$$

$$OOH^* \rightleftharpoons OO^* + H^+ + e^- \tag{6.E4}$$

$$OO^* \rightleftharpoons O_2 + * \tag{6.C3}$$

The C and E steps were converted into a set of ordinary differential equations (ODEs), which can be found in Appendix C.2, though it can also be easily programed with ElectroKitty [30], [31]. To fully describe the kinetic model, each electrochemical step requires a set of three constants, while chemical steps are described with a single constant describing one direction of a reaction. In addition, the total number of active sites is also required to solve these equations. Finally, equations describing the double-layer charging (C_{dl}) and the voltage drop due to uncompensated resistance (R_{u}), as well as the faradaic current were included in the model. To calculate these effects, we employed equations S8-S10, also found in Appendix C.2.

While the mechanistic steps are consistent with those in the above-mentioned studies, the mathematical formulation used here differs from that in previous work [158], [159]. Butler-Volmer formalism is used to describe the electrochemical reactions, and the Frumkin adsorption isotherm is adopted in place of the van der Waals isotherm reported in the cited articles. The Frumkin isotherm was selected as it provided the best fit to the peak at 1.01 V compared to all other isotherms tested, and also simplifies the numerical procedure, improving computational efficiency. The algorithm uses 26 constants to generate simulated data, which are determined by fitting the respective harmonic currents of each material. A full description of these constants is provided in Appendices C.2 and C.3, with a brief glossary given in Table 1.

Table 1: A quick glossary of the constants used to describe the mathematical model.

Constant	Description
α_1, α_2, α_3, α_4	Charge transfer coefficients, corresponding to the E1, E2, E3, and E4 steps
$E_{0,1}$; $E_{0,2}$; $E_{0,3}$; $E_{0,4}$	Formal potentials for the E1, E2, E3, and E4 steps
$k_{0,1}$; $k_{0,2}$; $k_{0,3}$; $k_{0,4}$	Rate constants for the electrochemical E1, E2, E3, and E4 steps
k_{ad1}, k_{ad2}	The forward and backward constant for the initial adsorption step (C1)
k_{c1}, k_{c2}	The forward and backward constant for the second chemical step (C2)
k_r	The rate constant describing the step of oxygen desorbtion (C3)
n_0	The total number of active sites
S^*, S_{H2O}, S_{OH}, S_O, S_{OH2O}, S_{OOH}, S_{OO}	Frumkin isotherm constant for each species
C_{dl}	Double layer capacitance

To solve the set of ODEs, an implicit discretization was used for the time step. The resulting set of algebraic equations was then calculated using the hybrid method found in the "root" routine of SciPy [164], where the parameters of the method are the default settings. This way, using the potential given by the potentiostat, the current for each time step could be calculated. The "curve_fit" routine included in Python's ScyPy module was used to fit each harmonic separately. The tolerance for the fit was set to 10^{-8}. The routine also provides information about the standard deviation of each parameter from which the confidence region can be estimated as discussed in reference [73]. A relative root mean squared error (RRMSE) comparison function between the simulated and experimental harmonic data was used to evaluate the "goodness of fit".

6.4 Results and Discussion

6.4.1 Characterization/comparison of materials

First, it is prudent to note the morphological properties of the studied materials. These being Ir Black, Ir on Vulcan and rutile IrO_2. All three materials are composed of nanoparticles, where Ir Black and Ir on Vulcan consist of mostly metallic Ir nanoparticles, with the difference that in Ir on Vulcan Ir nanoparticles are dispersed over a high surface area Vulcan carbon support. IrO_2 are oxide nanoparticles with a rutile structure prepared by annealing in a silica matrix, which was later removed by dissolution. Figure 6.1 shows TEM images as well as the particle size distribution obtained from the TEM images for each material. From the images, it can be seen that both Ir black and IrO_2 are agglomerated, while Ir on Vulcan shows a dispersion of smaller nanoparticles on the support but also contains some agglomerates. The average particle size for each material is 2.64 nm for Ir Black, 2.1 nm for Ir on Vulcan and 7.4 nm for IrO_2 nanoparticles.

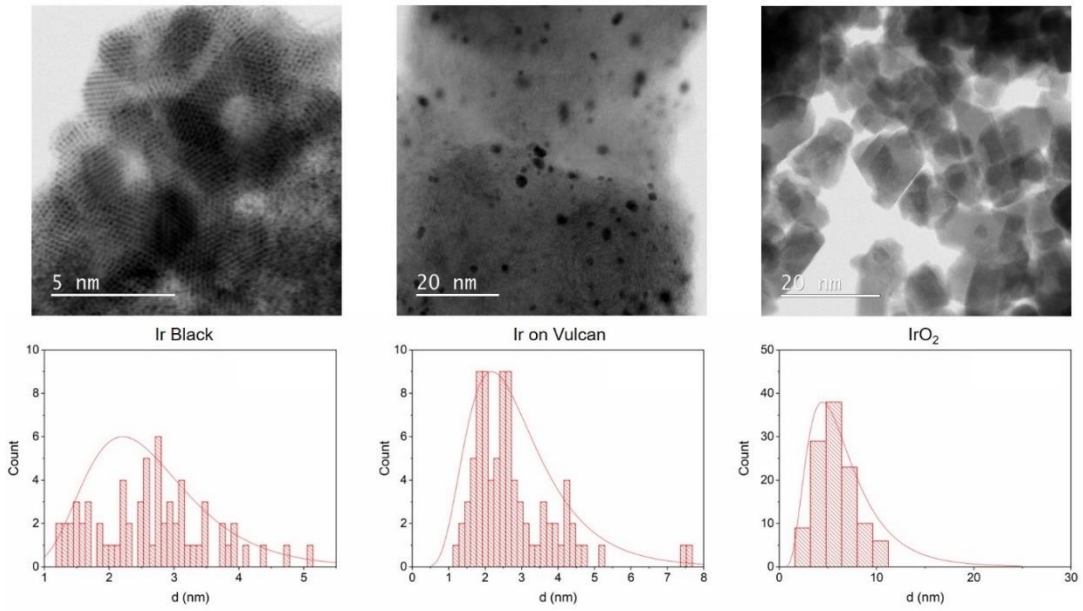


Figure 6.1: TEM images and particle size distributions for the studied materials. In order from left to right: Ir Black, Ir on Vulcan and IrO_2.Until now, fundamental studies have been performed mostly on bulk Ir metal electrodes [154], [155], [157], [165], [166], [167], while studies of the basic OER mechanism on nanosized Ir catalysts remain scarce. For bulk Ir metal, three surface oxidation steps are believed to occur prior to the onset of OER at approximately 1.4 V. As shown in Figure 6.2, the LSV curves for the Ir samples evolve with cycling, displaying peaks at approximately 0.6 V, 0.9 V, and 1.3 V, corresponding to reaction steps E1, E2, and E3, respectively. Growth of IrOH upon potential cycling between upper and lower potential limits has also been observed for bulk Ir [157], [166], suggesting that similar processes should occur for nanosized Ir.

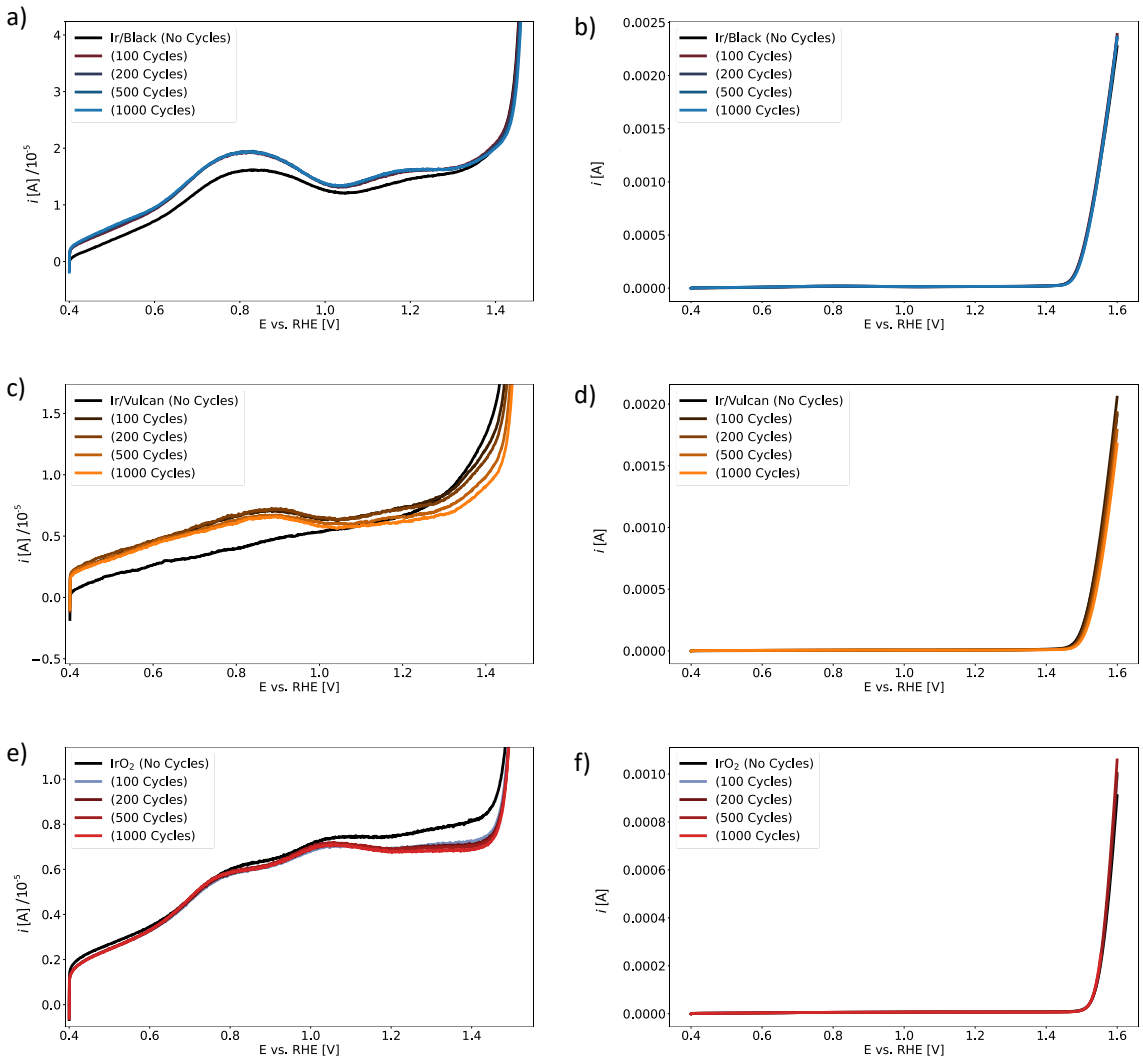


Figure 6.2: LSV comparison between the different Ir catalysts. From top to bottom: Ir Black, Ir on Vulcan and IrO_2. Figures 6.2 (a, c, e) show a close up of the region between 0.4 V and about 1.45 V in the Figures 6.2 (b, d, f). LSV scan from 0.4 V to 1.6 V was performed in 0.1 M $HClO_4$ for each material as deposited and after 100, 200, 500 and 1000 cycles. The materials were cycled by squared wave pulses, switching between 0.05 V and 1.45 V, with a potential hold of 2 s for each potential. All potentials are given with respect to the RHE reference electrode.

The LSV curves show that the material undergoes changes during cycling, referred to here as activation. For bulk Ir, this process is associated with the extensive growth of a 3D hydrous oxide (IrOH), as observed in numerous studies through both voltammetric characterization [154], [155], [157] and spectroscopic analysis of the catalyst surface [168], [169], [170]. The behavior of nanosized particles resembles that of bulk Ir but with some distinct differences. Even after activation, Ir on Vulcan exhibits poorly defined peaks in the potential range of 0.8–1.3 V, where Ir oxidation and reduction reactions would be expected (Figure 6.2c). While IrO_2 and Ir Black samples also show some peak broadening, their features are better resolved (Figures 6.2a and 6.2e, respectively). The peak potentials observed for the nanosized materials are also shifted to higher values compared to those reported for bulk Ir [154], [155], [157], [165], [171], [172]. Most striking is the peak at 1.01 V, which corresponds to a peak at 0.9 V in bulk Ir, and which appears considerably broader for nanosized Ir. These differences may be attributed to IrOH forming differently on Ir-based nanostructures, or to differences in the initial oxidation state of the material.

Looking at the general shape of LSVs in Figure 6.2, it appears that the underlying nature of reactions and mechanisms are the same regardless of whether the material is a supported Ir nanoparticle, bulk Ir, or even IrO_2. Nevertheless, some distinct differences should be further analyzed as they might affect the intrinsic properties of Ir OER. To better understand the similarities and differences between the materials, the ACV method is used to examine the different materials at different stages of activation. This method allows for easier study of Faradaic processes and tracking the changes of the materials through the activation or even degradation with cycling. Figure 6.3 illustrates how ACV can better show electrochemical reactions, compared to LSV/CV. This makes it easier to study how materials evolve based on their initial state.

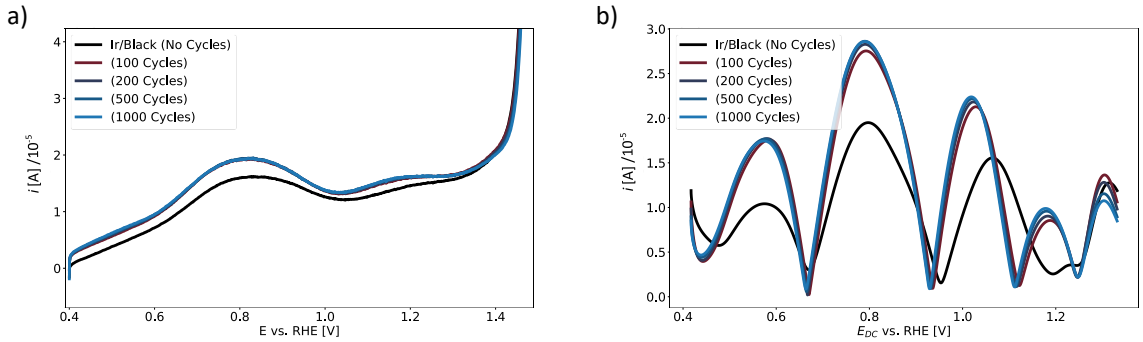


Figure 6.3: Comparison between LSV (a) and 3rd harmonic (b) for Ir Black. The advantage of ACV over LSV is clearly seen, as electrochemical reactions are seen in more detail. LSV and ACV measurements are taken before and after 100, 200, 500 and 1000 cycles of square wave pulses between 0.05 V and 1.45 V with a 2 s potential hold. The LSV was performed between 0.4 V and 1.6 V with a scan rate of 5 mV/s and the ACV scan made between 0.4 V and 1.5 V, with a scan rate of 1 mV/s, with a frequency and amplitude of 0.127 Hz and 150 mV respectively. All experiments are made in 0.1 M $HClO_4$ acid and all potentials are measured versus RHE.

6.4.2 ACV voltammograms/harmonics and their interpretation

Examining the ACV scans across different materials reveals that the material configuration, whether Ir is supported or unsupported, and the oxidation state of Ir, does indeed affect the activation process (Figure 6.4). As seen in Figures 6.4a, 6.4c, and 6.4e, some materials reach a steady state more rapidly than others.

In this Chapter, the focus is on the 3rd harmonic onward, as the lower harmonics have a noticeable contribution from ringing. This noise arises due to the numerical procedure used when filtering the harmonics in the frequency domain and we have been unable to avoid it for the 0th, 1st, and 2nd harmonics. The contribution from ringing becomes less noticeable for the higher harmonics, however, a noticeable contribution arises due to white noise in the 8th harmonic onward. As such, the 3rd and 4th harmonics are of primary concern as they have the cleanest data set. It should be stressed that all harmonics essentially share the same information.

Each material can be assigned its own activation threshold number (ATN). This number is given as the number of cycles needed for the harmonic currents to converge to a final shape that does not change with continued cycling, shown in Figures 6.4a, 6.4c and 6.4e. As the current amplitude increases or decreases, this indicates that we are observing the profile of a particular material, whose quantity (amount) is increasing or decreasing. Ir Black and Ir on Vulcan are the fastest to reach a steady-state, requiring only 100 cycles, which is consistent with previous observations where this was confirmed only with CV [173], [174]. Moreover, subsequent cycling only contributes to the decrease in current amplitude. IrO_2 is the slowest to fully activate, requiring 1000 cycles to reach the final steady state. Based on these trends, we can already see that Ir-based metallic analogues behave similarly, while rutile Ir oxide has a different behavior. The ATNs are summarized in Table 2. To further support this claim, a more thorough investigation of the OER pathway is needed.

Table 2: ATN for the materials studied. Square-wave pulses (SQW) between 0.05 and 1.45 V were used for the cycling protocol and each potential was held for 2 s. ACV measurements were performed after 100, 200, 500, and 1000 cycles.

Material	Activation threshold number
Ir Black	100
Ir on Vulcan	100
IrO_2	1000

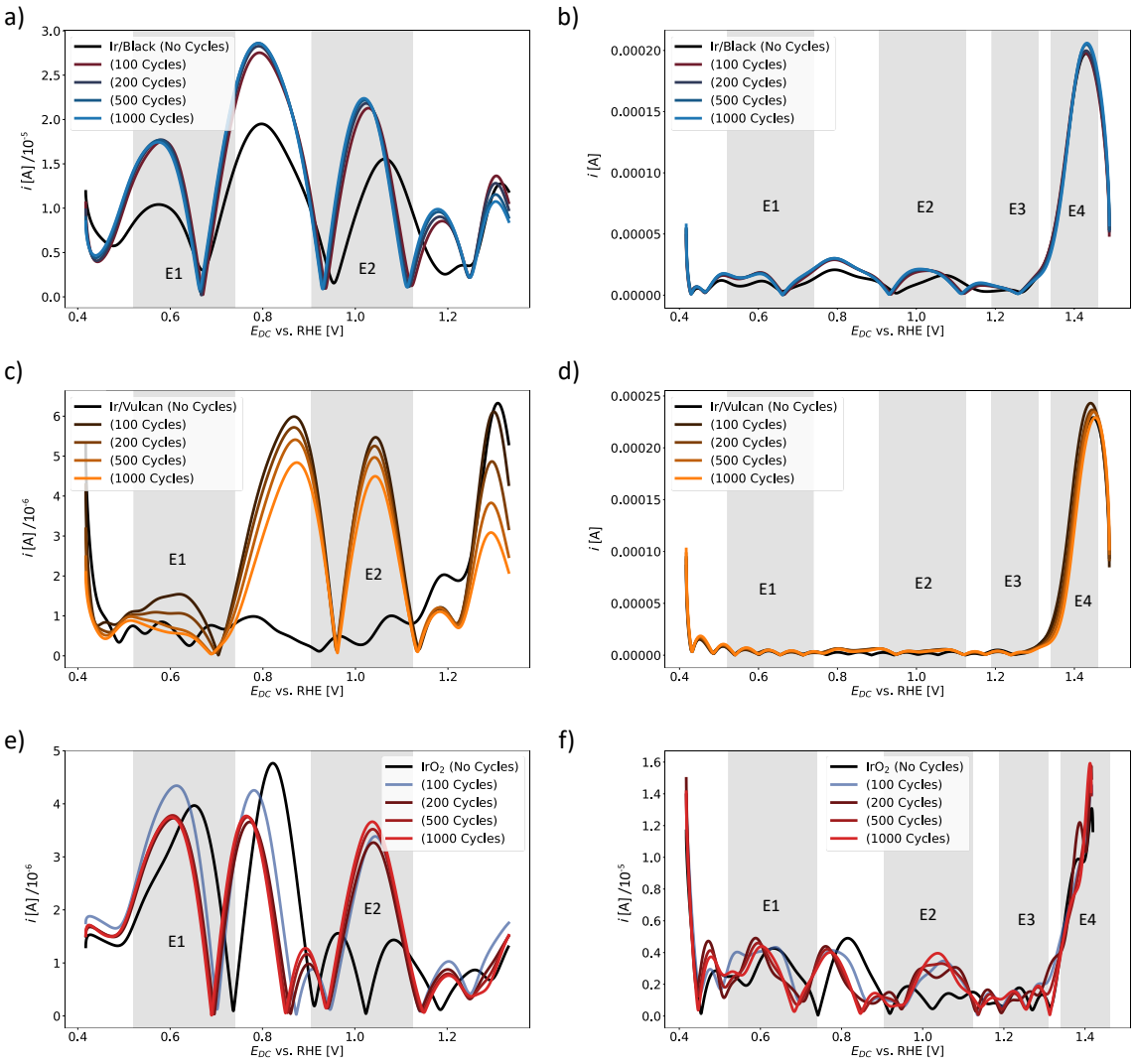


Figure 6.4: 3rd harmonic comparison for the studied materials. From top to bottom: Ir Black, Ir on Vulcan and IrO_2. Figures 6.4 (a, c, e) show a close up of the region between 0.4 V and 1.3 V of Figures 6.4 (b, d, f). In all Figures of 6.4, E1, E2, E3, and E4 note the electrochemical steps described previously in the text. The rest of the harmonics can be found in Supplementary Materials section 5. The ACV scans were made in 0.1 M $HClO_4$. The potential range was from 0.4 V and 1.5 V with a scan rate of 1 mV/s. The frequency was 0.127 Hz and the potential amplitude was 150 mV for the sinusoidal part of the signal. All potentials are with respect to the RHE.

Focusing exclusively on the shape and location of the third harmonic peak (Figure 6.4), and disregarding the current amplitude, several notable observations emerge. For potentials up to 1.3 V, both metallic Ir catalysts reach similar harmonic voltammogram shapes after the activation threshold number (ATN) of cycles, indicating a steady state (Figures 6.4a and 6.4c). The harmonic voltammogram for IrO_2 (Figures 6.4e and 6.4f) shows important similarities with the metallic Ir-based samples, most notably that upon reaching the ATN, the peak potentials for supported Ir and IrO_2 are virtually identical. This supports the hypothesis that all Ir-based materials share the same reaction pathway. However, Figure 6.4e also reveals that the peak shapes for IrO_2 differ considerably from those of the metallic Ir materials, suggesting that the IrO_2 surface has evolved differently. This point is further substantiated in Subchapter 6.5, where the mechanistic details are discussed. On this basis, it is concluded that all three materials follow the same mechanistic pathway, passing through the same intermediate stages.

While the general peak shape and position are virtually identical, some differences are apparent in the non-primary peaks of the odd harmonics, indicating that the reaction kinetics differ between materials. A full understanding of these kinetic differences requires a direct comparison between the model (described in Section 6.3) and the experimental data.

6.5 Discussion on OER Mechanism Fits

To further verify whether all materials share the same reaction pathway, the experimental data are fitted with the model presented in Subchapter 6.3, allowing differences and similarities among the materials to be directly identified. The fits were performed on the ACVs recorded after the ATN of cycles, taken to represent the steady state of each material. This yields the relevant kinetic parameters of the model, as well as the number of active sites for each material. A correct fit would be expected to produce a consistent set of parameters across frequencies, regardless of whether the response arises from the input signal or a harmonic current. However, some kinetic parameters may exhibit a frequency dependence, and this possibility cannot be excluded here. For this reason, each harmonic is fitted separately, both to further validate the model and to identify any frequency dependence in the fitted parameters.

Based on the data fit, it is seen that the proposed mechanism adequately reflects the obtained ACV data. The example below shows the fit to the 4^{th} harmonic for each material after ATN (100 cycles for Ir Black and Ir on Vulcan and 1000 cycles for IrO_2). The rest of the fitted constants can be found in Appendix C.5. The "goodness of fit" parameter for each harmonic shows that all fits are indeed adequate. Below, the confidence limits are treated in a quantitative manner and provide further insights into the adequacy of the model fit.

There is a consistency among the fits when observing the confidence limits for each parameter. It shows that the confidence limit for the formal potentials (E_0) and charge transfer coefficients (α) are very narrow, thus showing that the found parameters are likely correct. The confidence limits for the isotherm constants (denoted as g_x, with x as a stand-in for a species name) vary between the species, most of them have a narrow region, thus showing their importance to the model, with the constants for the active site (g^*), initially adsorbed water molecule (g_{H2O}), and finally, the final oxygen molecule (g_{OO}) having a wide confidence region. This could be the consequence of cross-correlation with kinetic parameters, as can be seen from the confidence regions for the kinetic parameters, as here the kinetic constants for the first and last electrochemical reactions ($k_{0,1}$ and $k_{0,4}$) have wide confidence regions. However, observing the confidence regions for the second and third kinetic constants ($k_{0,2}$ and $k_{0,3}$), the regions are relatively narrow, thus justifying the use of the isotherm at least for these two reactions. The kinetic parameters for the initial adsorption step ($k_{ad,1}$ and $k_{ad,2}$) again show a large confidence region, which again can be explained by the correlation with the isotherm term in the equation. The 6.C2 ($k_{c,1}$ and $k_{c,2}$) step has a much narrower confidence region, showing that the found parameters are likely correct, with the equilibrium being pushed in the forward direction in all cases. The parameter for the number of active sites (n_0) shows a narrow confidence region, along with the double layer capacitance (C_{dl}), however, some doubt can be given to the found double layer capacitance found in the higher harmonics (5^{th} onward), as the contribution from double layer charging is minimal. These results show that while some doubt can be given to some parameters from the individual harmonic fits, our confidence in the found harmonic fits is sufficient for us to accept the procedure on an individual basis. However, a problem with the current model is the inconsistency between the harmonic fits. In a perfect scenario, the correct model should exhibit consistency through all of the harmonic fits. This is discussed later on in the Chapter.

Having justified the quality of the fit, the constants in Table 3 can now be evaluated. Literature reports suggest a redox potential window for Ir from 0.8 V up to 1.3 V, where Ir undergoes a change in the oxidation state [154], [155], [175], [176]. This is in line with the formal potentials obtained for the reactions 6.E1, 6.E2, and 6.E3, which have values of 0.9 V, 1.1 V, and 1.3 V, respectively, for the metallic samples. Rutile IrO_2, however, shows a slight deviation, with formal potentials 0.83 V, 1.1 V, and 1.4 V, respectively, for the stated reactions. Due to the nature of cyclic voltammograms for Ir nanoparticles seldom showing well-resolved peaks, it is difficult to make good comparisons with the obtained formal potentials. However, for metallic samples, it can be seen with ACV (Figure 6.4), that the first redox step occurs at around 0.9 V, with the second following at roughly 1.1 V, which is in good agreement with the parameters in Table 3. The rest are harder to obtain, as the current starts to rise to a degree that there is little certainty in evaluating formal potentials from experimental data. For the oxide sample, it can also be seen that the first step occurs at lower potentials than that of metallics, which is also confirmed by the voltammograms found in the literature [154], [155], [158], [175], [176].

Turning first to the metallic samples (Ir Black and Ir on Vulcan), the k_0 constants obtained from the fit indicate that all four electrochemical steps are quite fast, confirming that kinetics is not the limiting factor in OER. The distorted peak shape is instead primarily attributable to the adsorption isotherm. The isotherm constants reveal that the first mechanistic step, water adsorption, is impeded by strong adsorbate interactions, as reflected in the high values of g^* and g_{H2O}. Elevated values are also observed for the adsorbed single oxygen atom (g_o) and the adsorbed oxygen molecule (g_{oo}).

The kinetics at IrO_2 show somewhat different behavior. Most surface species are not strongly hindered by adsorption; instead, the mechanism is slowed by inherently slower kinetics. This is evident when examining the constants responsible for adsorption kinetics and the chemical step between steps 6.E2 and 6.E3, as the constants $k_{0,2}$ and $k_{0,3}$ for IrO_2 are at least an order of magnitude smaller. It can also be seen that the $E_{0,3}$ value for the E3 step is higher than that of metallic Ir nanoparticles, making the reaction less favorable on IrO_2 than on IrOH grown from Ir metal [177]. This also shows that IrO_2 does not produce the same IrOH as Ir metal and that the material formed in a steady state is somewhat different, as the found constants would otherwise have similar values as metallic samples.

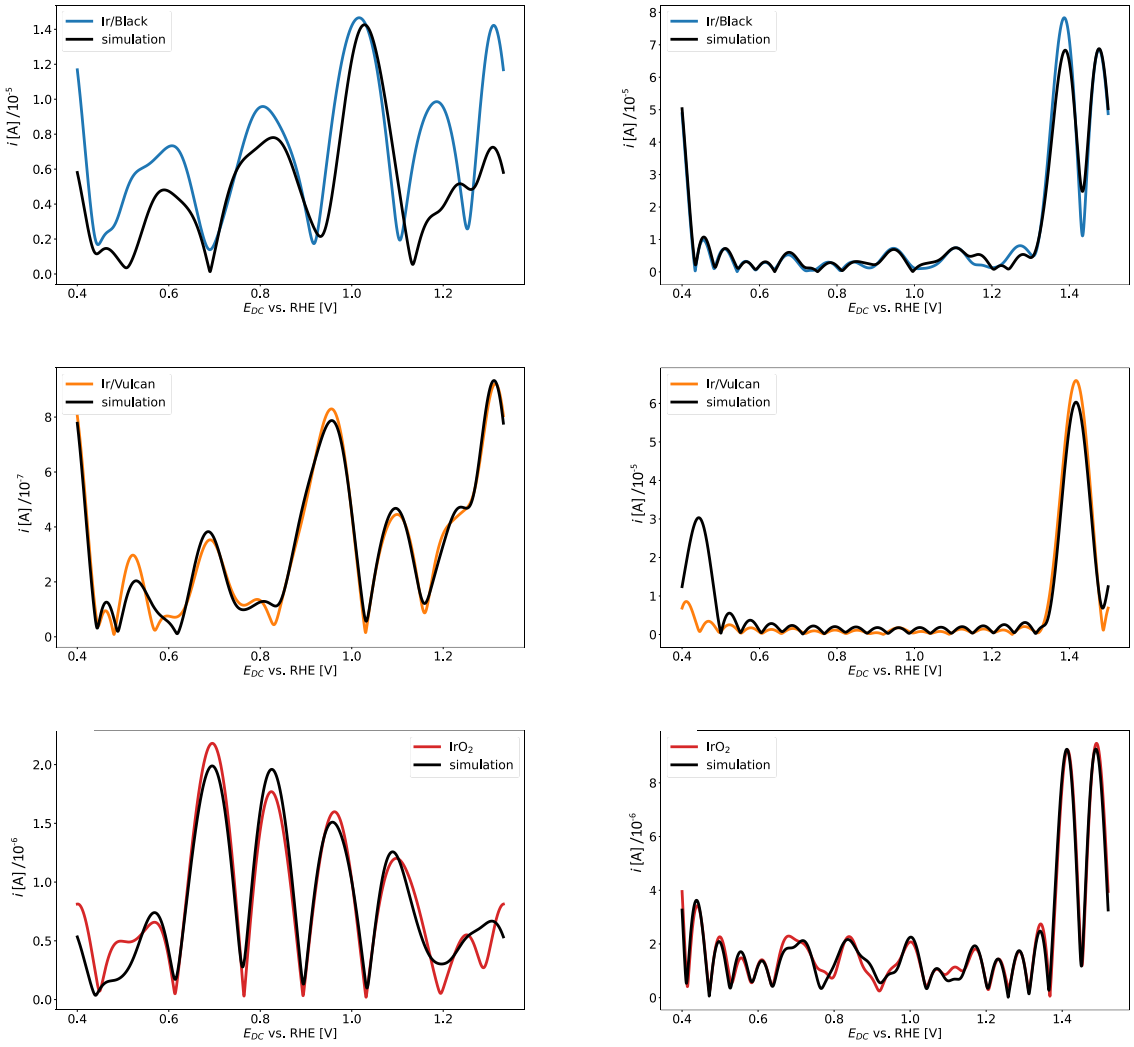


Figure 6.5: Comparison between simulation and experiment for the 4$^{\text{th}}$ harmonic currents after activation (100 cycles for Ir Black and Ir on Vulcan and 1000 cycles for IrO_2) for each studied material. From top to bottom: Ir Black, Ir on Vulcan and IrO_2. Figures 6.5 (a, c, e) show the region between 0.4 V and 1.3 V for the Figures 6.5 (b, d, f) in more detail. The experimental ACV was made with the linear ramp going from 0.4 V to 1.5 V with a scan rate of 1 mV/s, the sinusoidal signal has a frequency of 0.127 Hz and an amplitude of 150 mV. The measurement was made in 0.1 M $HClO_4$. All potentials are reported versus RHE.

Table 3: Fitted constants obtained from the 4th harmonic, with the standard deviation of the fit and the calculated RRMSE between the experiment and simulation. A glossary of the constants is available in Table 1.

Constant	Ir/Black	Confidence limit	Ir onVulcan	Confidence limit	IrO_2	Confidence limit
α_1 [/]	0.60	±0.014	0.85	±0.03	0.57	±0.01
E_{01} [V]	0.899	±0.001	0.911	±0.004	0.83	±0.0002
k_{01} [m/s]	12.0	±0.2	10.0	±1.5	3.69	±0.001
k_{ad1} [/s]	107	±3.0	64.7	±8.0	0.33	±0.01
k_{ad2} [/s]	26.3	±0.5	14.2	±1.7	15.6	±0.0001
α_2 [/]	0.426	±0.003	0.58	±0.01	0.47	±0.01
E_{02} [V]	1.160	±0.002	1.12	±0.01	1.11	±0.0004
k_{02} [m/s]	1.47	±0.06	1.08	±0.05	0.71	±0.01
α_3 [/]	0.37	±0.01	0.36	±0.01	0.35	±0.01
E_{03} [V]	1.330	±0.001	1.31	±0.01	1.41	±0.003
k_{03} [m/s]	1.41	±0.02	1.53	±0.09	0.35	±0.01
k_{c1} [/s]	157.0	±5.5	116.0	±12.8	0.006	±0.001
k_{c2} [/s]	15.2	±0.6	21.6	±2.3	0.001	±0.001
α_4 [/]	0.39	±0.03	0.61	±0.04	0.92	±0.01
E_{04} [V]	1.540	±0.006	1.49	±0.18	1.54	±0.08
k_{04} [m/s]	2080	±1020	0.25	±0.21	984	±4340
k_r [/s]	2.11	±0.41	9.01	±70.70	11.0	±9.5
S_* [/]	7.29	±0.16	10.3	±1.6	0.363	±0.001
S_{H2O} [/]	7.12	±0.12	9.42	±0.84	10.13	±0.001
S_{OH} [/]	2.52	±0.12	1.8	±0.1	0.244	±0.002
S_O [/]	0.789	±0.039	1.82	±0.10	1.16	±0.01
S_{OH2O} [/]	8.06	±0.53	15.6	±3.8	0.111	±0.002
S_{OOH} [/]	0.040	±0.001	0.009	±0.002	1.06	±0.01
S_{OO} [/]	20.1	±0.1	13.4	±2.6	1.75	±0.01
n_0 [/]	8.6E-10	±1.1E-11	1.0E-10	±3.5E-12	2.3E-10	±1.4E-12
C_{dl} [F]	5.0E-06	±3.0E-07	6.6E-06	±4.8E-07	3.3E-05	±1.1E-05
RRMSE [/]	0.122		0.103		0.131	

The mechanistic insight gained can now be used to make meaningful comparisons between materials. One of the fitted constants is the number of active sites, an important measure in any study of catalytic materials. This value allows both an estimate of the active site density based on catalyst mass, and a normalization of the polarization curves to assess which material has the highest activity per active site (Figures 6.6c and 6.6d). Such normalization offers a more reliable means of distinguishing between the intrinsic properties of different materials, as it removes the need to define an electrochemically active surface area.

The intrinsic activities thus measured are 1.7 mA $nmol^{-1}$ for Ir/Black, 5.1 mA $nmol^{-1}$ for Ir on Vulcan, and 0.9 mA $nmol^{-1}$ for IrO_2. These activities are taken at the OER onset potential of 1.55 V. As such, Ir on Vulcan is found to be roughly 5.6 times more active than IrO_2, and roughly 3 times more active than Ir/Black. However, a good catalyst should also have a sufficient number of active sites per mass, and the activity of the active sites of a catalyst should not be the only criterion by which we select the best catalyst. Thus, the best of the three catalysts studied would also be Ir on Vulcan, which has an active site density of 0.125 nmol μg^{-1}, and is also the most active. The other two materials have an active site density of 0.086 nmol μg^{-1} and 0.015 nmol μg^{-1} for Ir/Black and IrO_2, respectively.

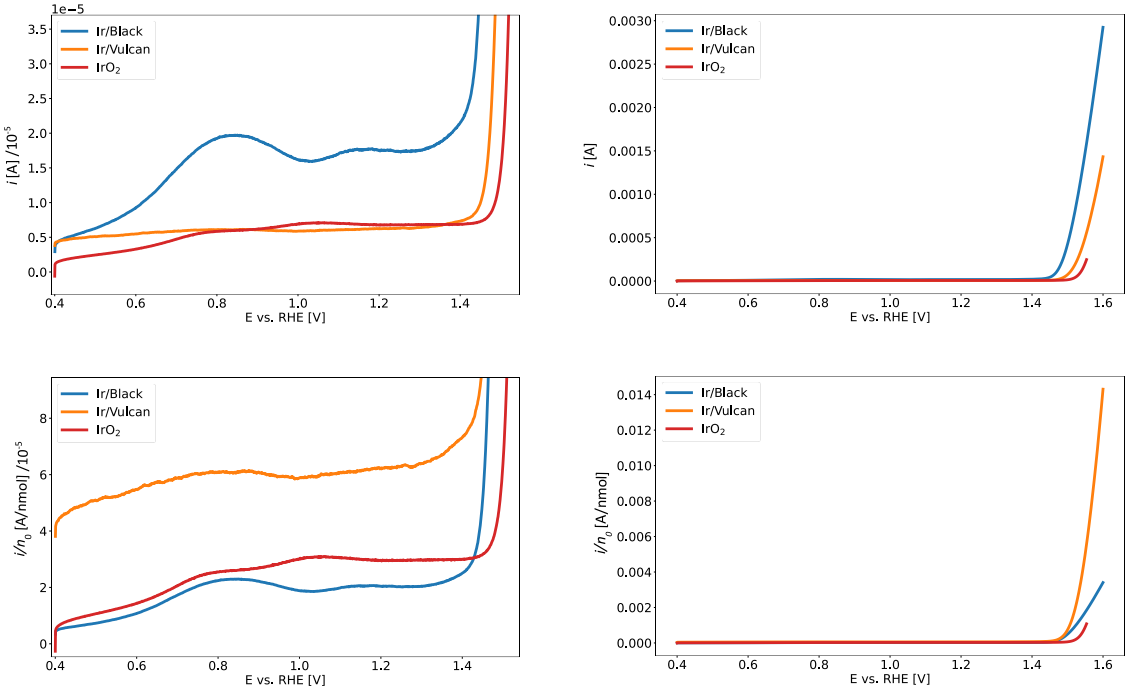


Figure 6.6: A comparison between materials. Figures 6.6a and 6.6b show the LSV curves without normalization, with 6.6a being the close-up of the region between 0.4 V and 1.45 V of Figure 6.6b. Figures 6.6c and 6.6d are the LSV curves normalized by the number of active sites, with Figure 6c again being the close-up of the region found in 6d. The LSVs for this image are taken when the material is at its most active (after 100 cycles for Ir Black and Ir on Vulcan, 1000 cycles for the IrO_2 sample). The LSV is taken between 0.4 V and 1.6 V, with a scan rate of 5 mV/s in 0.1 M $HClO_4$. Potentials are reported versus RHE.

As discussed earlier in the Chapter, one deficiency that has occurred is a lack of consistency in the fit of the harmonics. While the kinetic parameters remain roughly the same, the number of active sites found for the studied material varies greatly between harmonics. The reduction in the number of active sites due to the process is observed for all materials studied. This inconsistency is likely due to the dispersion of parameter values demonstrated for surface-bound reactions [178], [179]. This essentially suggests that different facets of the Ir nanoparticles studied behave differently under the same experimental conditions, such that the studied current is a combination of signals for each facet of the nanoparticles. Currently, this suggests that certain facets are more suited for OER as others. The model would need to be further optimized to fully capture parameter dispersion. For more information on parameter dispersion, see the article by Lloyd-Laney et al. [178], [179]. Other parameters also show some frequency dependence, such as the formal potential of the E1 step, being the other notable example. Again, showing the different frequency responses of different active sites.

These results demonstrate that materials sharing the same elemental composition are not necessarily the same catalysts. By fitting the ACV data, kinetic differences between all studied materials can be clearly identified. These differences are attributed to the local environment of the studied Ir-based nanoparticles, which influences both adsorption behavior and kinetics. This suggests that reactant access to the active site is of considerable importance in the development of novel electrocatalysts, and that careful attention should be paid to the design of both the support material and the catalytic particles. At present, these observations are based solely on the analysis of intrinsic activities and active site densities, and further research is needed to better understand the underlying phenomena.

6.6 Conclusion

This chapter demonstrates that ACV combined with mechanistic fitting can be used to screen the electrochemical intrinsic properties and OER mechanism of Ir-based materials. The approach reveals that Ir-metal-based materials evolve differently from IrO_2 upon activation cycling between oxidizing and reducing potentials, while also exposing both the differences and similarities in the mechanism across all materials studied. The OER reaction pathway appears to be impeded by adsorption on metallic Ir materials, whereas rutile IrO_2 exhibits kinetic limitations, yet both share the same underlying mechanistic pathway. This was established by fitting a model to the measured response and comparing the resulting constants. The fitted parameters were then used to identify the catalyst with the best intrinsic properties among the three materials studied, with a comparison of active site density and turnover frequency (TOF) allowing definitive conclusions to be drawn about which material is most suited for industrial application. A comparison between the metallic Ir samples thus shows that the supporting material, that influences nanoparticle morphology, can have an impact on OER activity. Comparing the metallic and oxide samples as well demonstrates that the presence of oxygen species within the nanoparticle structure also substantially affects catalytic activity.

The analysis becomes considerably more complex if one attempts to pinpoint the exact active site; as such, comparing TOFs and active site densities represents the only reasonable distinction that can be made. Identifying the active site beyond a generic Ir atom is not feasible for these materials, whose surfaces are far closer to those used industrially than those of single crystals. Rather than being flat and well-defined, these surfaces feature distributions of both facets and particle sizes, and are further altered by the activation process itself. Any inferences about the precise location and properties of active sites are therefore likely to be unreliable.

It should also be noted that while the fit yields kinetic and thermodynamic data, such data are only meaningful when compared against similar datasets. The changes observed in these parameters could arise from many different factors, including particle size, particle orientation, growth of a new phase, changes in the support material, and potentially others. This highlights a fundamental limitation of mean-field models: they struggle to explain observed differences between materials with an accurate microscopic picture.

Chapter 7

Conclusions

This thesis presented the most common and well-developed approach to modeling laboratory-scale electrochemical experiments. First, the equations describing the RDE electrode were introduced, along with the assumptions typically made about such systems. Following these assumptions, the equations were simplified and prepared for use in simulation. Chapter 3 introduced ElectroKitty, a library developed as part of this work and used throughout most of the thesis. The library was applied to three examples, related to the three hypotheses presented at the end of Chapter 1.

The first hypothesis states that solving such models is straightforward, and that simulation and fitting can be automated. This is confirmed by the ElectroKitty library presented in Chapter 3. While many nuances of simulation were not covered in this thesis, the core premise, that simulation and fitting can be automated, holds. The existence of ElectroKitty and similar packages confirm that simulation tasks can be made more accessible; however, this somewhat obscures an important caveat: different researchers have different needs and preferences. The notion of straightforward simulation can therefore only hold universally if researchers are working on sufficiently similar systems.

The second hypothesis, that simulation and fitting can yield meaningful mechanistic insight, is similarly confirmed. Fitting complex mechanisms, even if the validity of such models is questionable, can produce richer insights than just broad speculation on experimental data. As more experiments are conducted, many competing interpretations of the observed behavior emerge. While experiment is ultimately what rejects a model, it is important to have a precise and testable model to reject in the first place. In Chapters 4 through 6 I presented three different mechanisms, two of which were proposed by me, and another that was taken from literature. These mechanisms give a precise guess of the surface conditions, which can be either refuted or further corroborated. I have also shown, especially in Chapters 4 and 5 when the different proposed mechanisms were evaluated, just how important it is to have a diverse set of experiments to question model validity.

The final conclusion of this thesis is that the insights achievable from modelling depend heavily on the type of system studied. In this thesis I studied three very different types of systems, which while they all somewhat conform to the assumptions presented in Chapter 2, give vastly different mechanistic detail. For single-crystal surfaces, the active site can be assigned with considerable precision. This becomes harder as the surface becomes less homogeneous. While a mean-field model still produces good agreement between simulation and experiments, the conclusions can never be as precise as in the single-crystal case. When the system studied becomes composed of nanoparticles even less so. This is due to an inherent uncertainty of what the active site even looks like or where it is located. The parameters obtained from the fit become more convoluted, as the studied system increases in complexity. However, they still describe the behavior of an “average” active site.

This thesis concludes with a cautionary note. While mean-field models and simplifications can be powerful tools for interpreting experimental data, it is equally important to recognize their limitations early, both in terms of the model's assumptions and the physical meaning of the fitted parameters. While we gain insight by using such models, we are often left with more questions than answers.

Appendix A

Supplementary Materials for Chapter 4

A.1 ElectroKitty Code Containing the Model

Below is the code used for the simulation of the model presented in Chapter 4. Note that the isotherm contains lists for each step in the mechanism, that contain two lists, one for the forward and one for the backward reaction. All units are expressed in basic SI units as appropriate.

```
from electrokitty import ElectroKitty
import numpy as np
import matplotlib.pyplot as plt

mechanism = 'C:bb*=b* \n E(1): b* < c* \n E(1): c* = d* \n E(1):aa*=a* \n C:
a*=l* \n E(1): l* = m* \n C: final* = bb* + aa* \n E(1): bb* > c*'

kin = [[4.650896167832501e-06, 1.7169615809755034],

        [0.1124913477996893, 28.300374550126563, 0.9656289895553231],
        [0.3452633472873135, 671.3413866657255, 1.2628403059547946],
          [0.9801369222457272, 711.4748181227616, 0.9204357007198046],
            [1022.6867255951696, 732.7498749370912],
              [0.007952747041147535, 388.25781263721467, 0.6668011397245186],
                [0.3003130092953281, 99999998.32649107],
                [0.9564754303270201, 1034.3560676872987, 0.6486656620110904]]

D = []

iso = [[[12.151701284879932, 0, 0, 0, 0, 0, 0, 0, 0], [0, -18.489792653290888,
0, 0, 0, 0, 0, 0, 0]],
       [[0, 0, 0, 0, 0, 0, 0, 0, 0], [0, -21.623371648541536, 27.389295719700204,
0, 0, 0, 0, 0, 0]],
           [[0,  0,  -4.571582510728852,  0,  0,  0,  0,  0,  0], [0,  0,  0,  -
6.512789050824818, 0, 0, 0, 0, 0]],
          [[0,  0,  0,  0,  -10.719643156050694,  0,  0,  0,  0], [0,  0,  0,  0,  0,
8.430012815145133, 0, 0, 0]],
```

```
       [[0, 0, 0, 0, 0, 2.1901108590548013, 0, 0, 0], [0, 0, 0, 0, 0, 0,
0.8869454314068307, 0, 0]],
        [[0, 0, 0, 0, 0, 0, -13.645859523566704, 0, 0], [0, 0, 0, 0, 0, 0, 0,
1.067700850327604, 0]],
       [[0, 0, 0, 0, 0, 0, 0, 0, -19.976847966984497], [0.4351113311484233, 0,
0, 0, 2.1559376070550584, 0, 0, 0, 0]],
      [[-1.6172337036284494, 0, 0, 0, 0, 0, 0, 0, 0], [0, 0, 8.467585334284005,
0, 0, 0, 0, 0, 0]]]

species_info = [[0, 0, 0, 3.2850981467397947e-06, 0, 0, 0, 1.013794741355389e-
05, 0], []]

cell_const = [293, 12, 0.4, 0.125*10**-4]

spatial_info = [0.0001, 10, 10**-5, 0]

problem = ElectroKitty(mechanism)

problem.create_simulation(kin, cell_const, D, iso, spatial_info, species_info)

v = 0.05

problem.V_potential(0.4, 1.15, v, 0.0, 0, 4000)
e, i, t = problem.simulate()
problem.Plot_simulation()
```

A.2 STM Images of Pt(111) Before and After Going to 1.15 V

Ten potential scans were applied from 0.2 V up to 1.15 V, with a scan rate of 50 mVs^{-1}, while probing the surface with in situ STM. Below are the Figures of the surface before and after applying the scan. It is evident that no major reconstruction of the surface took place, thus justifying our assumption that the reactions taking place do not protrude deeper than the surface level and use of a mean-field model is not inherently wrong.

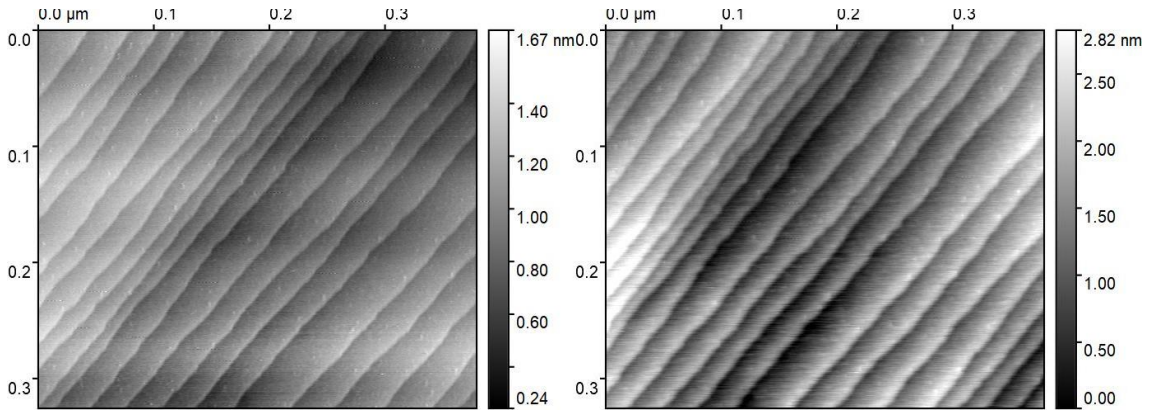


Figure A.1: In-situ STM images before (Left) and after (right) a scan up to 1.15 V.

A.3 Comparing Experiment and Simulation of Potential Holds

As the potentistat might does not necessarily hold the potential exactly at the mV range, it was investigated if perhaps the quantitative difference between simulation and experiment could be attributed to experimental error. For this, lower potentials are used for the simulation holds to see if potentially a closer quantitative agreement can be made. In no case is the potential lower than 10 mV from the assumed experimental potential hold. The behavior of the oxide peak during a hold is very sensitive to the applied potential, as such small variations could show a significant quantitative difference between experiment and simulation, even when the model is in principle correct. As can be seen the quantitative agreement is improved, as the potential is varied, showing that the differences could be due to potentiostat error.

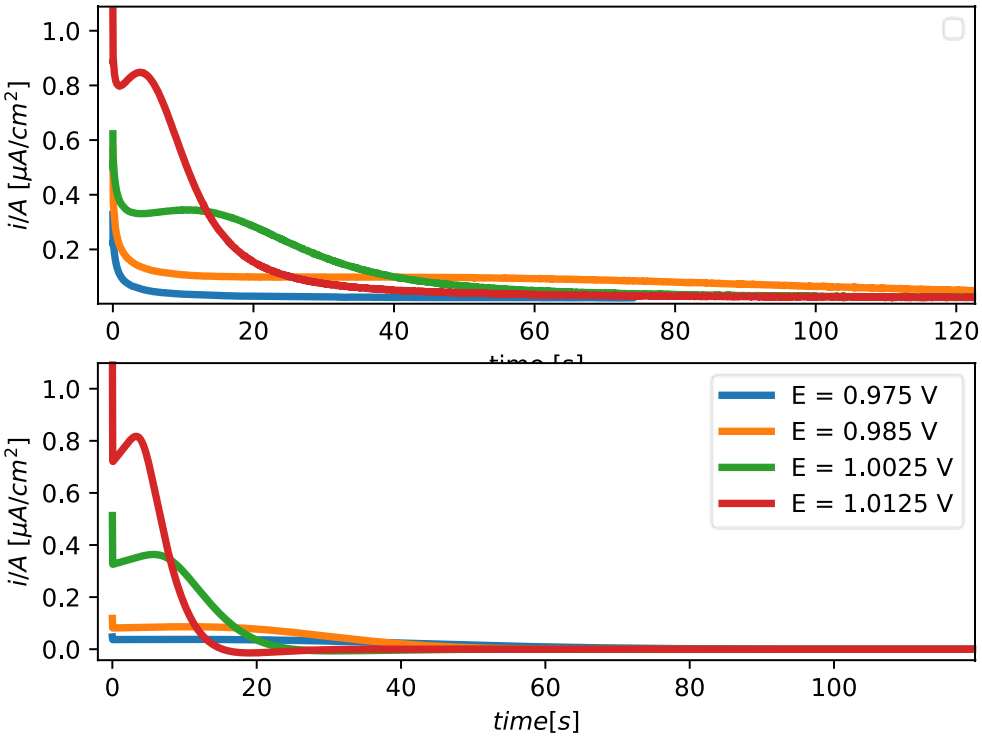


Figure A.2: Simulated potential holds with a variation in potential. Top: experimental results. Bottom: Simulated results with a positive shift of 2.5 mV in the positive direction.

A.4 Simulated Response From Literature

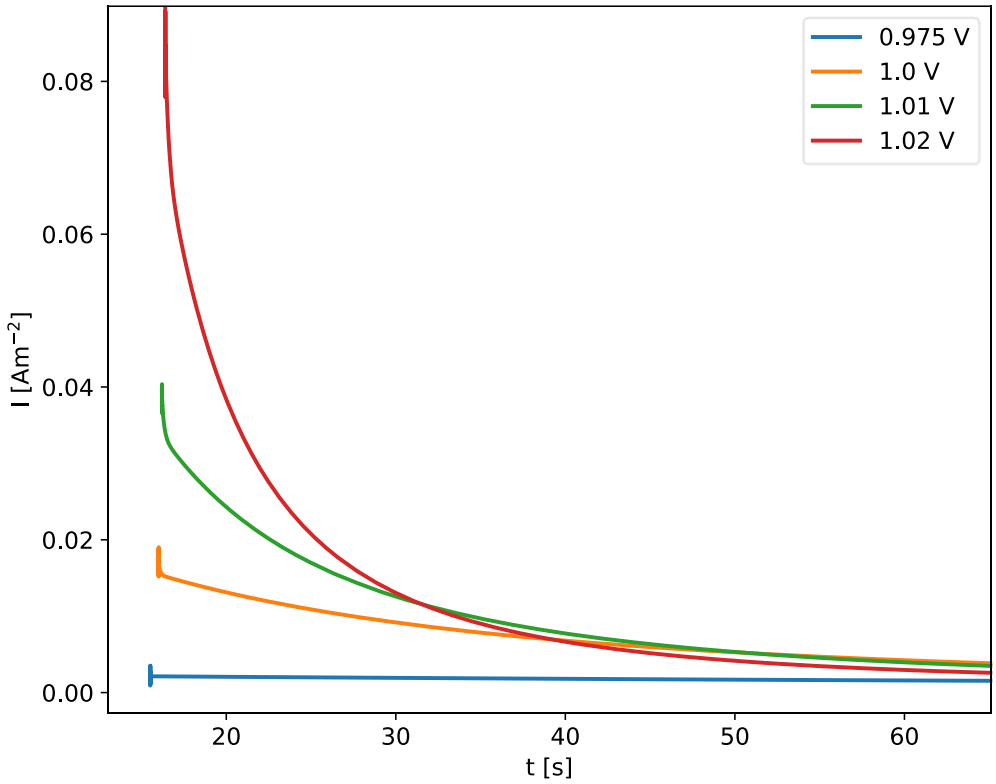


Figure A.3: Potential hold simulation using the literature model.

Appendix B

Supplementary Materials for Chapter 5

B.1 Demonstrating HER Subtraction From CVs

To obtain the pseudo-capacitances shown in the main paper, one needs to subtract the HER contribution to the measured current. This is done by assuming that the HER is essentially an exponential function superimposed onto the Ni oxidation current. Using the final tail in the data, and SciPy's [180], [181] curve_fit function to fit an exponential function onto it. The fitted function is used to subtract the function value from each experimental data point. As can be seen, there is a small shift to the rest of the data, as an exponential function is never zero; however, the effect is minimal.

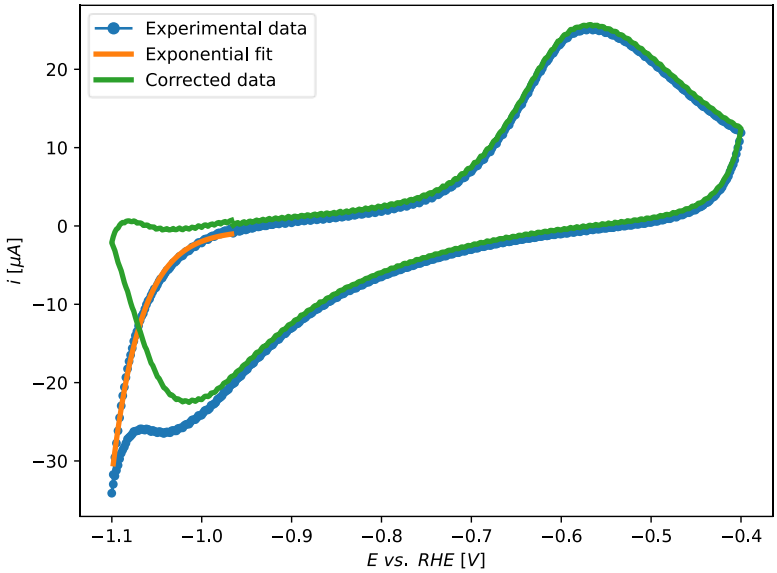


Figure B.1: Demonstrating on HER subtraction from voltamograms. The blue dotted curve is experimental data, with the orange being the fit made only on the points in that region. The fitted function is then subtracted from each data point. Note that an exponential function is essentially zero at higher potentials.

B.2 Figure Showing the Linear Dependance of the Anodic Peak

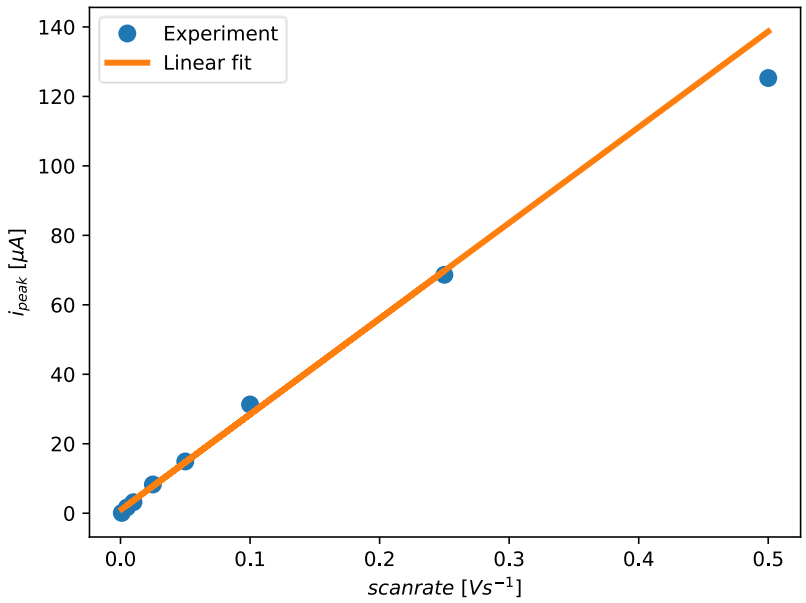


Figure B.2: Linear dependence of the Ni hydroxide peak.

B.3 Note on the Decreasing Anodic Current

The reason that the anodic current decreases as the vertex potential is increased is that some of the formed Ni (hydr)oxide is not fully reduced in the negative scan. This residual oxide then blocks the surface and does not allow the surface underneath to be available for oxidation. As one increases the vertex potential, more irreversible oxide forms, thus worsening the effect even further. This could be mitigated by annealing the electrode after each scan; however, the qualitative results and our conclusion would remain the same.

B.4 Figure of Simulated Potential Holds

To simulate this experiment, first the potential was scanned from a negative potential, with a scan-rate of 1 Vs^{-1}. Then the simulation was held at the final potential (0.255 V) for the anointed amount of time. Figure B.3 than shows the final step of the simulation, which is a slow scan of 10 mVs-1 in the negative direction. As can be seen the simulated results have a good qualitative agreement with experimental results in the main text (Figure 5.2c).

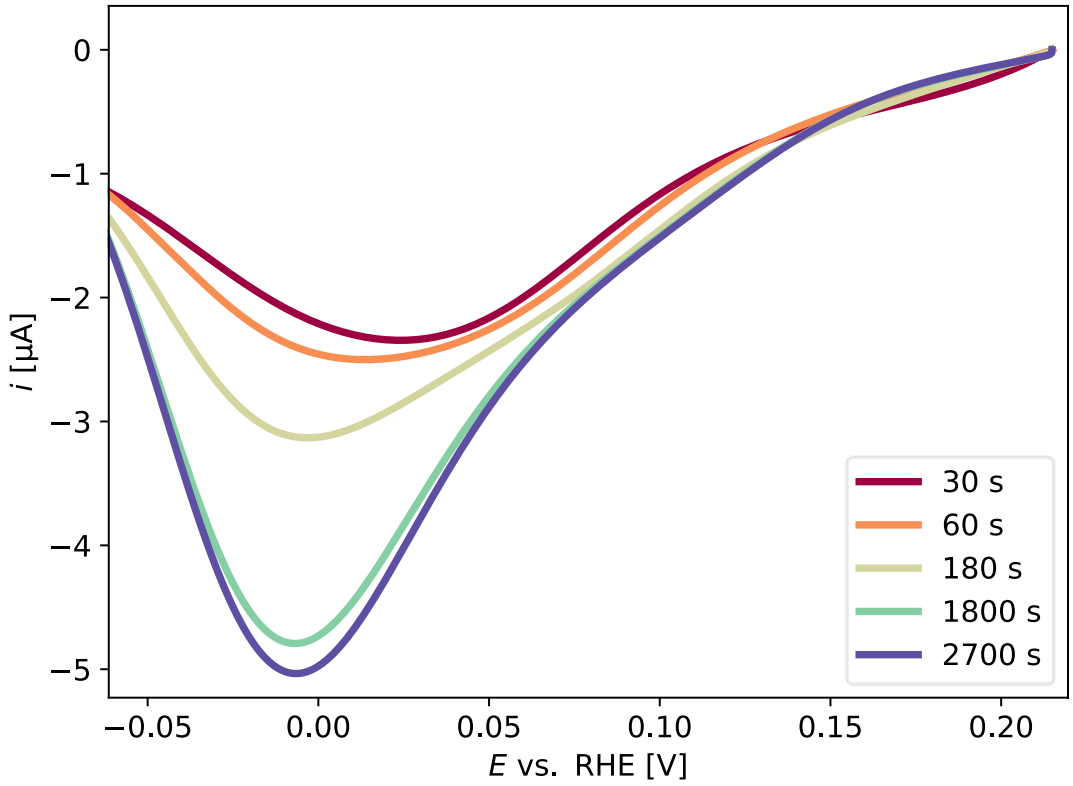


Figure B.3: Simulated potential hold experiment

B.5 Simulated Coverages of the Ni Place-Exchange Model

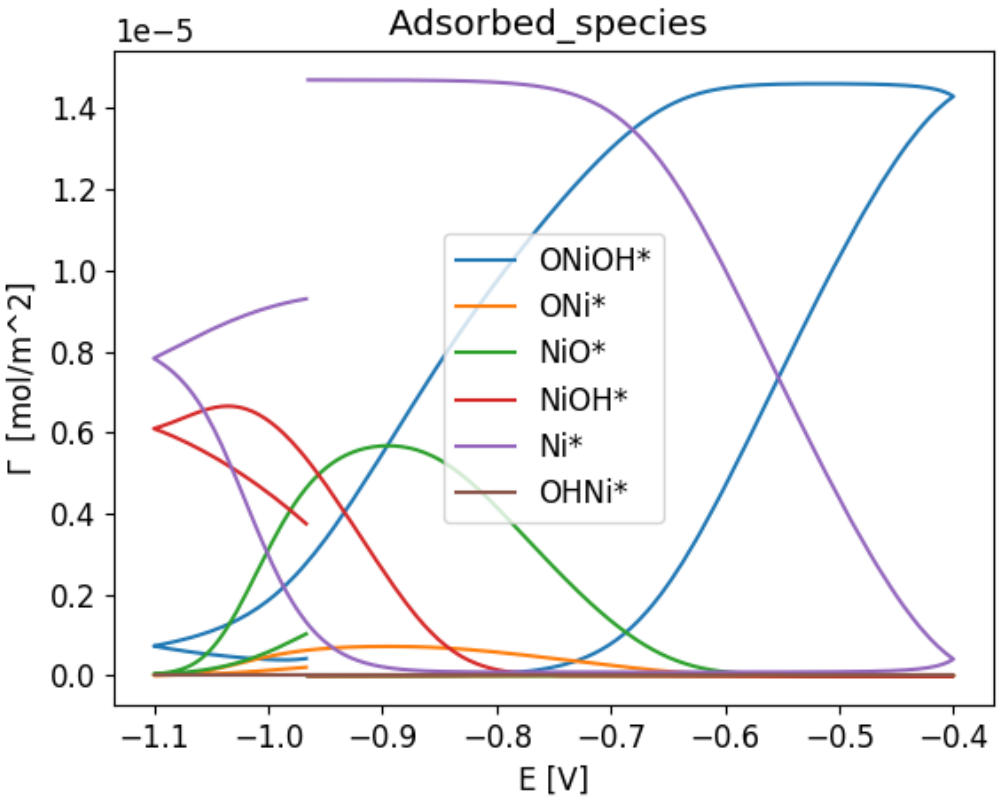


Figure B.4: Simulated coverages of the place exchange model in Chapter 5.

B.6 ElectroKitty Code for the Place-Exchange Model

```
"""
Created on Mon Nov 11 15:21:04 2025

@author: ozbejv
"""

import numpy as np
import matplotlib.pyplot as plt
from electrokitty import ElectroKitty

F=96485 #As/mol
R=8.314 #J/mol/K
T=293 #K

# Number of points in the spatial direction
nx=20
    # Number of points in the spatial direction
```

```
    # Mechanism string written in full
mechanism = 'E(1): ONiOH* = ONi* \n C: ONi* = NiO* \n E(1): NiO*=NiOH* \n
E(1): NiOH*=Ni* \n E(1):ONi* > OHNi* \n E(1): OHNi* > Ni*'

    kin_const=[[2.23599976839682e-09, 0.2270731466443743, -1.005127877172589],
               [8025.197462213034, 2130.550747859412],
               [0.37849438856509227, 0.569795295699977, -0.8876635772668164],
               [0.3037767435735477, 1.0845197586899118e-11, -
1.3428343416207846],
               [0.883152762097605, 768.0132190022811, -1.1634555030164773],
               [0.7002725180642281, 2.085368950788677, 11.051795884784271]]


    D=[]

    viscosity=10**-5 #m^2/s
    rot_freq=0 #Hz

    # Constants describing the cell: Temperature, Ru, Cdl, A
    cell_c=[293, 0, 1*10**-6, 0.286*10**-4] # K, NiOHhm , F/m^2, m^2

    # Constants describing the x direction: dx/xmax, nx
    si=[0.0001/36, nx, viscosity, rot_freq]

    spec_info = [[0, 0, 0, 0, 1.4700990255668218e-05, 0], []]

    iso = [-9.799536501684377, -29.99971787218451, -1.8951122568070744, -
9.501423828705727, -5.086902947447919, -29.924117329453818]

Ei=-1.1 #Initial potential, also the potential to wich the CV returns [V]
Ef=-0.4 #Final potential, we cycle to this potential [V]
v=0.05   #scan speed [V/s]
freq=0 #In case of ACV this is the frequency of a sine wave [Hz]
amp=0.0  #In case of ACV this is the amplitude of a sine wave [V]
nt=1000 #number of time points


###################
# simulation

problem=ElectroKitty(mechanism)

problem.V_potential(Ei, Ef, v, amp, freq, nt)
problem.create_simulation(kin_const, cell_c, D, iso, si, spec_info)

problem.simulate()
problem.Plot_simulation()
```

Appendix C

Supplementary Materials for Chapter 5

C.1 XRD Spectra and Sample Analysis

X-ray powder diffraction (XRD) measurements were performed using a PANalytical X'Pert PRO MPD high-resolution X-ray powder diffractometer with a Cu Kα1 radiation (λ = 1.5406 Å) in the 2θ range from 10° to 60° with the 0.034° step per 100 s (PANalytical B.V., Almelo, The Netherlands) with alpha1 configuration (CuKα1 λ = 1.5406 Å radiation). Phases were identified using the X'Pert HighScore Plus programme and the International Centre for Diffraction Data (ICDD) PDF-4+ 2021 database [182].

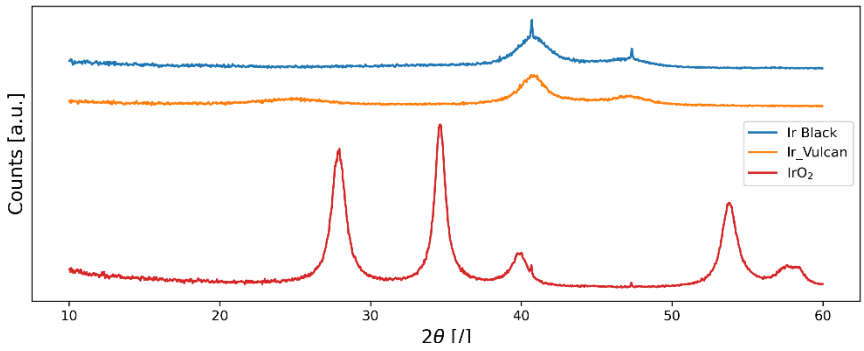


Figure C.1: XRD spectra of Ir Black, Ir on Vulcan and IrO_2 nanoparticles.

In-house synthesized IrO_2 nanoparticles, commercial Ir Black, and Ir on Vulcan were first analyzed by XRD. For the commercial samples, the broader peaks were observed at 40.7° (111) and 47.3° (200) angles corresponding to cubic Ir (PDF 04-007-8342) [182]. The shape of the Ir Black peaks indicates that the sample as a whole consists of small Ir nanoparticles (broad base) with some larger particles (sharp peak). An additional broad peak in the pattern of the Ir Vulcan sample around 25° corresponds to the (002) diffraction of typical amorphous carbon (graphite-like crystalline structure, PDF 00-001-0640) [182]. In the sample of IrO_2 nanoparticles, however, the diffraction peaks at 28.0°, 34.5°, 39.8°, 53.8°, 57.9°, and 58.2° angles, corresponding to planes (110), (101), (200), (211), (220), and (002), are related to tetragonal IrO_2 (PDF 04-009-8479) [182]. The presence of small peaks at 40.7° and 47.3° indicates a small amount of metallic Ir in the sample.

C.2 Model Equations

Here, the ODEs used for modeling our data are presented. The equations were discretized with respect to time and solved implicitly using a root finding algorithm (root) found in Python's SciPy Optimize module. A short discussion on the constants used in ODEs can be found in the following section.

$$\frac{d\theta_*}{dt} = -k_{\mathrm{ad1}}\theta_* e^{S_*\theta_*} + k_{\mathrm{ad2}}\theta_{\mathrm{H_2O}} e^{S_{\mathrm{H_2O}}\theta_{\mathrm{H_2O}}} + k_{\mathrm{r}}\theta_{\mathrm{H_2O}} e^{S_{\mathrm{OO}}\theta_{\mathrm{OO}}} \tag{C1}$$

$$\frac{d\theta_{\mathrm{H_2O}}}{dt} = k_{\mathrm{ad1}}\theta_* e^{S_*\theta_*} - k_{\mathrm{ad2}}\theta_{\mathrm{H_2O}} e^{S_{\mathrm{H_2O}}\theta_{\mathrm{H_2O}}} + k_{0,1}\left(\theta_{\mathrm{OH}} a_{\mathrm{H}} e^{S_{\mathrm{OH}}\theta_{\mathrm{OH}}} e^{-\alpha f(E-E_{0,1})} - \theta_{\mathrm{H_2O}} e^{S_{\mathrm{H_2O}}\theta_{\mathrm{H_2O}}} e^{-\alpha f(E-E_{0,1})}\right) \tag{C2}$$

$$\frac{d\theta_{\mathrm{OH}}}{dt} = -k_{0,1}\left(\theta_{\mathrm{OH}} a_{\mathrm{H}} e^{S_{\mathrm{OH}}\theta_{\mathrm{OH}}} e^{-\alpha f(E-E_{0,1})} - \theta_{\mathrm{H_2O}} e^{S_{\mathrm{H_2O}}\theta_{\mathrm{H_2O}}} e^{-\alpha f(E-E_{0,1})}\right) + k_{0,2}\left(\theta_{\mathrm{O}} a_{\mathrm{H}} e^{S_{\mathrm{O}}\theta_{\mathrm{O}}} e^{-\alpha f(E-E_{0,2})} - \theta_{\mathrm{OH}} e^{S_{\mathrm{OH}}\theta_{\mathrm{OH}}} e^{-\alpha f(E-E_{0,2})}\right) \tag{C3}$$

$$\frac{d\theta_{\mathrm{O}}}{dt} - k_{0,2}\left(\theta_{\mathrm{O}} a_{\mathrm{H}} e^{S_{\mathrm{O}}\theta_{\mathrm{O}}} e^{-\alpha f(E-E_{0,2})} - \theta_{\mathrm{OH}} e^{S_{\mathrm{OH}}\theta_{\mathrm{OH}}} e^{-\alpha f(E-E_{0,2})}\right) - k_{\mathrm{c1}}\theta_{\mathrm{O}} e^{S_{\mathrm{O}}\theta_{\mathrm{O}}} + k_{\mathrm{c2}}\theta_{\mathrm{OH_2O}} e^{S_{\mathrm{OH_2O}}\theta_{\mathrm{OH_2O}}} \tag{C4}$$

$$\frac{d\theta_{\mathrm{OH_2O}}}{dt} = k_{\mathrm{c1}}\theta_{\mathrm{O}} e^{S_{\mathrm{O}}\theta_{\mathrm{O}}} - k_{\mathrm{c2}}\theta_{\mathrm{OH_2O}} e^{S_{\mathrm{OH_2O}}\theta_{\mathrm{OH_2O}}} + k_{0,3}\left(\theta_{\mathrm{OOH}} a_{\mathrm{H}} e^{S_{\mathrm{OOH}}\theta_{\mathrm{OOH}}} e^{-\alpha f(E-E_{0,3})} - \theta_{\mathrm{OH_2O}} e^{S_{\mathrm{OH_2O}}\theta_{\mathrm{OH_2O}}} e^{-\alpha f(E-E_{0,3})}\right) \tag{C5}$$

$$\frac{d\theta_{\mathrm{OOH}}}{dt} = -k_{0,3}\left(\theta_{\mathrm{OOH}} a_{\mathrm{H}} e^{S_{\mathrm{OOH}}\theta_{\mathrm{OOH}}} e^{-\alpha f(E-E_{0,3})} - \theta_{\mathrm{OH_2O}} e^{S_{\mathrm{OH_2O}}\theta_{\mathrm{OH_2O}}} e^{-\alpha f(E-E_{0,3})}\right) + k_{0,4}\left(\theta_{\mathrm{OO}} a_{\mathrm{H}} e^{S_{\mathrm{OO}}\theta_{\mathrm{OO}}} e^{-\alpha f(E-E_{0,4})} - \theta_{\mathrm{OOH}} e^{S_{\mathrm{OOH}}\theta_{\mathrm{OOH}}} e^{-\alpha f(E-E_{0,4})}\right) \tag{C6}$$

$$\frac{d\theta_{\mathrm{OO}}}{dt} = -k_{0,4}\left(\theta_{\mathrm{OO}} a_{\mathrm{H}} e^{S_{\mathrm{OO}}\theta_{\mathrm{OO}}} e^{-\alpha f(E-E_{0,4})} - \theta_{\mathrm{OOH}} e^{S_{\mathrm{OOH}}\theta_{\mathrm{OOH}}} e^{-\alpha f(E-E_{0,4})}\right) - k_{\mathrm{r}}\theta_{\mathrm{H_2O}} e^{S_{\mathrm{OO}}\theta_{\mathrm{OO}}} \tag{C7}$$

To calculate the double layer charging and the voltage drop due to uncompensated resistance, we must write the equations describing such processes. These are equations C8 and C9 respectively, where t denotes time, E_{signal} is the potential of the potentiostat, i_{c} the capacitive current and i_{f} the faradaic current. The subscript p represents the value from the previous time step. To calculate the faradaic current we employ equation C10. The constants are further expanded upon in the following section.

$$i_{\mathrm{c}} = -C_{\mathrm{dl}}\frac{dE_{\mathrm{signal}}}{dt} + R_{\mathrm{u}}C_{\mathrm{dl}}\left(\frac{i_{\mathrm{f}} - i_{\mathrm{f},p}}{\Delta t} + \frac{i_{\mathrm{c}} - i_{\mathrm{c},p}}{\Delta t}\right) \tag{C8}$$

$$E = E_{\mathrm{signal}} - R_{\mathrm{u}}(i_{\mathrm{f}} + i_{\mathrm{c}}) \tag{C9}$$

$$i_{\mathrm{f}} = -n_0 F \begin{pmatrix} k_{0,1}(\theta_{\mathrm{OH}} a_{\mathrm{H}} e^{s_{\mathrm{OH}}\theta_{\mathrm{OH}}} e^{-\alpha f(E-E_{0,1})} - \theta_{\mathrm{H_2O}} e^{s_{\mathrm{H_2O}}\theta_{\mathrm{H_2O}}} e^{-\alpha f(E-E_{0,1})}) + \\ k_{0,2}(\theta_{\mathrm{O}} a_{\mathrm{H}} e^{s_{\mathrm{O}}\theta_{\mathrm{O}}} e^{-\alpha f(E-E_{0,2})} - \theta_{\mathrm{OH}} e^{s_{\mathrm{OH}}\theta_{\mathrm{OH}}} e^{-\alpha f(E-E_{0,2})}) + \\ k_{0,3}(\theta_{\mathrm{OOH}} a_{\mathrm{H}} e^{s_{\mathrm{OOH}}\theta_{\mathrm{OOH}}} e^{-\alpha f(E-E_{0,3})} - \theta_{\mathrm{OH_2O}} e^{s_{\mathrm{OH_2O}}\theta_{\mathrm{OH_2O}}} e^{-\alpha f(E-E_{0,3})}) + \\ k_{0,4}(\theta_{\mathrm{OO}} a_{\mathrm{H}} e^{s_{\mathrm{OO}}\theta_{\mathrm{OO}}} e^{-\alpha f(E-E_{0,4})} - \theta_{\mathrm{OOH}} e^{s_{\mathrm{OOH}}\theta_{\mathrm{OOH}}} e^{-\alpha f(E-E_{0,4})}) \end{pmatrix} \tag{C10}$$

C.3 Constants Used

To fully describe an electrochemical reaction using the Butler-Volmer formalism, we need a total of three constants for each E step. These are the reaction constant denoted as $k_{0,i}$, Formal potential $E_{0,i}$ and charge transfer coefficient α_i. Here "i" is used to denote one of the four electrochemical steps found in the reaction pathway. Furthermore, to describe the chemical steps, a set of two constants is needed to describe such a step. Here $k_{ads,i}$ and $k_{c,i}$ are denoted as constants for the initial adsorption and latter chemical transition steps respectively, with 1 denoting a forward and 2 a backward step. The final step of oxygen desorbing is described with a single constant k_r. Two thermodynamic constants used as well are ah, representing the proton activity found in the solution and f as the standard electrochemical constant, comprised from the Faraday's and gas constants, as well as temperature. This constant has a value of around 38 at room temperature. As explained in Chapter 6, we also simulate the uncompensated resistance and double layer capacitance, the constants being R_u and C_{dl} respectively. We also use θ_j to describe the relative number of active sites used by the individual species, with n_0 being the total number of active sites on the studied material. Finally, each species has a constant to describe its Temkin isotherm, the symbol being S_j. Both in the case of θ_j and S_j, j denotes one of the species: *, H2O, OH, O, OH2O, OOH, and OO.

Finally to make a fit, the constants to be varied during the procedure are all of the $k_{0,i}$, $E_{0,i}$ and α_i,, all four constant for the adsorption and chemical steps, the total number of active sites and double layer capacitance, as well as all seven isotherm constants. As such there are in total 26 constants that need to be fitted onto experimental data. The uncompensated resistance used in the model is set to the value obtained by high-frequency EIS (Spectra are shown below). The value is typically around 20 Ω.

C.4 EIS Spectra

Here the high frequency EIS spectra obtained for the materials studied are shown. It can be observed that all of the materials have a similar value of uncompensated resistance of about 20 Ω. The measurement was performed with the SP-300 potentiostat before each experimental procedure, as described in the main text.

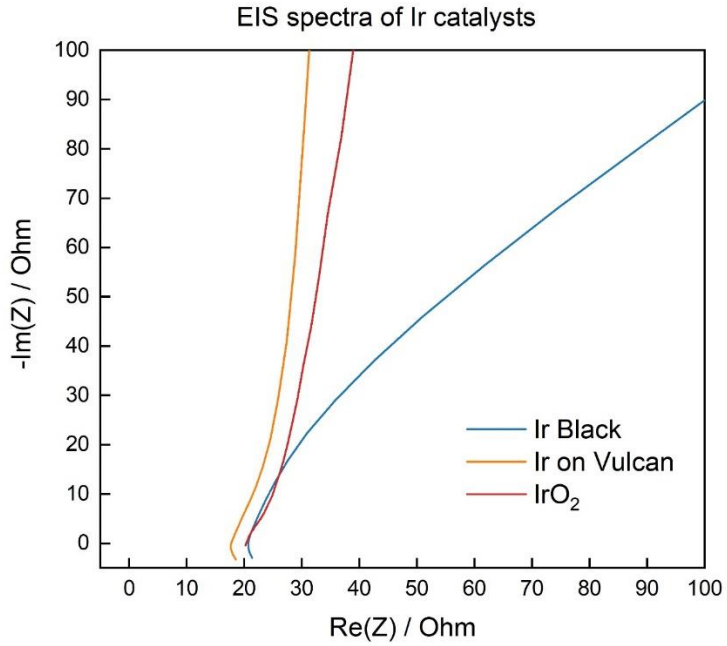


Figure C.2: High frequency EIS spectra for the investigated samples.

C.5 Found Constants for Each Material

Here are shown all of the found constants for each material. The fits were made for each of the harmonics separately, starting with the 3rd harmonic. The constant in two regions are also fitted. The lower region up to about 1.2 V and high region up to 1.55 V. This was done as in the high region the reactions occurring in the lower region do not have an adecuate response and the fitted constants may lose physical meaning. This can be seen as the constants for the different regions sometimes differ greatly. The procedure is then done by first fitting the lower region and then fitting the high region with the found constants and combining the constants to gain a better picture of our mechanism.

Ir Black Low region											
Constant	3rd harmonic fit	4th harmonic fit	5th harmonic fit	6th harmonic fit	7th harmonic fit		3rd harmonic error	4th harmonic error	5th harmonic error	6th harmonic error	7th harmonic error
k01 [/s]	2026.56	2141.76	1958.17	1590.78	1860		86.8104	29.1009	0.000140105	4.88211	72.9629
E01 [V]	1.48934	1.5215	1.51388	1.68671	1.54384		0.00265391	0.000796912	0.000655134	0.0033326	0.0867033
Kr [/s]	0.241371	0.263064	0.955005	0.196109	0.997937		0.027266	0.00908912	0.000759593	0.000238314	0.0276249
k02 [/s]	3.18199	1.40507	0.746316	1.32093	0.777779		0.146142	0.00432936	0.00305052	0.00596692	0.039806
E02 [V]	1.34898	1.32629	1.37618	1.40712	1.37894		0.000510646	0.000261368	0.000403399	1.91E-05	0.0359505
k03 [/s]	2.20186	1.46604	0.305232	0.938696	0.343533		0.0643109	0.0101653	0.000641609	0.00367267	0.00374243
E03 [V]	1.13874	1.1644	1.11145	1.24963	1.12729		0.00104589	0.000278662	0.000122289	0.00071541	0.00221783
k04 [/s]	11.5486	11.9639	8.15E+00	17.7803	6.29504		0.503519	0.0385574	0.0125287	0.000876383	0.0801394
E04 [V]	0.872272	0.898981	0.945792	0.942652	0.988655		0.00134113	0.00015205	0.000163972	7.25E-05	0.00202338
kc1 [/s]	1.00E+02	1.57E+02	25.9046	170.536	18.9681		4.71E+00	1.02012	0.023066	0.000298401	0.381413
kc2 [/s]	1.74E+01	1.52E+01	2.13E+01	9.89E+00	2.28E+01		4.45E-01	0.102609	0.0128316	2.65E-04	9.05E-01
kad1 [/s]	142.36	106.605	145.342	39.027	161.168		4.43015	0.61381	0.00165931	0.00112628	1.11101
kad2 [/s]	24.467	26.3489	66.6905	34.7024	74.5406		1.34635	0.0863816	0.00568126	0.110211	1.54407
n0 [/]	8.24E-10	8.59E-10	7.90E-10	6.75E-10	6.35E-10		9.22E-12	1.96E-12	2.85E-12	9.39E-15	1.16E-11
Cdl [F]	4.74E-06	4.98E-06	6.61E-04	4.40E-06	3.15E-06		2.11E-07	5.50E-08	9.60E-05	8.95E-09	1.65E-07
Sa [/]	12.7455	7.11809	6.68919	8.05318	5.819		0.88276	0.0218956	0.0121153	5.75E-05	0.0697697
Sb [/]	1.67234	2.52036	1.99623	2.2943	1.99959		0.0324007	0.0203153	0.00432717	0.00384517	0.0127776
Sc [/]	4.03E-01	7.89E-01	4.56E-01	1.49E+00	0.488014		1.29E-02	0.00732538	0.00157178	4.02E-06	0.00443954
Sd [/]	9.18521	8.05778	15.5057	1.84672	15.7781		0.531438	0.0988839	0.00662879	0.0021831	0.17779
Se [/]	0.0325686	0.0403924	0.107037	0.0352745	7.82E-02		0.00114138	0.000162513	0.00130293	0.000209309	1.79E-03
Sf [/]	17.434	20.1309	30.8661	14.1308	32.8557		0.784099	0.166832	0.00758313	0.0428817	0.23722
Sn [/]	5.79352	7.29341	8.44468	12.44	9.59017		0.165545	0.0292263	0.0108504	0.0391775	0.0934634
alfa1 [/]	0.37673	0.39093	0.967285	1.27427	1.17821		0.0420609	0.00557385	0.00166364	0.0047792	0.0265056
alfa2 [/]	0.342716	0.370456	0.109851	0.220255	0.0872356		0.00625891	0.00193742	0.00300663	0.000422289	0.000674338
alfa3 [/]	0.401286	0.425853	0.496635	0.545202	0.495757		0.00106836	0.000512662	0.000204135	1.61E-05	0.00151497
alfa4 [/]	0.610133	0.598741	0.168772	0.242018	0.146912		0.0209939	0.00260276	0.000691508	0.000406447	0.00254589
Phi	0.194337973	0.121782531	0.208689642	0.434551103	0.696298781						

Ir Black High Region											
Constant	3rd harmonic fit	4th harmonic fit	5th harmonic fit	6th harmonic fit	7th harmonic fit		3rd harmonic error	4th harmonic error	5th harmonic error	6th harmonic error	7th harmonic error
k01 [/s]	2192.54	2078.87	2086.42	2058.21	2105.65		239.956	189.362	0.000140105	22.0547	21.4003
E01 [V]	1.54032	1.5362	1.53617	1.53272	1.52752		0.0161271	0.00118048	0.000655134	0.00204414	0.00333
Kr [/s]	1.74365	2.10658	2.15832	2.13083	2.14637		0.894562	0.0759721	0.000759593	0.103789	0.176173
k02 [/s]	1.38922	1.38784	1.39322	1.40509	1.39244		0.13108	0.0346283	0.00305052	0.0214001	0.0238641
E02 [V]	1.33466	1.48118	1.48096	1.48273	1.48593		0.00239115	0.000987013	0.000403399	1.36E-03	0.00209804
k03 [/s]	1.49598	1.4793	1.45981	1.46625	1.44477		0.128051	0.0303112	0.000641609	0.00990897	0.0353771
E03 [V]	1.15362	1.15643	1.13811	1.13091	1.13991		0.00361503	0.000678105	0.000122289	0.000356985	0.00102602
k04 [/s]	12.0458	11.945	1.20E+01	11.9323	12.0395		1.85859	0.677611	0.0125287	0.211185	0.254632
E04 [V]	0.886737	0.888626	0.884393	0.900015	0.896222		0.00444134	0.00209546	0.000163972	8.30E-04	0.000977336
kc1 [/s]	1.61E+02	1.60E+02	161.408	161.133	159.876		1.01E+01	2.08392	0.023066	1.71021	2.30907
kc2 [/s]	1.62E+01	1.56E+01	1.54E+01	1.56E+01	1.56E+01		1.01E+00	0.424078	0.0128316	3.59E-01	5.40E-01
kad1 [/s]	103.006	102.654	103.783	101.458	101.19		19.1477	6.68498	0.00165931	1.75806	2.8453
kad2 [/s]	24.7194	24.8396	24.4559	25.3872	24.8423		2.50584	0.545476	0.00568126	0.232837	0.192538
n0 [/]	8.34E-10	8.23E-10	8.05E-10	7.88E-10	8.20E-10		2.25E-11	2.92E-11	2.85E-12	8.38E-12	1.51E-11
Cdl [F]	4.89E-06	4.85E-06	4.83E-06	4.80E-06	4.80E-06		5.59E-07	2.24E-07	9.60E-05	1.14E-07	1.86E-07
Sa [/]	11.3309	11.5394	12.0105	11.6951	11.5237		0.333812	0.510822	0.0121153	1.58E-01	0.137938
Sb [/]	1.82534	1.82505	1.85519	1.77825	1.82121		0.0855489	0.0894937	0.00432717	0.040804	0.0329796
Sc [/]	7.18E-01	7.18E-01	7.15E-01	7.39E-01	0.717998		9.96E-02	0.0390775	0.00157178	1.92E-02	0.0193131
Sd [/]	8.12793	7.97997	8.33163	7.97009	8.07203		0.931907	0.569207	0.00662879	0.254102	0.141698
Se [/]	0.0390618	0.0388724	0.0384759	0.0397043	3.95E-02		0.0107348	0.00421537	0.00130293	0.000604174	8.58E-04
Sf [/]	19.1389	18.9215	19.3284	18.5371	18.7724		0.97091	1.357	0.00758313	0.383705	0.234101
Sn [/]	7.36642	7.30349	7.33972	7.24217	7.29548		0.337682	0.215944	0.0108504	0.0788045	0.172971
alfa1 [/]	0.379962	0.378088	0.381064	0.381856	0.379058		0.0496798	0.0576437	0.00166364	0.0092511	0.0107075
alfa2 [/]	0.366346	0.357828	0.362263	0.370361	0.358473		0.0134606	0.0047955	0.00300663	0.00488711	0.00476965
alfa3 [/]	0.422935	0.422532	0.424088	0.42215	0.425721		0.0195446	0.00248608	0.000204135	2.49E-03	0.00220216
alfa4 [/]	0.562093	0.557793	0.547182	0.560033	0.564236		0.085196	0.0166838	0.000691508	0.0120912	0.00748244
Phi	0.249912632	0.160729356	0.155480173	0.1841708	0.258423465						

Ir Vulcan Low Region											
Constant	3rd harmonic fit	4th harmonic fit	5th harmonic fit	6th harmonic fit	7th harmonic fit		3rd harmonic error	4th harmonic error	5th harmonic error	6th harmonic error	7th harmonic error
k01 [/s]	326.091	496.247	405.254	278.336	469.768		72.7729	10.3744	0.0010748	7.82012	0.000261624
E01 [V]	1.47869	1.47853	1.90894	1.63125	1.60134		0.00731618	0.00166237	3.37E-06	0.020035	1.54E-06
Kr [/s]	0.0603339	0.0870058	459435	0.0616252	33.3798		0.00419302	0.0033643	19602.3	0.00158868	0.773595
k02 [/s]	0.62148	1.53322	1.89559	0.64179	0.907633		0.067087	0.0173704	3.69E-06	0.0217655	4.79E-07
E02 [V]	1.29322	1.31131	1.36481	1.32349	0.96031		0.00348753	0.000449205	1.58E-06	0.00841147	8.63E-08
k03 [/s]	1.18174	1.07585	1.34029	1.01483	1.59131		0.0597452	0.00850901	1.57E-06	0.0127923	1.87E-06
E03 [V]	1.09124	1.11766	1.0879	1.16425	0.957964		0.00282128	0.000622097	4.74E-07	0.0056373	3.83E-07
k04 [/s]	3.59289	10.0361	2.75E+00	3.98303	2.65208		0.238167	0.283888	3.56E-06	0.145049	1.30E-06
E04 [V]	0.936237	0.910582	0.89184	0.876854	0.768589		0.00421319	0.000826076	2.52E-06	0.0024996	7.36E-07
kc1 [/s]	1.06E+02	1.16E+02	128.703	131.679	74.8038		47.7134	2.38231	0.000236569	2.78781	3.49E-05
kc2 [/s]	1.75E+01	2.16E+01	3.99E+01	2.00E+01	2.28E+01		8.4374	0.424174	5.00E-05	3.54E-01	1.23E-05
kad1 [/s]	25.5423	64.7022	70.72	24.9484	87.4363		6.87019	1.48043	0.000132085	0.891811	2.65E-05
kad2 [/s]	27.3513	14.1581	4.34461	12.6259	6.20819		2.43559	0.311621	5.40E-06	0.627428	2.59E-06
n0 [/]	1.57E-10	1.00E-10	8.42E-11	1.37E-10	2.60E-11		1.50E-11	6.57E-13	8.98E-17	2.21E-12	1.31E-17
Cdl [F]	6.87E-06	6.57E-06	7.18E-06	7.65E-06	9.53E-06		7.94E-07	8.97E-08	1.29E-11	1.68E-07	6.11E-12
Sa [/]	10.6175	9.42322	12.5629	8.97608	11.0991		1.33365	0.156745	2.13E-05	0.00913654	6.02E-06
Sb [/]	2.60555	1.8029	1.63546	5.20833	2.89516		0.132	0.01603	4.82E-06	0.132147	1.19E-06
Sc [/]	3.02E+00	1.82E+00	1.06E+00	3.13E+00	1.11811		0.365175	0.0188152	2.38E-06	0.0518516	5.54E-07
Sd [/]	16.6362	15.5935	3.39885	3.59863	1.31401		4.07479	0.713804	1.06E-05	0.0946376	5.78E-07
Se [/]	0.0129375	0.00906953	0.0104636	0.0143948	9.10E-03		0.00370221	0.000306607	3.38E-08	0.000240223	2.65E-09
Sf [/]	13.9182	13.3916	17.3358	11.0888	16.6852		0.868378	0.481745	4.12E-05	0.18793	1.18E-05
Sn [/]	9.62898	10.2943	14.5196	12.4854	18.3928		1.2033	0.302695	2.31E-05	0.345469	1.09E-05
alfa1 [/]	0.877257	0.606443	0.52453	1.28706	0.626033		0.351523	0.00737356	1.25E-06	0.0301169	2.34E-07
alfa2 [/]	0.403061	0.361271	0.435137	0.343702	0.440574		0.00822577	0.00133485	3.93E-07	0.00662855	1.99E-07
alfa3 [/]	0.571731	0.580968	0.637232	0.493191	0.750633		0.00343088	0.0012125	4.87E-07	0.00505941	8.15E-07
alfa4 [/]	0.353388	0.852071	0.752512	0.268727	0.765138		0.0201102	0.00528384	4.91E-07	0.00466951	3.64E-07
Phi	0.212219786	0.102665543	0.299018233	0.382159191	0.403845057						

Ir Vulcan High Region											
Constant	3rd harmonic fit	4th harmonic fit	5th harmonic fit	6th harmonic fit	7th harmonic fit		3rd harmonic error	4th harmonic error	5th harmonic error	6th harmonic error	7th harmonic error
k01 [/s]	0.712648	0.252653	0.590814	0.513596	0.509107		5.233	0.0382346	40.4093	2.23E-05	1.62435
E01 [V]	1.52588	1.49421	1.45267	1.49935	1.50075		0.145488	0.0332216	1.31E+00	4.86E-05	0.114514
Kr [/s]	24.8457	9.00915	1.15504	65.8798	59.3458		175.08	13.1806	28.7343	3.17844	146.428
k02 [/s]	0.0541766	0.132757	0.0290679	0.11034	0.0814388		0.377544	0.0147289	1.04E+00	4.62E-06	0.113667
E02 [V]	1.42326	1.43021	1.41128	1.2889	1.30281		0.415707	0.0128447	1.19E+00	0.00187923	0.126269
k03 [/s]	0.329658	4.01649	0.756917	0.925651	0.874606		13.2056	0.817613	3.19E+02	2.96E-05	3.76055
E03 [V]	0.683143	0.731963	0.13578	0.277847	0.295443		0.849592	0.00908014	1.00E+02	2.17E-05	2.13722
k04 [/s]	0.543051	2.77614	2.19E+00	3.34921	2.85565		11.1724	0.440279	1.61E+03	0.000177252	28.3408
E04 [V]	0.86236	0.912679	0.327359	1.597	1.59826		1.21742	0.0114516	5.79E+00	7.32E-07	0.412244
kc1 [/s]	1366.75	9.43E+01	160.777	463.996	30.796		70884.5	15.0542	47590.3	0.00752475	124.427
kc2 [/s]	23.3083	6.03E+01	1.54E+01	-2.85E+01	5.18E+00		4.83E-05	8.02221	6197.39	1.97E-04	3.07E+01
kad1 [/s]	7.15817	12.7019	63.7909	35.9375	36.4864		166.636	1.37559	39047.3	0.000335988	179.162
kad2 [/s]	9.74488	5.34259	18.9769	6.62059	6.25463		73.025	2.02681	1.27E+04	0.00462183	1.30234
n0 [/]	2.50E-11	2.29E-11	2.09E-11	3.62E-11	3.46E-11		3.95E-11	5.04E-12	7.07E-10	3.33E-16	1.09E-10
Cdl [F]	1.52E-05	3.87E-06	1.38E-05	-7.66E-05	2.00E-04		1.90E-04	1.08E-06	1.53E-04	3.69E-10	1.23E-04
Sa [/]	44.5315	52.467	47.2603	29.713	41.6288		248.205	2.99897	2.23E+03	0.375463	57.2398
Sb [/]	0.270806	0.167659	0.176997	1.25217	1.02273		2.95607	0.0118118	2.58E+01	0.0492324	2.14966
Sc [/]	-0.552029	1.07E-02	2.31E+00	3.13E+00	2.2974		1.79493	0.000981883	1.19E+02	0.0045599	16.1493
Sd [/]	0.129863	0.102069	0.0291723	-5.7237	-7.93213		2.27727	2.11E-06	2.30E+01	0.000243514	29.7808
Se [/]	-0.0442702	-0.00858987	-0.00570765	0.0495665	-4.52E-02		1.49235	0.00126942	1.85E+00	0.0303838	2.12E-01
Sf [/]	-0.281446	2.48627	0.901291	0.00139556	-0.336965		2.98E+00	0.626818	4.34E+02	8.11E-08	1.22805
Sn [/]	-7.03974	1.09098	1.45128	1.0301	0.618575		4.85483	0.218843	628.641	1.74E-05	2.1427
alfa1 [/]	1.75107	1.24416	1.42109	0.786641	0.855445		0.9145	0.0855011	2.63E+00	7.47E-06	0.140556
alfa2 [/]	0.312789	0.365797	0.343761	0.302924	0.355988		1.30453	0.0970087	2.45E+00	1.15E-05	0.412648
alfa3 [/]	0.665206	0.728671	0.26158	0.946057	0.946842		1.64E-06	3.52E-05	2.78E+01	7.03E-05	0.395976
alfa4 [/]	0.453243	1.3364	2.68665	1.12784	1.15464		2.40764	0.133535	2.53E+02	6.15E-05	4.01921
Phi	0.01079269	0.30757422	0.029740681	0.180634955	0.071589323						

IrO_2 Low Region											
Constant	3rd harmonic fit	4th harmonic fit	5th harmonic fit	6th harmonic fit	7th harmonic fit		3rd harmonic error	4th harmonic error	5th harmonic error	6th harmonic error	7th harmonic error
k01 [/s]	326.49	880.573	880.573	880.572	519.526		1.50E-05	3.43E-07	1.52E-07	5.79E-08	8.90E+01
E01 [V]	1.56569	1.54006	1.57452	1.48573	1.58481		0.000881867	0.000808984	0.00121655	0.000719936	0.101954
Kr [/s]	6.41E-15	2.80E-29	-0.00932851	0.0368665	1.24E+01		1.31E-06	0.000461592	0.000406327	1.44E-05	2.14E+00
k02 [/s]	0.179363	0.348847	0.315993	0.419582	0.920235		0.000310048	0.000616623	0.000626117	9.48E-05	0.074967
E02 [V]	1.5431	1.40848	1.49687	1.41407	1.41056		0.000677757	0.000530147	0.00129309	0.0010916	0.115039
k03 [/s]	0.438519	0.711023	0.977379	0.439916	1.00682		0.000389123	0.0025492	0.00257405	0.00082256	4.59E-02
E03 [V]	1.12494	1.11295	1.10124	1.07639	1.16652		6.19E-05	8.18E-05	0.000113896	0.000122008	7.99E-04
k04 [/s]	2.80127	3.69099	3.68E+00	3.91905	2.31674		0.000540954	0.000132139	0.000387721	0.000377374	0.0343216
E04 [V]	0.680571	0.830891	0.830858	0.844359	0.846333		8.27E-05	3.50E-05	7.35E-05	4.96E-05	9.78E-04
kc1 [/s]	7.34E-03	5.72E-03	0.00374792	-0.00725499	0.0079411		0.000100248	9.09E-05	2.51E-05	0.000229695	1.02E-03
kc2 [/s]	5.41E-05	2.34E-06	-2.08E-03	1.49E-01	4.21E-03		0.000122823	9.97E-05	1.43E-05	1.63E-03	7.86E-04
kad1 [/s]	0.0354231	0.331857	0.598277	0.681791	0.602396		0.000137562	0.00107214	0.00117436	0.000513672	1.14E-01
kad2 [/s]	9.55805	15.5991	15.5893	15.6133	16.9698		0.00283874	1.84E-05	0.000204573	4.78E-05	1.46234
n0 [/]	3.37E-10	2.30E-10	1.94E-10	1.56E-10	1.38E-10		4.20E-13	2.69E-13	3.15E-13	1.59E-13	1.65E-12
Cdl [F]	5.08E-06	3.28E-05	3.82E-04	4.36E-04	5.33E-04		5.36E-05	2.00E-06	2.88E-06	8.72E-06	3.98E-05
Sa [/]	149.345	10.1347	10.1262	10.0954	8.32716		5.07E-07	2.20E-05	4.18E-05	7.88E-06	5.04E-01
Sb [/]	0.632795	0.24346	0.220236	0.400673	0.0338097		7.57E-05	0.000331874	0.00328754	1.36E-05	4.30E-08
Sc [/]	6.82E-01	1.16E+00	1.12E+00	9.89E-01	2.61267		0.000212005	0.000361169	0.000688861	1.69E-06	0.132061
Sd [/]	0.0324003	0.111359	0.51338	-0.141632	0.433245		0.000742089	0.000291062	0.00441091	0.00251356	2.03E-02
Se [/]	1.06958	1.05523	1.13735	0.580667	1.10E+00		0.000491948	0.00156369	0.00234987	0.000955434	1.42E-02
Sf [/]	3.47429	1.75144	1.72304	2.42555	1.90467		0.000575474	0.00107665	0.00240299	0.00179511	0.000501139
Sn [/]	0.00711292	0.363499	0.281526	0.376396	0.279139		1.63E-07	8.31E-05	5.78E-05	0.00211771	1.18E-02
alfa1 [/]	0.669533	0.922356	0.849899	0.849382	1.3058		0.000561547	0.000281888	9.11E-05	6.50E-06	0.0193526
alfa2 [/]	0.436201	0.344985	0.235344	-0.395078	0.0182369		0.000551677	0.000781288	0.0023103	4.83E-05	2.74E-03
alfa3 [/]	0.45733	0.471883	0.465741	0.555505	0.491657		9.97E-06	0.000457762	0.000322437	0.000243075	0.00252809
alfa4 [/]	1.25142	0.570664	0.599987	1.21411	0.728058		0.000432026	0.00132218	0.0010258	0.00174224	4.19E-03
Phi	0.214019371	0.131333025	0.21057881	0.198166653	0.338911757						

IrO_2 High Region											
Constant	3rd harmonic fit	4th harmonic fit	5th harmonic fit	6th harmonic fit	7th harmonic fit		3rd harmonic error	4th harmonic error	5th harmonic error	6th harmonic error	7th harmonic error
k01 [/s]	1688.51	983.839	781.532	2140.63	567.277		1.26E-06	8.09E+02	1.44E-07	2.67E+02	3.28E+02
E01 [V]	1.57049	1.54123	1.57921	1.52662	1.58295		0.00020824	0.0157241	0.000826206	0.0033964	0.00930624
Kr [/s]	2.64E+00	1.10E+01	14.882	14.3539	1.40E+01		6.10E-04	1.77734	0.000231441	2.82E+00	2.44E+00
k02 [/s]	0.855991	0.347392	1.33618	0.174548	0.886402		3.08E-06	0.0625854	0.000937486	1.26E-02	0.172127
E02 [V]	1.39063	1.55843	1.47516	1.24947	1.43654		0.000369296	0.0164221	0.00335013	0.110437	0.129423
k03 [/s]	0.483081	0.701689	2.33264	0.468426	1.65909		0.00322662	0.00564117	0.00802407	0.00789191	1.11E-01
E03 [V]	1.10155	1.11562	1.10343	1.05043	1.1108		2.53E-04	4.57E-04	0.000331535	0.00173723	2.22E-03
k04 [/s]	0.983534	3.50743	1.97E+00	1.28971	2.28595		0.00476079	0.107084	0.000461466	0.0753687	0.232335
E04 [V]	0.873819	0.823669	0.830537	0.872127	0.863268		2.86E-04	4.79E-04	3.24E-04	2.77E-03	4.53E-03
kc1 [/s]	5.20E-03	4.44E-03	0.00795435	0.000351877	0.00711798		0.00020379	9.04E-05	5.23E-04	9.04E-05	1.58E-03
kc2 [/s]	2.17E-03	2.20E-06	2.45E-03	7.19E-03	3.69E-03		0.000338869	1.76E-06	1.80E-04	1.29E-03	5.40E-04
kad1 [/s]	0.316109	0.66173	0.44522	0.303355	0.548566		0.00520284	0.122141	0.00447154	0.0649174	9.65E-02
kad2 [/s]	12.5735	9.07082	12.3885	21.9649	25.9536		0.000275443	1.70E+00	0.000147736	4.83E+00	8.89414
n0 [/]	2.97E-10	2.16E-10	1.87E-10	1.84E-10	1.46E-10		9.71E-13	8.85E-13	1.26E-12	5.45E-12	7.62E-12
Cdl [F]	3.77E-04	3.17E-05	3.95E-06	4.85E-04	6.27E-04		5.30E-06	5.05E-06	8.63E-06	2.75E-05	1.84E-04
Sa [/]	14.8453	9.06765	6.03831	23.9306	10.714		2.07E-04	3.20E+00	9.82E-04	4.68E+00	3.83E+00
Sb [/]	0.302449	0.237998	0.176872	-0.0414569	0.0530273		3.91E-03	0.140805	0.00156986	4.20E-03	0.00837179
Sc [/]	5.37E-01	1.13E+00	3.51E+00	6.13E-01	2.10019		0.00304586	0.452489	0.000306284	1.44E-01	0.324725
Sd [/]	0.0562165	0.16827	0.335026	0.0833389	0.421338		0.00351946	0.0160928	0.0185047	0.00807122	6.52E-02
Se [/]	0.890477	1.06196	0.85743	0.496492	1.02E+00		0.00247942	0.0129969	0.00950129	0.0268027	7.70E-02
Sf [/]	4.75911	1.96973	1.73161	3.34867	1.79309		0.00106472	0.0338392	0.0065574	0.102118	0.0790602
Sn [/]	0.110885	0.17007	0.317719	0.123214	0.314122		1.55E-03	3.14E-02	2.15E-04	0.0241576	2.27E-01
alfa1 [/]	1.09957	1.10045	0.679873	1.24156	0.992501		0.00217854	0.369814	3.31E-05	3.76E-01	0.184143
alfa2 [/]	0.0998058	0.24759	0.170773	0.0392828	0.0173229		0.00276701	0.0396561	0.00802778	3.75E-03	1.71E-03
alfa3 [/]	0.485608	0.472509	0.417933	0.567626	0.428091		1.34E-03	0.00126927	0.00167853	0.00532518	0.00730444
alfa4 [/]	0.533911	0.406651	0.578378	0.902225	0.558027		0.00179451	0.00287861	0.00273491	0.0282842	2.05E-02
Phi	0.230898363	0.106302972	0.225380877	0.376482366	0.255851553						

References

[1] "Our world in data: global number of natural disaster by year." Accessed: Feb. 18, 2026. [Online]. Available: https://ourworldindata.org/grapher/natural-disasters-by-type

[2] *Global Drought Outlook*. OECD Publishing, 2025. doi: 10.1787/d492583a-en.

[3] "Carbon brief: increasing number of draughts." Accessed: Feb. 18, 2026. [Online]. Available: https://www.carbonbrief.org/multi-year-droughts-have-become-more-frequent-drier-and-hotter-over-past-40-years/

[4] "The Guardian: Snow in texas." Accessed: Feb. 18, 2026. [Online]. Available: https://www.theguardian.com/us-news/2026/jan/26/winter-storm-snow-deaths-power-outages-travel

[5] H. Pearson, "The rise of eco-anxiety: scientists wake up to the mental-health toll of climate change," *Nature*, vol. 628, no. 8007, pp. 256–258, Apr. 2024, doi: 10.1038/d41586-024-00998-6.

[6] T. R. Oliver, "The politics of public health policy," 2006. doi: 10.1146/annurev.publhealth.25.101802.123126.

[7] A. Boretti, "Challenges of a 'free market' approach to the hydrogen economy," Sep. 19, 2024, *Elsevier Ltd.* doi: 10.1016/j.ijhydene.2024.08.086.

[8] A. Boretti and B. G. Pollet, "Hydrogen economy: Paving the path to a sustainable, low-carbon future," Dec. 03, 2024, *Elsevier Ltd.* doi: 10.1016/j.ijhydene.2024.10.350.

[9] R. S. El-Emam and H. Özcan, "Comprehensive review on the techno-economics of sustainable large-scale clean hydrogen production," May 20, 2019, *Elsevier Ltd.* doi: 10.1016/j.jclepro.2019.01.309.

[10] "Our world in data: Consuption of fuel by type." Accessed: Feb. 18, 2026. [Online]. Available: https://ourworldindata.org/grapher/energy-consumption-by-source-and-country

[11] I. Katsounaros and M. T. M. Koper, "Electrocatalysis for the hydrogen economy," in *Electrochemical Science for a Sustainable Society: A Tribute to John O'M Bockris*, Springer International Publishing, 2017, pp. 23–50. doi: 10.1007/978-3-319-57310-6_2.

[12] B. H. R. Suryanto, H. L. Du, D. Wang, J. Chen, A. N. Simonov, and D. R. MacFarlane, "Challenges and prospects in the catalysis of electroreduction of nitrogen to ammonia," *Nat. Catal.*, vol. 2, no. 4, pp. 290–296, Feb. 2019, doi: 10.1038/s41929-019-0252-4.

[13] A. Kovač, M. Paranos, and D. Marciuš, "Hydrogen in energy transition: A review," *Int. J. Hydrogen Energy*, vol. 46, no. 16, pp. 10016–10035, Mar. 2021, doi: 10.1016/j.ijhydene.2020.11.256.

[14] N. M. Markovic, "Electrocatalysis: Interfacing electrochemistry," 2013, *Nature Publishing Group*. doi: 10.1038/nmat3554.

[15] Z. W. She, J. Kibsgaard, C. F. Dickens, I. Chorkendorff, J. K. Nørskov, and T. F. Jaramillo, "Combining theory and experiment in electrocatalysis: Insights into materials

design," Feb. 2017, *American Association for the Advancement of Science*. doi: 10.1126/science.aad4998.

[16] E. Guerrini and S. Trasatti, "Recent developments in understanding factors of electrocatalysis," in *Russian Journal of Electrochemistry*, Feb. 2006, pp. 1017–1025. doi: 10.1134/S1023193506100053.

[17] A. S. Bandarenka, E. Ventosa, A. Maljusch, J. Masa, and W. Schuhmann, "Techniques and methodologies in modern electrocatalysis: evaluation of activity, selectivity and stability of catalytic materials," *Analyst*, vol. 139, no. 6, pp. 1274–1291, 2014, doi: 10.1039/c3an01647a.

[18] J. Swaminathan and A. Meiyazhagan, "Characterization of electrocatalyst," in *Methods for Electrocatalysis: Advanced Materials and Allied Applications*, Springer International Publishing, 2020, pp. 425–451. doi: 10.1007/978-3-030-27161-9_17.

[19] L. R. B. Allen J.; Faulkner and W. S. Henry, *Electrochemical Methods: Fundamentals and Applications*, 3rd Edition. John Wiley Sons, inc., 2022.

[20] N. Djilali, "Computational modelling of polymer electrolyte membrane (PEM) fuel cells: Challenges and opportunities," *Energy*, vol. 32, no. 4, pp. 269–280, 2007, doi: 10.1016/j.energy.2006.08.007.

[21] A. M. Bond, E. A. Mashkina, and A. N. Simonov, "A Critical Review of the Methods Available for Quantitative Evaluation of Electrode Kinetics at Stationary Macrodisk Electrodes," *Developments in Electrochemistry: Science Inspired by Martin Fleischmann*, vol. 9781118694, pp. 21–47, 2014, doi: 10.1002/9781118694404.ch2.

[22] A. M. Bond, J. Zhang, L. Gundry, and G. F. Kennedy, "Opportunities and challenges in applying machine learning to voltammetric mechanistic studies," Feb. 2022, *Elsevier B.V.* doi: 10.1016/j.coelec.2022.101009.

[23] L. Gundry *et al.*, "Recent advances and future perspectives for automated parameterisation, Bayesian inference and machine learning in voltammetry," *Chemical Communications*, vol. 57, no. 15, pp. 1855–1870, 2021, doi: 10.1039/d0cc07549c.

[24] T. Peachey *et al.*, "Leveraging e-Science infrastructure for electrochemical research," *Philosophical Transactions of the Royal Society A: Mathematical, Physical and Engineering Sciences*, vol. 369, no. 1949, pp. 3336–3352, 2011, doi: 10.1098/rsta.2011.0146.

[25] W. Schmickler and E. Santos, *Interfacial Electrochemistry*. Springer Berlin Heidelberg, 2010. doi: 10.1007/978-3-642-04937-8.

[26] J. Wang, *Analytical electrochemistry*. Wiley-VCH, 2000.

[27] W. Zheng, "Python for Electrochemistry: A Free and All-In-One Toolset," Feb. 2023, *Institute of Physics*. doi: 10.1149/2754-2734/acff0b.

[28] D. S. Jorg Britz, *Digital Cyclic Voltammetry*, Fourth Edi. Springer US, 2016.

[29] E. J. F. Dickinson, J. G. Limon-Petersen, N. V. Rees, and R. G. Compton, "How Much Supporting Electrolyte Is Required to Make a Cyclic Voltammetry Experiment Quantitatively 'Diffusional'? A Theoretical and Experimental Investigation," *The Journal of Physical Chemistry C*, vol. 113, no. 25, pp. 11157–11171, Jun. 2009, doi: 10.1021/jp901628h.

[30] "ElectroKitty Git Hub page," Accessed: May 22, 2026. [Online]. Available: https://github.com/RedrumKid/ElectroKitty

[31] O. Vodeb, P. Farinazzo Bergamo Dias Martins, D. Strmčnik, N. Hodnik, and M. Gaberšček, "ElectroKitty: A Python Tool for Modeling Electrochemical Data Including Non-Langmuir Adsorption," *ACS Electrochemistry*, vol. 1, no. 8, pp. 1540–1544, Aug. 2025, doi: 10.1021/acselectrochem.4c00218.

[32] W. Schmickler, "A THEORY OF ADIABATIC ELECTRON-TRANSFER REACTIONS l," Elsevter Sequoia S.A, 1986.

[33] E. Santos, P. Quaino, and W. Schmickler, "Theory of electrocatalysis: Hydrogen evolution and more," *Physical Chemistry Chemical Physics*, vol. 14, no. 32, pp. 11224–11233, Jul. 2012, doi: 10.1039/c2cp40717e.

[34] R. A. Marcus, "Chemical and Electrochemical Electron-Transfer Theory," *Annu. Rev. Phys. Chem.*, vol. 15, no. 1, pp. 155–196, Oct. 1964, doi: 10.1146/annurev.pc.15.100164.001103.

[35] R. A. Marcus, "On the theory of oxidation-reduction reactions involving electron transfer. I," *J. Chem. Phys.*, vol. 24, no. 5, pp. 966–978, 1956, doi: 10.1063/1.1742723.

[36] R. A. Marcus, "On the Theory of Electron-Transfer Reactions. VI. Unified Treatment for Homogeneous and Electrode Reactions," *J. Chem. Phys.*, vol. 43, no. 2, pp. 679–701, Jul. 1965, doi: 10.1063/1.1696792.

[37] N. S. Hush, "Adiabatic rate processes at electrodes. I. Energy-charge relationships," *J. Chem. Phys.*, vol. 28, no. 5, pp. 962–972, 1958, doi: 10.1063/1.1744305.

[38] W. Schmickler and D. Henderson, "NEW MODELS FOR THE STRUCTURE OF THE ELECTROCHEMICAL INTERFACE," 1986.

[39] N. Garcia-Araez, J. J. Lukkien, M. T. M. Koper, and J. M. Feliu, "Competitive adsorption of hydrogen and bromide on Pt(1 0 0): Mean-field approximation vs. Monte Carlo simulations," *Journal of Electroanalytical Chemistry*, vol. 588, no. 1, pp. 1–14, Mar. 2006, doi: 10.1016/j.jelechem.2005.11.034.

[40] N. Garcia-Araez, J. J. Lukkien, M. T. M. Koper, and J. M. Feliu, "Competitive adsorption of hydrogen and bromide on Pt(1 0 0): Mean-field approximation vs. Monte Carlo simulations," *Journal of Electroanalytical Chemistry*, vol. 588, no. 1, pp. 1–14, Mar. 2006, doi: 10.1016/j.jelechem.2005.11.034.

[41] C. H. Turner, Z. Zhang, L. D. Gelb, and B. I. Dunlap, "Kinetic Monte Carlo Simulation of Electrochemical Systems," 2015.

[42] S. W. Feldberg, "Improvements on Computer Simulation of Electrochemical Phenomena Involving Hydrodynamics: The Rotating Disk and Dropping Mercury Electrode," *Journal of Electroanalytical Chemistry*, vol. 109, pp. 69–82, 1980.

[43] S. W. Feldberg, C. I. Goldstein, and M. Rudolph, "A stability criterion for accurate simulation of electrochemical diffusion-kinetic phenomena at the rotating disk electrode and implications for simulation of diffusion-migration and other problems," *Journal of Electroanalytical Chemistry*, vol. 413, no. 1–2, pp. 25–36, 1996, doi: 10.1016/0022-0728(96)04625-6.

[44] M. Rudolph, D. P. Reddy, and S. W. Feldberg, "A Simulator for Cyclic Voltammetric Responses," *Anal. Chem.*, vol. 66, no. 10, pp. 589A-600A, Feb. 1994, doi: 10.1021/ac00082a725.

[45] S. W. Feldberg, M. L. Bowers, and F. C. Anson, “Hopscotch-finite-difference simulation of the rotating ring-disc electrode,” *Journal of Electroanalytical Chemistry*, vol. 215, no. 1–2, pp. 11–28, 1986, doi: 10.1016/0022-0728(86)87002-4.

[46] D. Britz and J. Strutwolf, “Higher-order spatial discretisations in electrochemical digital simulations. Part 4. Discretisation on an arbitrarily spaced grid,” *Comput. Biol. Chem.*, vol. 27, no. 3, pp. 327–337, 2003, doi: 10.1016/S1476-9271(02)00080-4.

[47] “DigiElch.” [Online]. Available: https://www.gamry.com/cells-and-accessories/digielch-electrochemical-simulation-software/

[48] “Comsol package.” Accessed: Feb. 05, 2026. [Online]. Available: https://www.comsol.com/

[49] “OpenFoaem package.” Accessed: Feb. 05, 2026. [Online]. Available: https://www.openfoam.com/

[50] G. F. Kennedy, A. M. Bond, and A. N. Simonov, “Modelling ac voltammetry with MECSim: facilitating simulation–experiment comparisons,” *Curr. Opin. Electrochem.*, vol. 1, no. 1, pp. 140–147, 2017, doi: 10.1016/j.coelec.2016.12.001.

[51] A. M. Bond, N. W. Duffy, S. X. Guo, J. Zhang, and D. Elton, “Changing the look of voltammetry,” *Anal. Chem.*, vol. 77, no. 9, 2005, doi: 10.1021/ac053370k.

[52] N. Hansen, “The CMA Evolution Strategy: A Tutorial,” Feb. 2016, [Online]. Available: http://arxiv.org/abs/1604.00772

[53] W. H. Press, S. A. Teukolsky, W. T. Vetterling, and B. P. Flannery, *Numerical recipes*, 3. Edition. Cambridge university press, 2011. doi: 10.1017/cbo9780511599798.031.

[54] W. Zheng, “Python for Electrochemistry: A Free and All-In-One Toolset,” Dec. 01, 2023, *Institute of Physics*. doi: 10.1149/2754-2734/acff0b.

[55] “Software from Gamry instruments.” Accessed: Oct. 25, 2024. [Online]. Available: https://www.gamry.com/support-2/software/

[56] “NOVA.” Accessed: Oct. 25, 2024. [Online]. Available: https://www.metrohm.com/en/service/software-center/nova.html

[57] “EC lab.” Accessed: Oct. 25, 2024. [Online]. Available: https://www.biologic.net/topics/ec-lab/

[58] A. M. Bond, N. W. Duffy, S. X. Guo, J. Zhang, and D. Elton, “Changing the look of voltammetry,” *Anal. Chem.*, vol. 77, no. 9, 2005, doi: 10.1021/ac053370k.

[59] A. M. Bond, J. Zhang, L. Gundry, and G. F. Kennedy, “Opportunities and challenges in applying machine learning to voltammetric mechanistic studies,” Aug. 01, 2022, *Elsevier B.V.* doi: 10.1016/j.coelec.2022.101009.

[60] L. Gundry *et al.*, “Recent advances and future perspectives for automated parameterisation, Bayesian inference and machine learning in voltammetry,” *Chemical Communications*, vol. 57, no. 15, pp. 1855–1870, Feb. 2021, doi: 10.1039/d0cc07549c.

[61] M. Rudolph, D. P. Reddy, and S. W. Feldberg, “A Simulator for Cyclic Voltammetric Responses,” *Anal. Chem.*, vol. 66, no. 10, pp. 589A-600A, May 1994, doi: 10.1021/ac00082a725.

[62] “DigiElch.” Accessed: Oct. 25, 2024. [Online]. Available: https://www.gamry.com/cells-and-accessories/digielch-electrochemical-simulation-software/

[63] “MECSim webpage.” Accessed: Oct. 25, 2024. [Online]. Available: https://garethkennedy.net/MECSim.html

[64] G. F. Kennedy, A. M. Bond, and A. N. Simonov, "Modelling ac voltammetry with MECSim: facilitating simulation–experiment comparisons," Feb. 01, 2017, *Elsevier B.V.* doi: 10.1016/j.coelec.2016.12.001.

[65] "KISSA group." Accessed: Oct. 25, 2024. [Online]. Available: http://www.kissagroup.com/

[66] R. Johansson, "Numerical python: Scientific computing and data science applications with numpy, SciPy and matplotlib, Second edition," 2018. doi: 10.1007/978-1-4842-4246-9.

[67] W. Jakob, J. Rhinelander, and D. Moldovan, "pybind11 – Seamless operability between C++11 and Python," 2017.

[68] B. Fornberg, "Generation of Finite Difference Formulas on Arbitrarily Spaced Grids," *Math. Comput.*, vol. 51, no. 184, p. 699, 1988, doi: 10.2307/2008770.

[69] J. Britz, Dieter; Strutwolf, *Digital Cyclic Voltammetry*, Fourth Edi. Aarhus, Dennmark: Springer US, 2016.

[70] "C++ implementation of hybrd method." Accessed: Oct. 25, 2024. [Online]. Available: https://people.sc.fsu.edu/~jburkardt/cpp_src/minpack/minpack.html

[71] M. J. D. Powell, "A Hybrid Method for Nonlinear Equations," in *Numerical Methods for Nonlinear Algebraic Equations*, P. Rabinowitz, Ed., Gordon and Breach, 1970.

[72] "User guide for MINPACK." Accessed: Oct. 25, 2024. [Online]. Available: https://www.mcs.anl.gov/~more/ANL8074a.pdf

[73] W. H. Press, S. A. Teukolsky, W. T. Vetterling, and B. P. Flannery, *Numerical recipes*, 3. Edition. Cambridge: Cambridge university press, 2011. doi: 10.1017/cbo9780511599798.031.

[74] N. Hansen, "The CMA Evolution Strategy: A Tutorial," Apr. 2016, [Online]. Available: http://arxiv.org/abs/1604.00772

[75] "cma package GitHub." Accessed: Oct. 25, 2024. [Online]. Available: https://github.com/CMA-ES/pycma

[76] L. Gundry *et al.*, "A Comparison of Bayesian Inference Strategies for Parameterisation of Large Amplitude AC Voltammetry Derived from Total Current and Fourier Transformed Versions," *ChemElectroChem*, vol. 8, no. 12, pp. 2238–2258, Jun. 2021, doi: 10.1002/celc.202100391.

[77] C. Andrieu and J. Thoms, "A tutorial on adaptive MCMC," *Stat. Comput.*, vol. 18, no. 4, pp. 343–373, Dec. 2008, doi: 10.1007/s11222-008-9110-y.

[78] M. Shao, Q. Chang, J.-P. Dodelet, and R. Chenitz, "Recent Advances in Electrocatalysts for Oxygen Reduction Reaction," *Chem. Rev.*, vol. 116, no. 6, pp. 3594–3657, Mar. 2016, doi: 10.1021/acs.chemrev.5b00462.

[79] J. X. Wang *et al.*, "Multi-Step Oxygen Reduction Reaction (ORR) Kinetics on Pt including Water Activation," 2007.

[80] M. Moore, A. Putz, and M. Secanell, "Development of a Cathode Electrode Model Using the ORR Dual-Trap Intrinsic Kinetic Model," in *ASME 2012 10th International Conference on Fuel Cell Science, Engineering and Technology*, American Society of Mechanical Engineers, Jul. 2012, pp. 367–376. doi: 10.1115/FuelCell2012-91150.

[81] M. Moore, A. Putz, and M. Secanell, "Investigation of the ORR Using the Double-Trap Intrinsic Kinetic Model," *J. Electrochem. Soc.*, vol. 160, no. 6, pp. F670–F681, 2013, doi: 10.1149/2.123306jes.

[82] N. Fukaya, H. Murata, M. Shibata, and R. Jinnouchi, "Micro-kinetic mean-field model of subsurface oxidation in a platinum electrocatalyst," *Electrochim. Acta*, vol. 464, Oct. 2023, doi: 10.1016/j.electacta.2023.142867.

[83] J. X. Wang, J. Zhang, and R. R. Adzic, "Double-trap kinetic equation for the oxygen reduction reaction on pt(111) in acidic media," *Journal of Physical Chemistry A*, vol. 111, no. 49, pp. 12702–12710, Dec. 2007, doi: 10.1021/jp076104e.

[84] A. Kuzume, E. Herrero, and J. M. Feliu, "Oxygen reduction on stepped platinum surfaces in acidic media," *Journal of Electroanalytical Chemistry*, vol. 599, no. 2, pp. 333–343, Jan. 2007, doi: 10.1016/j.jelechem.2006.05.006.

[85] A. M. Gómez-Marín and J. M. Feliu, "Pt(1 1 1) surface disorder kinetics in perchloric acid solutions and the influence of specific anion adsorption," in *Electrochimica Acta*, Nov. 2012, pp. 558–569. doi: 10.1016/j.electacta.2012.04.066.

[86] A. Björling, E. Herrero, and J. M. Feliu, "Electrochemical oxidation of Pt(1 1 1) vicinal surfaces: Effects of surface structure and specific anion adsorption," *Journal of Physical Chemistry C*, vol. 115, no. 31, pp. 15509–15515, Aug. 2011, doi: 10.1021/jp204306k.

[87] A. M. Gómez-Marín, J. Clavilier, and J. M. Feliu, "Sequential Pt(1 1 1) oxide formation in perchloric acid: An electrochemical study of surface species inter-conversion," *Journal of Electroanalytical Chemistry*, vol. 688, pp. 360–370, 2013, doi: 10.1016/j.jelechem.2012.07.016.

[88] R. Rizo *et al.*, "Investigating the presence of adsorbed species on Pt steps at low potentials," *Nat. Commun.*, vol. 13, no. 1, p. 2550, May 2022, doi: 10.1038/s41467-022-30241-7.

[89] I. M. Tidswell, N. M. Markovic, and P. N. Ross, "Potential dependent surface structure of the Pt(1 1 1) electrolyte interface," *Journal of Electroanalytical Chemistry*, vol. 376, no. 1–2, pp. 119–126, Oct. 1994, doi: 10.1016/0022-0728(94)03553-9.

[90] D. Y. Chung *et al.*, "Dynamic stability of active sites in hydr(oxy)oxides for the oxygen evolution reaction," *Nat. Energy*, vol. 5, no. 3, pp. 222–230, Mar. 2020, doi: 10.1038/s41560-020-0576-y.

[91] M. Ruge *et al.*, "Structural Reorganization of Pt(111) Electrodes by Electrochemical Oxidation and Reduction," *J. Am. Chem. Soc.*, vol. 139, no. 12, pp. 4532–4539, Mar. 2017, doi: 10.1021/jacs.7b01039.

[92] T. Fuchs *et al.*, "Driving Force of the Initial Step in Electrochemical Pt(111) Oxidation," *Journal of Physical Chemistry Letters*, vol. 14, no. 14, pp. 3589–3593, Apr. 2023, doi: 10.1021/acs.jpclett.3c00520.

[93] A. Berná, V. Climent, and J. M. Feliu, "New understanding of the nature of OH adsorption on Pt(1 1 1) electrodes," *Electrochem. commun.*, vol. 9, no. 12, pp. 2789–2794, Dec. 2007, doi: 10.1016/j.elecom.2007.09.018.

[94] A. M. Gómez-Marín and J. M. Feliu, "Oxide growth dynamics at Pt(1 1 1) in absence of specific adsorption: A mechanistic study," *Electrochim. Acta*, vol. 104, pp. 367–377, 2013, doi: 10.1016/j.electacta.2012.10.075.

[95] N. Markovic, "Surface science studies of model fuel cell electrocatalysts," *Surf. Sci. Rep.*, vol. 45, no. 4–6, pp. 117–229, Apr. 2002, doi: 10.1016/S0167-5729(01)00022-X.

[96] N. M. Marković, R. R. Adžić, B. D. Cahan, and E. B. Yeager, "Structural effects in electrocatalysis: oxygen reduction on platinum low index single-crystal surfaces in

perchloric acid solutions," *Journal of Electroanalytical Chemistry*, vol. 377, no. 1–2, pp. 249–259, Oct. 1994, doi: 10.1016/0022-0728(94)03467-2.

[97] N. M. Marković, H. A. Gasteiger, and P. N. Ross, "Oxygen Reduction on Platinum Low-Index Single-Crystal Surfaces in Alkaline Solution: Rotating Ring Disk $_{Pt(\ hkl\ )}$ Studies," *J. Phys. Chem.*, vol. 100, no. 16, pp. 6715–6721, Apr. 1996, doi: 10.1021/jp9533382.

[98] S. G. Rinaldo, W. Lee, J. Stumper, and M. Eikerling, "Mechanistic Principles of Platinum Oxide Formation and Reduction," *Electrocatalysis*, vol. 5, no. 3, pp. 262–272, Jul. 2014, doi: 10.1007/s12678-014-0189-y.

[99] D. Shen, Y. Liu, G. Yang, H. Yu, and F. Peng, "Mechanistic Insights into Cyclic Voltammograms on Pt(111): Kinetics Simulations," *ChemPhysChem*, vol. 20, no. 21, pp. 2791–2798, Nov. 2019, doi: 10.1002/cphc.201900804.

[100] V. Viswanathan, H. A. Hansen, J. Rossmeisl, T. F. Jaramillo, H. Pitsch, and J. K. Nørskov, "Simulating linear sweep voltammetry from first-principles: Application to electrochemical oxidation of water on Pt(111) and Pt 3Ni(111)," *Journal of Physical Chemistry C*, vol. 116, no. 7, pp. 4698–4704, Feb. 2012, doi: 10.1021/jp210802q.

[101] M. T. M. Koper and J. J. Lukkien, "Modeling the butterfly: the voltammetry of ($\sqrt{3}\times\sqrt{3}$)R30° and p(2×2) overlayers on (111) electrodes," *Journal of Electroanalytical Chemistry*, vol. 485, no. 2, pp. 161–165, May 2000, doi: 10.1016/S0022-0728(00)00109-1.

[102] A. M. Gómez-Marín and J. M. Feliu, "Pt(1 1 1) surface disorder kinetics in perchloric acid solutions and the influence of specific anion adsorption," in *Electrochimica Acta*, Nov. 2012, pp. 558–569. doi: 10.1016/j.electacta.2012.04.066.

[103] A. M. Gómez-Marín and J. M. Feliu, "Oxide growth dynamics at Pt(1 1 1) in absence of specific adsorption: A mechanistic study," *Electrochim. Acta*, vol. 104, pp. 367–377, 2013, doi: 10.1016/j.electacta.2012.10.075.

[104] A. M. Gómez-Marín, J. Clavilier, and J. M. Feliu, "Sequential Pt(1 1 1) oxide formation in perchloric acid: An electrochemical study of surface species inter-conversion," *Journal of Electroanalytical Chemistry*, vol. 688, pp. 360–370, 2013, doi: 10.1016/j.jelechem.2012.07.016.

[105] S. Fletcher, C. S. Halliday, D. Gates, M. Westcott, T. Lwln, and G. Nelson, "THE RESPONSE OF SOME NUCLEATION/GROWTH PROCESSES TO TRIANGULAR SCANS OF POTENTIAL," Elsevier Sequoia S.A, 1983.

[106] T. Wandlowski, "Phase Transitions in Two-dimensional Adlayers at Electrode Surfaces: Thermodynamics, Kinetics, and Structural Aspects," in *Encyclopedia of Electrochemistry*, Wiley, 2002. doi: 10.1002/9783527610426.bard010303.

[107] B. A. Bewick, M. Fleischmann, and H. R. Thirsk, "Kinetics of the Electrocrystallization of Thin Films of Calomel Hg-eSHgL. + slow."

[108] C. Cachet, I. Epelboin, M. Keddam, and R. Wiart, "THE Ag/Ag ÷ SYSTEM: AN IMPEDANCE MODEL FOR NUCLEATION AND GROWTH," 1979.

[109] A. Milchev and M. I. Montenegro, "A galvanostatic study of electrochemical nucleation," Elsevier Sequoia S.A, 1992.

[110] A. Milchev, S. Stoyanov, and R. Kaischev, "Atomistic theory of electrolytic nucleation: I," *Thin Solid Films*, vol. 22, no. 3, pp. 255–265, Jul. 1974, doi: 10.1016/0040-6090(74)90296-X.

[111] A. Björling, E. Herrero, and J. M. Feliu, "Electrochemical Oxidation of Pt(1 1 1) Vicinal Surfaces: Effects of Surface Structure and Specific Anion Adsorption," *The Journal of Physical Chemistry C*, vol. 115, no. 31, pp. 15509–15515, Aug. 2011, doi: 10.1021/jp204306k.

[112] L. Jacobse *et al.*, "Electrochemical oxidation of Pt(111) beyond the place-exchange model," *Electrochim. Acta*, vol. 407, p. 139881, Mar. 2022, doi: 10.1016/j.electacta.2022.139881.

[113] M. J. Rost, L. Jacobse, and M. T. M. Koper, "Non-Random Island Nucleation in the Electrochemical Roughening on Pt(111)," *Angew. Chem. Int. Ed.*, vol. 62, no. 27, Jul. 2023, doi: 10.1002/anie.202216376.

[114] L. Jacobse, Y. F. Huang, M. T. M. Koper, and M. J. Rost, "Correlation of surface site formation to nanoisland growth in the electrochemical roughening of Pt(111)," *Nat. Mater.*, vol. 17, no. 3, pp. 277–282, Mar. 2018, doi: 10.1038/s41563-017-0015-z.

[115] V. Viswanathan, H. A. Hansen, J. Rossmeisl, T. F. Jaramillo, H. Pitsch, and J. K. Nørskov, "Simulating linear sweep voltammetry from first-principles: Application to electrochemical oxidation of water on Pt(111) and Pt 3Ni(111)," *Journal of Physical Chemistry C*, vol. 116, no. 7, pp. 4698–4704, 2012, doi: 10.1021/jp210802q.

[116] "cma package GitHub." [Online]. Available: https://github.com/CMA-ES/pycma

[117] L. Jacobse, Y. F. Huang, M. T. M. Koper, and M. J. Rost, "Correlation of surface site formation to nanoisland growth in the electrochemical roughening of Pt(111)," *Nat. Mater.*, vol. 17, no. 3, pp. 277–282, Mar. 2018, doi: 10.1038/s41563-017-0015-z.

[118] D. Boden, I. M. N. Groot, and J. Meyer, "Elucidating the Initial Oxidation of Pt(111) Using Large-Scale Atomistic Thermodynamics: A ReaxFF Study," *Journal of Physical Chemistry C*, vol. 126, no. 47, pp. 20020–20027, Dec. 2022, doi: 10.1021/acs.jpcc.2c05769.

[119] M. J. Rost, L. Jacobse, and M. T. M. Koper, "Non-Random Island Nucleation in the Electrochemical Roughening on Pt(111)," *Angew. Chem. Int. Ed.*, vol. 62, no. 27, Jul. 2023, doi: 10.1002/anie.202216376.

[120] H. Wendt and G. Imarisio, "Nine years of research and development on advanced water electrolysis. A review of the research programme of the Commission of the European Communities," *J. Appl. Electrochem.*, vol. 18, no. 1, pp. 1–14, Jan. 1988, doi: 10.1007/BF01016198.

[121] J. M. Skowroński and A. Ważny, "Nickel foam-based composite electrodes for electrooxidation of methanol," *Journal of Solid State Electrochemistry*, vol. 9, no. 12, pp. 890–899, Dec. 2005, doi: 10.1007/s10008-005-0046-2.

[122] S. P. Jiang and S. H. Chan, "A review of anode materials development in solid oxide fuel cells," *J. Mater. Sci.*, vol. 39, no. 14, pp. 4405–4439, Jul. 2004, doi: 10.1023/B:JMSC.0000034135.52164.6b.

[123] W. C. Dautremont-Smith, "Transition metal oxide electrochromic materials and displays: a review," *Displays*, vol. 3, no. 2, pp. 67–80, Apr. 1982, doi: 10.1016/0141-9382(82)90100-7.

[124] V. R. Stamenkovic, D. Strmcnik, P. P. Lopes, and N. M. Markovic, "Energy and fuels from electrochemical interfaces," *Nat. Mater.*, vol. 16, no. 1, pp. 57–69, Jan. 2017, doi: 10.1038/nmat4738.

[125] D. Kozlica *et al.*, "The role of individual nickel surface species in the hydrogen evolution reaction on nickel in alkaline electrolytes," Aug. 2025. doi: 10.21203/rs.3.rs-7285662/v1.

[126] R. Subbaraman *et al.*, "Trends in activity for the water electrolyser reactions on 3d M(Ni,Co,Fe,Mn) hydr(oxy)oxide catalysts," *Nat. Mater.*, vol. 11, no. 6, pp. 550–557, Jun. 2012, doi: 10.1038/nmat3313.

[127] A. G. Oshchepkov, A. Bonnefont, and E. R. Savinova, "On the Influence of the Extent of Oxidation on the Kinetics of the Hydrogen Electrode Reactions on Polycrystalline Nickel," *Electrocatalysis*, vol. 11, no. 2, pp. 133–142, Mar. 2020, doi: 10.1007/s12678-019-00560-3.

[128] A. G. Oshchepkov, A. Bonnefont, V. N. Parmon, and E. R. Savinova, "On the effect of temperature and surface oxidation on the kinetics of hydrogen electrode reactions on nickel in alkaline media," *Electrochim. Acta*, vol. 269, pp. 111–118, Apr. 2018, doi: 10.1016/j.electacta.2018.02.106.

[129] A. G. Oshchepkov *et al.*, "Exploring the Influence of the Nickel Oxide Species on the Kinetics of Hydrogen Electrode Reactions in Alkaline Media," *Top. Catal.*, vol. 59, no. 15–16, pp. 1319–1331, Sep. 2016, doi: 10.1007/s11244-016-0657-0.

[130] E. B. Ferreira and G. Jerkiewicz, "On the Electrochemical Reduction of β-Ni(OH)2 to Metallic Nickel," *Electrocatalysis*, vol. 12, no. 2, pp. 199–209, Mar. 2021, doi: 10.1007/s12678-021-00643-0.

[131] M. Alsabet, M. Grden, and G. Jerkiewicz, "Electrochemical Growth of Surface Oxides on Nickel. Part 1: Formation of α-Ni(OH)2 in Relation to the Polarization Potential, Polarization Time, and Temperature," *Electrocatalysis*, vol. 2, no. 4, pp. 317–330, Dec. 2011, doi: 10.1007/s12678-011-0067-9.

[132] K. L. Varvaris, D. Esau, F. M. Schuett, T. Jacob, and G. Jerkiewicz, "Surface Structure Dependence of Electrochemical Processes at Monocrystalline Nickel Electrodes. Part 1: The Hydrogen Evolution Reaction," *Journal of Physical Chemistry C*, vol. 127, no. 30, pp. 14711–14722, Feb. 2023, doi: 10.1021/acs.jpcc.3c01698.

[133] A. Seghiouer, J. Chevalet, A. Barhoun, and F. Lantelme, "Electrochemical oxidation of nickel in alkaline solutions: a voltammetric study and modelling," *Journal of Electroanalytical Chemistry*, vol. 442, no. 1–2, pp. 113–123, Jan. 1998, doi: 10.1016/S0022-0728(97)00498-1.

[134] H. Bode, K. Dehmelt, and J. Witte, "Zur kenntnis der nickelhydroxidelektrode—I.Über das nickel (II)-hydroxidhydrat," *Electrochim. Acta*, vol. 11, no. 8, pp. 1079–1087, Aug. 1966, doi: 10.1016/0013-4686(66)80045-2.

[135] L. D. Burke and D. P. Whelan, "Growth of electrochromic film on nickel in base under potential cycling conditions," *J. Electroanal. Chem. Interfacial Electrochem.*, vol. 109, no. 1–3, pp. 385–388, May 1980, doi: 10.1016/S0022-0728(80)80139-2.

[136] L. D. Burke and T. A. M. Twomey, "Voltammetric behaviour of nickel in base with particular reference to thick oxide growth," *J. Electroanal. Chem. Interfacial Electrochem.*, vol. 162, no. 1–2, pp. 101–119, Mar. 1984, doi: 10.1016/S0022-0728(84)80158-8.

[137] L. D. Burke and T. A. M. Twomey, "Influence of ph on the redox behaviour of hydrous nickel oxide," *J. Electroanal. Chem. Interfacial Electrochem.*, vol. 134, no. 2, pp. 353–362, Apr. 1982, doi: 10.1016/0022-0728(82)80013-2.

[138] L. D. Burke and D. P. Whelan, "Preliminary note A NEW INTERPRETATION OF THE CHARGE STORAGE AND ELECTRICAL CONDUCTIVITY BEHAVIOUR OF HYDROUS IRIDIUM OXIDE," 1981, *Elsevier Sequoia S.A.*

[139] L. D. Burke and D. P. Whelan, "A VOLTAMMETRIC INVESTIGATION OF THE CHARGE STORAGE REACTIONS OF HYDROUS IRIDIUM OXIDE LAYERS," 1984.

[140] R. Simpraga and B. E. Conway, "Realization of monolayer levels of surface oxidation of nickel by anodization at low temperatures," *J. Electroanal. Chem. Interfacial Electrochem.*, vol. 280, no. 2, pp. 341–357, Mar. 1990, doi: 10.1016/0022-0728(90)87008-8.

[141] J. Mozota and B. E. Conway, "Surface and bulk processes at oxidized iridium electrodes—I. Monolayer stage and transition to reversible multilayer oxide film behaviour," *Electrochim. Acta*, vol. 28, no. 1, pp. 1–8, Feb. 1983, doi: 10.1016/0013-4686(83)85079-8.

[142] B. E. Conway and J. Mozota, "Surface and bulk processes at oxidized iridium electrodes—II. Conductivity-switched behaviour of thick oxide films," *Electrochim. Acta*, vol. 28, no. 1, pp. 9–16, Feb. 1983, doi: 10.1016/0013-4686(83)85080-4.

[143] B. E. Conway and H. Angerstein-Kozlowska, "The electrochemical study of multiple-state adsorption in monolayers," *Acc. Chem. Res.*, vol. 14, no. 2, pp. 49–56, Feb. 1981, doi: 10.1021/ar00062a004.

[144] A. Seyeux, V. Maurice, L. H. Klein, and P. Marcus, "In situ scanning tunnelling microscopic study of the initial stages of growth and of the structure of the passive film on Ni(111) in 1 mM NaOH(aq)," *Journal of Solid State Electrochemistry*, vol. 9, no. 5, pp. 337–346, May 2005, doi: 10.1007/s10008-004-0627-5.

[145] D. Floner, C. Lamy, and J.-M. Leger, "Electrocatalytic oxidation of hydrogen on polycrystal and single-crystal nickel electrodes," *Surf. Sci.*, vol. 234, no. 1–2, pp. 87–97, Aug. 1990, doi: 10.1016/0039-6028(90)90668-X.

[146] J. L. Weininger and M. W. Breiter, "Hydrogen Evolution and Surface Oxidation of Nickel Electrodes in Alkaline Solution," *J. Electrochem. Soc.*, vol. 111, no. 6, p. 707, 1964, doi: 10.1149/1.2426216.

[147] O. Vodeb *et al.*, "Intrinsic properties of nanoparticulate Ir-based catalysts for oxygen evolution reaction by AC voltammetry," *Electrochim. Acta*, vol. 464, Feb. 2023, doi: 10.1016/j.electacta.2023.142882.

[148] S. Cherevko, S. Geiger, O. Kasian, A. Mingers, and K. J. J. Mayrhofer, "Oxygen evolution activity and stability of iridium in acidic media. Part 1. - Metallic iridium," *Journal of Electroanalytical Chemistry*, vol. 773, pp. 69–78, 2016, doi: 10.1016/j.jelechem.2016.04.033.

[149] S. Cherevko, S. Geiger, O. Kasian, A. Mingers, and K. J. J. Mayrhofer, "Oxygen evolution activity and stability of iridium in acidic media. Part 2. - Electrochemically grown hydrous iridium oxide," *Journal of Electroanalytical Chemistry*, vol. 774, pp. 102–110, 2016, doi: 10.1016/j.jelechem.2016.05.015.

[150] D. A. J. Rand and R. Woods, "Cyclic voltammetric studies on iridium electrodes in sulphuric acid solutions," *J. Electroanal. Chem. Interfacial Electrochem.*, vol. 55, no. 3, pp. 375–381, Sep. 1974, doi: 10.1016/S0022-0728(74)80431-6.

[151] E. J. Frazer and R. Woods, "The oxygen evolution reaction on cycled iridium electrodes," *Journal of Electroanalytical Chemistry*, vol. 102, no. 1, pp. 127–130, 1979, doi: 10.1016/S0022-0728(79)80036-4.

[152] S. Gottesfeld, "Faradaic Processes at the Ir/Ir Oxide Electrode," *J. Electrochem. Soc.*, vol. 127, no. 9, pp. 1922–1925, 1980, doi: 10.1149/1.2130037.

[153] L. D. Burke and E. J. M. O. Sullivan, "Oxygen gas evolution on hydrous oxides — An example of three-dimensional electrocatalysis?," *J. Electroanal. Chen*, vol. 117, pp. 155–160, 1981.

[154] S. Cherevko, S. Geiger, O. Kasian, A. Mingers, and K. J. J. Mayrhofer, "Oxygen evolution activity and stability of iridium in acidic media. Part 2. - Electrochemically grown hydrous iridium oxide," *Journal of Electroanalytical Chemistry*, vol. 774, pp. 102–110, Aug. 2016, doi: 10.1016/j.jelechem.2016.05.015.

[155] S. Cherevko, S. Geiger, O. Kasian, A. Mingers, and K. J. J. Mayrhofer, "Oxygen evolution activity and stability of iridium in acidic media. Part 1. - Metallic iridium," *Journal of Electroanalytical Chemistry*, vol. 773, pp. 69–78, Jul. 2016, doi: 10.1016/j.jelechem.2016.04.033.

[156] E. Fabbri and T. J. Schmidt, "Oxygen Evolution Reaction - The Enigma in Water Electrolysis," Oct. 05, 2018, *American Chemical Society*. doi: 10.1021/acscatal.8b02712.

[157] P. G. Pickup and V. I. Birss, "A model for anodic hydrous oxide growth at iridium," *J. Electroanal. Chem. Interfacial Electrochem.*, vol. 220, no. 1, pp. 83–100, Mar. 1987, doi: 10.1016/0022-0728(87)88006-3.

[158] J. Geppert *et al.*, "Microkinetic Analysis of the Oxygen Evolution Performance at Different Stages of Iridium Oxide Degradation," *J. Am. Chem. Soc.*, vol. 144, no. 29, pp. 13205–13217, Jul. 2022, doi: 10.1021/jacs.2c03561.

[159] J. Geppert, F. Kubannek, P. Röse, and U. Krewer, "Identifying the oxygen evolution mechanism by microkinetic modelling of cyclic voltammograms," *Electrochim. Acta*, vol. 380, Jun. 2021, doi: 10.1016/j.electacta.2021.137902.

[160] Y. Zhang, A. N. Simonov, J. Zhang, and A. M. Bond, "Fourier transformed alternating current voltammetry in electromaterials research: Direct visualisation of important underlying electron transfer processes," Aug. 01, 2018, *Elsevier B.V.* doi: 10.1016/j.coelec.2018.04.016.

[161] A. M. Bond, E. A. Mashkina, and A. N. Simonov, "2 A Critical Review of the Methods Available for Quantitative Evaluation of Electrode Kinetics at Stationary Macrodisk Electrodes," 2014.

[162] S. A. Bonke, A. M. Bond, L. Spiccia, and A. N. Simonov, "Parameterization of Water Electrooxidation Catalyzed by Metal Oxides Using Fourier Transformed Alternating Current Voltammetry," *J. Am. Chem. Soc.*, vol. 138, no. 49, pp. 16095–16104, Dec. 2016, doi: 10.1021/jacs.6b10304.

[163] L. Gundry *et al.*, "Recent advances and future perspectives for automated parameterisation, Bayesian inference and machine learning in voltammetry," *Chemical Communications*, vol. 57, no. 15, pp. 1855–1870, 2021, doi: 10.1039/d0cc07549c.

[164] P. Virtanen *et al.*, "SciPy 1.0: Fundamental Algorithms for Scientific Computing in Python," *Nat. Methods*, vol. 17, pp. 261–272, 2020, doi: 10.1038/s41592-019-0686-2.

[165] B. E. Conway, B. Barnett, H. Angerstein-Kozlowska, and B. v. Tilak, "A surface-electrochemical basis for the direct logarithmic growth law for initial stages of extension of anodic oxide films formed at noble metals," *J. Chem. Phys.*, vol. 93, no. 11, pp. 8361–8373, 1990, doi: 10.1063/1.459319.

[166] J. Mozota and B. E. Conway, "Surface and bulk processes at oxidized iridium electrodes—I. Monolayer stage and transition to reversible multilayer oxide film behaviour," *Electrochim. Acta*, vol. 28, no. 1, pp. 1–8, Jan. 1983, doi: 10.1016/0013-4686(83)85079-8.

[167] B. E. Conway and J. Mozota, "Surface and bulk processes at oxidized iridium electrodes—II. Conductivity-switched behaviour of thick oxide films," *Electrochim. Acta*, vol. 28, no. 1, pp. 9–16, Jan. 1983, doi: 10.1016/0013-4686(83)85080-4.

[168] A. BalaKrishnan *et al.*, "Direct Detection of Surface Species Formed on Iridium Electrocatalysts during the Oxygen Evolution Reaction," *Angew. Chem. Int. Ed.*, vol. 60, no. 39, pp. 21396–21403, Sep. 2021, doi: 10.1002/anie.202106790.

[169] N. Sivasankar, W. W. Weare, and H. Frei, "Direct observation of a hydroperoxide surface intermediate upon visible light-driven water oxidation at an Ir oxide nanocluster catalyst by rapid-scan FT-IR spectroscopy," *J. Am. Chem. Soc.*, vol. 133, no. 33, pp. 12976–12979, Aug. 2011, doi: 10.1021/ja205300a.

[170] C. Bozal-Ginesta *et al.*, "Redox-State Kinetics in Water-Oxidation IrOx Electrocatalysts Measured by Operando Spectroelectrochemistry," *ACS Catal.*, vol. 11, no. 24, pp. 15013–15025, Dec. 2021, doi: 10.1021/acscatal.1c03290.

[171] J. Mozota and B. E. Conway, "Surface and bulk processes at oxidized iridium electrodes—I. Monolayer stage and transition to reversible multilayer oxide film behaviour," *Electrochim. Acta*, vol. 28, no. 1, pp. 1–8, Jan. 1983, doi: 10.1016/0013-4686(83)85079-8.

[172] B. E. Conway and J. Mozota, "Surface and bulk processes at oxidized iridium electrodes—II. Conductivity-switched behaviour of thick oxide films," *Electrochim. Acta*, vol. 28, no. 1, pp. 9–16, Jan. 1983, doi: 10.1016/0013-4686(83)85080-4.

[173] G. Koderman Podboršek *et al.*, "Atomically-resolved structural changes of ceramic supported nanoparticulate oxygen evolution reaction Ir catalyst," *Electrochim. Acta*, vol. 426, Sep. 2022, doi: 10.1016/j.electacta.2022.140800.

[174] M. Bele *et al.*, "Towards Stable and Conductive Titanium Oxynitride High-Surface-Area Support for Iridium Nanoparticles as Oxygen Evolution Reaction Electrocatalyst," *ChemCatChem*, vol. 11, no. 20, pp. 5038–5044, Oct. 2019, doi: 10.1002/cctc.201901487.

[175] C. Daiane Ferreira Da Silva *et al.*, "Oxygen Evolution Reaction Activity and Stability Benchmarks for Supported and Unsupported IrOxElectrocatalysts," *ACS Catal.*, vol. 11, no. 7, pp. 4107–4116, Apr. 2021, doi: 10.1021/acscatal.0c04613.

[176] H. N. Nong *et al.*, "Key role of chemistry versus bias in electrocatalytic oxygen evolution," *Nature*, vol. 587, no. 7834, pp. 408–413, Nov. 2020, doi: 10.1038/s41586-020-2908-2.

[177] S. M. Alia *et al.*, "Activity and Durability of Iridium Nanoparticles in the Oxygen Evolution Reaction," *J. Electrochem. Soc.*, vol. 163, no. 11, pp. F3105–F3112, 2016, doi: 10.1149/2.0151611jes.

[178] H. O. Lloyd-Laney, M. J. Robinson, A. M. Bond, A. Parkin, and D. J. Gavaghan, "A Spotter's guide to dispersion in non-catalytic surface-confined voltammetry experiments," *Journal of Electroanalytical Chemistry*, vol. 894, Aug. 2021, doi: 10.1016/j.jelechem.2021.115204.

[179] G. K. Rowe, M. T. Carter, J. N. Richardson, and R. W. Murray, "Consequences of Kinetic Dispersion on the Electrochemistry of an Adsorbed Redox-Active Monolayer," 1995. [Online]. Available: https://pubs.acs.org/sharingguidelines

[180] "Scipy." [Online]. Available: https://scipy.org/

[181] P. Virtanen *et al.*, "SciPy 1.0: Fundamental Algorithms for Scientific Computing in Python," *Nat. Methods*, vol. 17, pp. 261–272, 2020, doi: 10.1038/s41592-019-0686-2.

[182] S. Gates-Rector and T. Blanton, "The Powder Diffraction File: a quality materials characterization database," *Powder Diffr.*, vol. 34, no. 4, pp. 352–360, Dec. 2019, doi: 10.1017/S0885715619000812.

Bibliography

Publications Related to the Thesis

Journal Articles

O. Vodeb *et al.*, “Intrinsic properties of nanoparticulate Ir-based catalysts for oxygen evolution reaction by AC voltammetry,” *Electrochim Acta*, vol. 464, Oct. 2023, doi: 10.1016/j.electacta.2023.142882.

O. Vodeb, P. Farinazzo Bergamo Dias Martins, D. Strmčnik, N. Hodnik, and M. Gaberšček, “ElectroKitty: A Python Tool for Modeling Electrochemical Data Including Non-Langmuir Adsorption,” *ACS Electrochemistry*, vol. 1, no. 8, pp. 1540–1544, Aug. 2025, doi: 10.1021/acselectrochem.4c00218.

Biography

After finishing high school in 2017 at Gimnazija Kranj, I enrolled in the chemical engineering programme at the University of Ljubljana, Faculty of Chemistry and Chemical Technologies. I have graduated from the course and thus earned my Bachelor's degree in 2020. In the same year, I then enrolled in the chemical engineering master's programme at the same faculty. During my second year of undergraduate studies, I began working in the Electrocatalysis group at the Department of Material Chemistry at the National Institute of Chemistry as a student assistant, where I continued until the end of my master's studies. After earning my master's degree in 2022, I was employed by the laboratory as a young researcher and enrolled at the International Postgraduate School of Josef Stefan as a PhD student in the programme Nanosciences and Nanotechnologies